Design, Modeling, and Simulation of Piezoelectric and Magnetoelectric Devices for Multimodal Energy Harvesting Applications

By

Nan Chen

A Dissertation Submitted in Partial Fulfillment

of the Requirements for the Degree of

Doctor of Philosophy in Computational Sciences

Middle Tennessee State University

October 2020

Dissertation Committee:

Dr. Vishwas Bedekar, Chair

Dr. William Robertson

Dr. Misagh Faezipour

Dr. Joshua Phillips

Program Director:

Dr. John Wallin

Dedicated to my mother, Liya Ke.

ACKNOWLEDGMENTS

Time flies so quickly. It has been eight years since I entered the Computational Science Program in the summer of 2012. There are many friends and family members, whom I am deeply thankful to, and without them, this dissertation would not have been completed. Beyond the support of family and friends, I would like to express my sincere gratitude to my academic advisor Dr. Vishwas N. Bedekar, who has provided insightful research experience and guidance in every step of the research, from the qualifying exam to the final dissertation preparation. Through working with Dr. Bedekar, I have seen a bigger picture of the computational material science research through accomplishing key requirements of the Computational Science Program at Middle Tennessee State University. I would also like to thank the committee members: Dr. William Robertson, Dr. Joshua Phillips, and Dr. Misagh Faezipour for reading through drafts of the dissertation, and providing valuable feedback, advice, and suggestions of improvements through key stages in the research. At the same time, I would like to thank the Program Director, Dr. John Wallin, for writing the recommendation letter with my advisor to nominate me for the Provost Writing Fellowship and facilitating the progress of my research.

Lastly, I would like to thank my mom, Liya Ke, and all my friends, Nathan Knight, Jesse Keogh, Sean Hagan, Cosmo Sperduto, for constantly being supportive. Without them, this dissertation would not be possible.

`

ABSTRACT

The power consumption of electronic devices reduces as the size of these devices shrinks [1]. Today most portable and wearable devices are still powered by batteries. Researchers have been considering various renewable energy sources including solar, wind, tidal, and mechanical vibrations [1]. The application demands the electronic devices being used in any weather conditions, anytime, and anywhere [1]. Mechanical vibrations are abundantly available in structures such as bridges, machinery, engines, and aircraft. Hence, several researchers have been developing self-powered MEMS (Microelectromechanical Systems): energy harvesters which are made of piezoelectric materials or magnetostrictive materials to provide power for low power electric devices at the mW or μW level using mechanical vibrations [1] [2].

All piezoelectric materials and magnetostrictive materials have a Curie temperature. When the operating temperature is higher than the Curie temperature, piezoelectric and magnetoelectric materials lose the ability to generate electric power from mechanical vibration or magnetic fields in an environment [2] as the aligned electric and magnetic dipole moments become disordered by the thermal disturbance. The Curie temperature of the piezoelectric materials and magnetoelectric (ME) materials can be as high as 40 ~ 180 °C for the PZT based piezoelectric materials and up to 680 °C for Fe based magnetostrictive materials [2]. Given the fact that the Curie temperature of piezoelectric and magnetoelectric materials is much

`

higher than the normal operating temperature range of batteries, composite piezoelectric and magnetoelectric energy harvesters are more suitable to operate in extreme environments in terms of wider operating temperature range.

To answer the question of how to harvest energy from a broad range of mechanical vibrations in an environment, we have developed multiple stages of the research proposal to address the challenges in designing various multimodal energy harvester devices. These designs include piezoelectric harvesters through a multi-beam approach, a one-piece trapezoidal approach, and a two-piece trapezoidal approach using our composite piezoelectric material. Full-width half-maximum (FWHM) bandwidth is one of the methods to benchmark the vibration bandwidth of our piezoelectric and magnetoelectric (ME) vibration energy harvesters (VEH). Our piezoelectric and magnetoelectric (ME) VEH models are simulated using COMSOL Multiphysics software. COMSOL Multiphysics is a commercial finite element analysis computer simulation software that specializes in solving two or more coupled multi-physics problems and is widely used in engineering fields, research & product development, and academic communities. We expanded our research from a simple rectangular bimorph model to the multi-beam model and nonlinear models, and we demonstrate the wider band of the device. We further developed nonlinear shapes such as the trapezoids to investigate the frequency bandwidth of the device. The one-piece trapezoidal model was expanded to a two-piece trapezoidal beam harvester model to demonstrate that the two-piece trapezoidal piezoelectric cantilever can achieve a broader vibration frequency response. The two-piece trapezoidal piezoelectric composite beam design resulted in a broader bandwidth of 5.6 Hz while generating a maximum power density of 16.81 mW/cm^3, whereas the one-piece

`

trapezoidal beam generated a maximum power density 10.37 mW/cm^3 with a bandwidth 2.9 Hz in our previous work [3] [4]. These results helped us to design for broader band piezoelectric and ME energy harvesters with higher electric power density. For single ME rectangle energy harvesters, the peak electric power reaches 8.99 mW and peak electric power density at 192 mW/cm^3 via the optimal resistor of 0.5 MΩ. For the one-piece trapezoidal ME energy harvesters, we saw the peak electric power reaching 37.1 mW and peak electric power density of 56.2 mW/cm^3 with an optimal resistance of 0.013 MΩ. In this work, we have advanced our research from composite piezoelectric beam models to novel trapezoidal magnetoelectric composite beam designs for harvesting not only vibration energy but also magnetic energy from the surrounding environment.

`

TABLE OF CONTENTS

LIST OF TABLES

`

LIST OF FIGURES

`

`

CHAPTER 1: INTRODUCTION

The majority of wearable and portable electronic devices rely on the lifetime of the battery. The battery needs periodic recharge or disposal which prohibits the continuous use of these wearable devices [1]. Despite battery technology advances in terms of power density and capacity in recent years [1] [5], there are still some limitations to utilize the power from a battery [1] [2] [6]. Once batteries become depleted, they are either discarded or recharged. Discarded batteries become an environmental hazard. The lifespan of a battery is sensitive to the number of recharge cycles and the operating temperature [6]. The capacity of the battery decreases as the number of recharge cycles increase. Battery lifetime is also sensitive to temperature: if the temperature in the environment is too high, there would be irreversible damage to the battery. On the other hand, if the temperature in the environment is too low, there would be a temporary reduction in battery life. As there are many known disadvantages of battery power, researchers have been considering various renewable energy sources such as solar, wind, tidal, and mechanical vibrations [1]. Solar, wind and, tidal energy all have their limitations as renewable energy sources (e.g. weather, geographical location, time of the day). On the other hand, mechanical vibrations are available abundantly on structures such as bridges, machinery, and vehicles. Each system that uses a frequency domain thus becomes an attractive source for mechanical vibrations resulting in harvesting energy for medical monitoring device applications and wireless sensing applications in which batteries have been the dominant power source [7]. There are several mechanisms to transform mechanical vibration energy to electrical energy that provide high power density as well as a range of

operational frequencies: electromagnetic induction, the direct piezoelectric effect, and the magnetoelectric effect. Compared with electromagnetic induction, piezoelectric and magnetoelectric (ME) energy harvesters have a smaller form factor, simpler structure, and higher power density [1]. The electric power and the voltage of a piezoelectric and ME vibration energy harvester (VEH) diminish significantly when vibration frequency deviates from the resonance frequencies of the VEH [7]. For instance, MicroStrain Piezoelectric Vibration Energy Harvester (PEH) produces 30 mW at 1.04 kHz [8]; when the vibration frequency shifts 1% from the resonance frequency, 1.04 kHz, the electric power drops to 20% ~ 40% of its peak electric power of 30 mW [8]. To address the issue of low bandwidth of energy harvesters, there have been several efforts to improve bandwidth of piezoelectric energy harvesters [1] [7] [9] [10], and magnetoelectric energy harvesters [11, 12]. The multi-beam method is a popular method to broaden the bandwidth of the piezoelectric and ME VEH as it provides multiple resonance frequencies based on the geometry of the harvester. Liu *et al.* studied a microarray of a multi-layered composite cantilever beam generating 3.98 μW effective electric power and 3.93V DC voltage as shown in Figure 1 and Figure 2 [10].

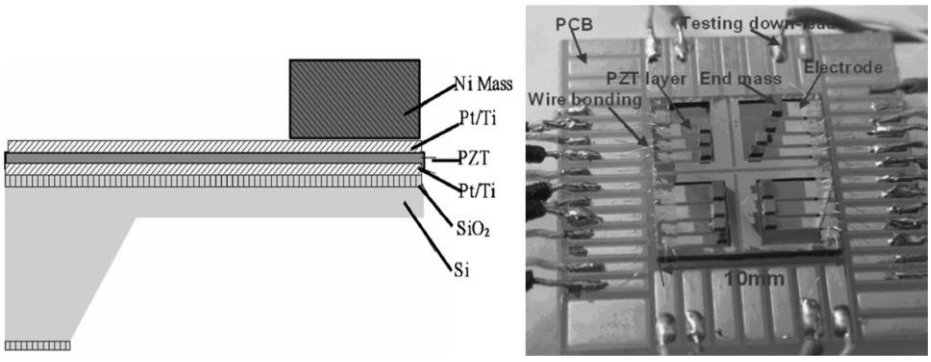

Figure 1. (Left) A composite piezoelectric beam design. (Right) A wideband microarray power

generator works from 226 to 234 Hz proposed by Liu *et al*. [10].

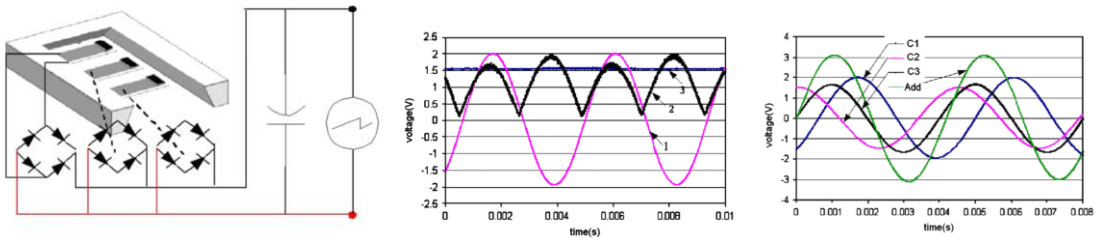

Figure 2. The electrical connection between each cantilever in the left subplot for the microarray design proposed by Liu *et al.*; the AC voltage generated by one piezoelectric cantilever (pink) in the middle subplot; the rectified voltage signal after 3 rectifiers (black). The DC voltage signal after a capacitor and rectifiers were added (blue). An electric voltage reading of three cantilevers in the microarray prototype on the right subplot; the blue curve indicates the total voltage [10].

Liu *et al.* described a problem they observed where the phase of the AC voltage generated by the 1st cantilever and the 2nd cantilever separated by 120° as shown in the right subplot of Figure 2. The phase difference cancels out the voltage generated by three individual cantilevers in the microarray [10]. Therefore, a capacitor was added after the AC voltage signal was rectified into the DC electrical signal as shown in the middle subplot shown in Figure 2 [10]. Liu *et al*. claimed the bandwidth of their multi-beam design is from 226 Hz to 234 Hz (8 Hz), which is narrower than the bandwidth of our piezoelectric multi-beam design 18 Hz (62.303 Hz - 80.303 Hz) reported in Chapter 3 Section 3.3. T. M. Ferrari *et al.* studied a multi-beam system where they found that RMS (root mean square) voltage was increased by 200 % when they added the driving beam in the middle of two piezoelectric beams shown in the upper left

plot in Figure 3 [13]. However, Ferrari *et al.* did not show the power density bandwidth of their piezoelectric multi-beam prototype nor did they consider the power density of the multi-beam system. The electric power increases with the size increase of the multi-beam system. Therefore, comparing the electric power density of piezoelectric layer(s) is more meaningful than comparing the electric power between piezoelectric and ME VEH models. For this reason, we have chosen the electric power density as well as the electric power density bandwidth of the piezoelectric layer to benchmark various piezoelectric and ME VEHs models.

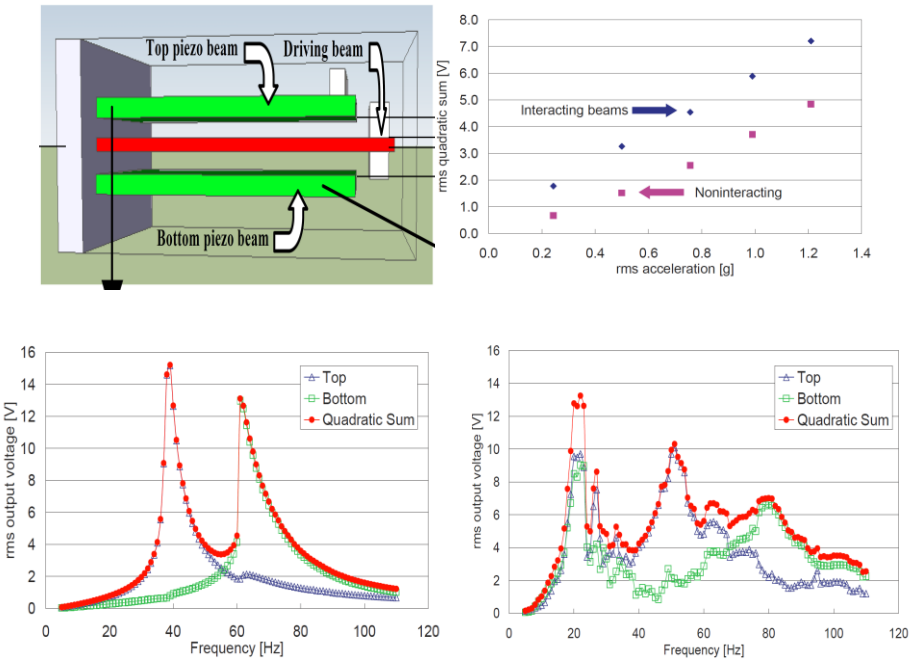

Figure 3. (Upper left) a multi-beam piezoelectric VEH proposed by Ferrari *et al.* (upper right) RMS voltage increases as the acceleration of the multi-beam increases. The model with the driving beam has a higher RMS voltage than the model without the driving beam. (Lower left) the RMS voltage-mechanical vibration frequency response of a non-interacting multi-beam model. The resonance frequency is 40 Hz and 46 Hz. (lower right) the resonance frequency shifted from 40 Hz, 46 Hz to 20 Hz due to the driving beam was added in the multi-beam

model [13].

Wu *et al.* studied a piezoelectric multi-beam system with one main beam and two folded auxiliary beams [9]. Wu *et al.* discovered that the M-shape multi-beam has a more concentrated resonance frequency (14.3 Hz, 17.8 Hz, 24.3 Hz) than that of the Y-shaped multi-beam (6.2 Hz, 21.4 Hz, 41.9 Hz) because the M-shaped multi-beam is more compact than the Y-shaped multi-beam [9]. Wu *et al.* also showed the open voltage bandwidth of the M-shaped multi-beam, which is 12 Hz (from 13 Hz to 25 Hz) in the right subplot of Figure 4. As we can see from the right subplot of Figure 4, the red curve shows that the M-shaped multi-beam has three separate peaks at three different resonance frequencies (15 Hz, 17 Hz, 24 Hz) for each beam. However, Wu *et al.* did not show the power density nor the mechanical bandwidth of their M-shaped multi-beam, yet our research group tabulated the electric power density and bandwidth of our multi-beam model and the results are reported in Chapter 3. Wu *et al.* did not explain the method to interpret the open voltage bandwidth (12 Hz, 13 Hz to 25 Hz), yet we have used full-width half-maximum (FWHM) bandwidth a criterion to measure the vibration bandwidth of our piezoelectric energy harvesters. We also discussed the limitations of applying the FWHM bandwidth to our broadband energy harvester models in Chapter 3.

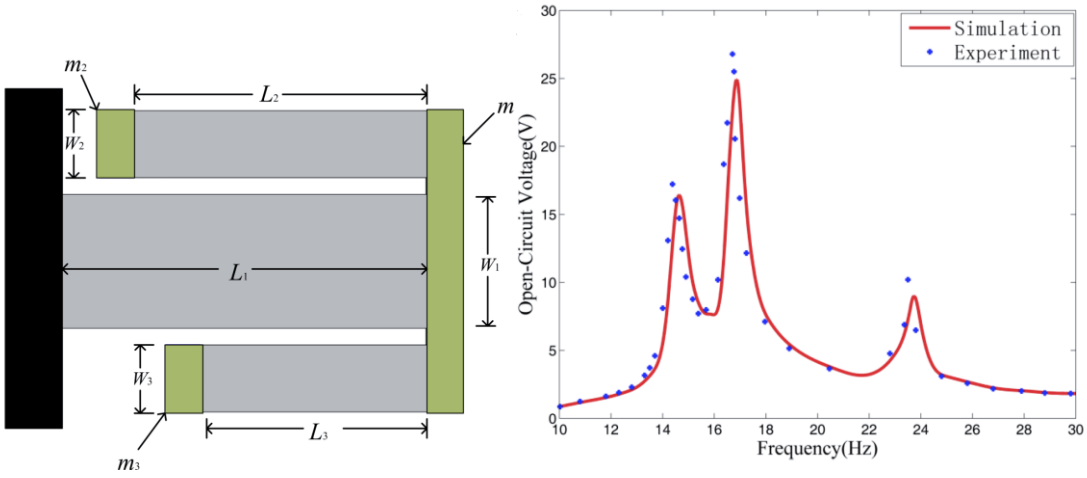

Figure 4. (Left subplot) Top view of an M-shaped piezoelectric broadband VEH. The green rectangles are tip mass (m_1, m_2, m_3). The gray rectangles are piezoelectric multi-beam [9]. (Right subplot) Experimental and simulation data of open voltage bandwidth of the M-shaped piezoelectric broadband VEH [9].

The first step was to model a single piezoelectric/ME beam with the piezoelectric, piezomagnetic, and mechanical material properties and we showed a step by step conversion scheme in our first published article in Journal of Materials Science Research [14]. The piezoelectric, piezomagnetic, and mechanical material properties are tabulated in Table 1.

`

Table 1. Name and definition of piezoelectric and mechanical material properties [14]

Piezoelectric Material property	Definition
k_{31}	Electro-mechanical piezoelectric coupling factor ratio of Electrical Energy converted (1-direction) to Mechanical Energy applied (3-direction)
ε_{33}	Dielectric constant in z direction (F/m)
d_{31}	Piezoelectric charge constant (C/N)
g_{31}	Piezoelectric voltage constant (V m/N)
ν	Poisson's ratio (negative ratio of transverse strain to axial strain)
$\tan \delta$	Dissipation factor (ratio of active power to reactive power)
S_{11}	Compliance in 1-direction (Pa^{-1}, inverse of stiffness)

There have been several efforts to perform the theoretical analysis and experiments investigating piezoelectric energy harvesting; however, a detailed systematic approach to convert material properties into a compliance matrix before they are fed to the COMSOL Multiphysics model was missing in the literature. This work is useful to other researchers because the conversion scheme serves as a guide to model any polycrystalline piezoelectric/ME material in COMSOL simulation if the piezoelectric/piezomagnetic and the

`

mechanical material properties are known. We also verified this conversion scheme by comparing our piezoelectric model's electric power and output voltage data with those of another researcher in Chapter 4 [15]. With the ability to model any polycrystalline piezoelectric material, the MTSU research group has designed a composite piezoelectric multi-beam system with five beams at five different lengths at 44 mm, 48 mm, 52 mm, 56 mm, and 60 mm. All the piezoelectric beams in our multi-beam model have a uniform width of 10 mm and a uniform thickness of 0.55 mm. In all piezoelectric and ME models, we have used the PZTPZN-Scheme4 polycrystalline ceramic piezoelectric material as it was reported to have a superior power density than other PZTPZN-Scheme materials [15]. Bedekar *et al*. reported the measured electric power density is 0.1713 mW/cm^3, 20.97 % higher than that of PZT-ZNN Scheme2 (0.1416 mW/cm^3), 15.38 % higher (49.5 μW measured) in the electric power output, 31.13 % higher (0.499 mW/cm^3 measured) in the piezo-element power density, as the two-step sintering method was used to reduce grain size and increase density, which leads to higher relative dielectric (ε_r is 1588, 2.95 ~ 4.23 times higher than those of PZT-ZNNs) and piezoelectric property of PZN-PZN Scheme4 material (charge constants in the thickness mode d_{33} is 400 pC/N, 2.4 to 2.6 times higher than that of PZT-ZNNs. The charge constants of PZT-PZN in the transverse mode d_{31} is 153.73 pC/N, 2.75 ~ 3.07 times higher than those of PZT-ZNNs) [15]. Not only are the power densities of the PZT-PZN-Scheme4 higher than its PZT-ZNN competitors, but also is PZT-PZN-Scheme4's quality factor Q significantly lower (78.7) than that of PZN-ZNN (780) which makes PZT-PZN-Scheme4 a better material choice for a broadband energy harvester as the PZT-PZN-Scheme4 is a low-quality factor material [4] [16]." The chemical formula PZTPZN-Scheme4 is 0.8 [Pb ($Zr_{0.52}$ $Ti_{0.48}$) O_3] – 0.2 [Pb ($Zn_{1/3}$ $Nb_{2/3)}$ O_3], which was developed by Bedekar *et al.* However, PZTPZN-Scheme4 has not been

`

used in any composite multi-beam piezoelectric energy harvester design and simulation to date. The electro-mechanical vibration bandwidth of the multi-beam model is tabulated in Chapter 3 Section 5.3. To carry on our research in developing higher performance and broader band energy harvester designs, we investigated various non-linear geometries of the magnetoelectric (ME) beams, as a nonlinear geometry provides an opportunity to widen the electro-mechanical bandwidth response of a piezoelectric VEH. Ramalingam Usharani *et al.* reported that the maximum voltage is available when the taper angle is at 2.25 degrees [17]. Rouhollah and Mohsen studied the "trapezoidal v-shaped" beam and proposed an analytical formula for the resonance frequency of the trapezoidal beam: the authors showed that the analytical resonance frequency of the trapezoidal beam is twice as much as that of the rectangular beam [18]. However, the authors did not discuss the electro-mechanical bandwidth of the V-shaped beam or the trapezoidal beam. The trapezoidal V-shaped beam designs are shown in Figure 5.

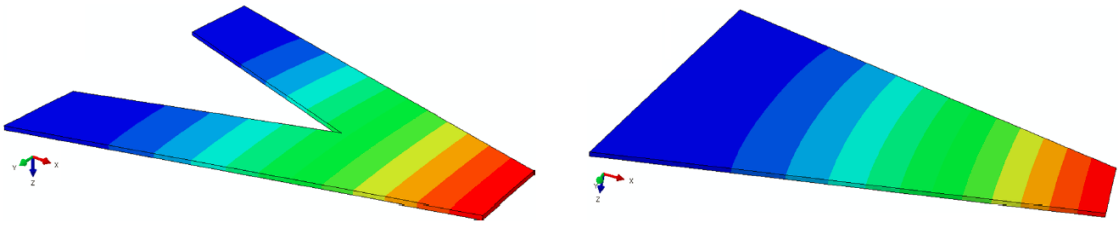

Figure 5. (Left) A deformed V-shaped beam when it vibrates at the first resonance frequency; (Right) a deformed trapezoidal-shaped cantilever when vibrating at its first resonance frequency [18].

Because the minimum power density data and the electro-mechanical bandwidth data of the nonlinear piezoelectric VEHs are often missing in the literature [18] [19] [20], we investigated

the performance of our one-piece trapezoidal and two-piece trapezoidal composite piezoelectric beams to effectively improved the electric power and power density output. No publication can be found on PZTPZN-Scheme4 use in any two-piece trapezoidal multi-beam piezoelectric energy harvester design to date. The electro-mechanical bandwidth of the trapezoidal models is tabulated in Chapter 3 Section 5.3. Using our knowledge and findings on modeling the piezoelectric energy harvesting, we further our research by modeling rectangular and trapezoidal magnetoelectric (ME) energy harvester designs through simulations. Since polycrystalline ceramic piezoelectric materials are brittle, the electromechanical coupling coefficient of the piezoelectric materials are generally low (k from 0.3 to 0.4). Researchers have been looking for newer, smarter materials which have a higher coupling coefficient (k > 0.7) and are resistant to fatigue and aging. The working principle of the magnetoelectric effect is: change in the surrounding magnetic field changes the shape of magnetostrictive material which generates mechanical strain in the materials. This mechanical strain gets transferred to the piezoelectric material bonded to the magnetostrictive material. Using the direct piezoelectric effect, the piezoelectric material generates an electric charge and voltage that can be harvested. The advantage of the magnetoelectric energy harvester is harvesting energy from two sources, viz. mechanical vibrations and change in the magnetic field(s), instead of just one source. Thus, the harvester generates higher voltage, improved electric power, and electric power density by extracting energy from two sources. This multimodal energy harvesting design provides greater and more efficient possibilities for energy harvesting. Existing literature studies the magnetic-electric (ME) behavior of a single composite beam of the piezoelectric layer and magnetic-electric layer [21]. Nan *et al.* [21] studied three different ME composites: 0-3 (particulate composite), 2-2 (laminate composite), 1-3 (fiber/rod composite),

and proposed an analytical calculation of the effective ME coefficient tensor α concerning piezoelectric and piezomagnetic coupled effect. 0-3 (particulate composite) and 1-3 (fiber/rod composite) ME composite configurations are not related to our research as we are focusing on the laminate composite (2-2) for all our piezoelectric and magnetoelectric energy harvesting models. Nan *et al.* [21] also pointed out that placing the magnetic field in parallel with the electric polling direction is not optimal for the 2-2 laminated composite, and instead suggested placing the magnetic field perpendicular to the electrical polling which yields a greater ME effect as $\alpha_{31} > \alpha_{33}$ [21]. Fiebig pointed out that there was previous research that tried out many different angles between the magnetic ac and dc fields [22]. The research concluded that the ME voltage coefficient reaches its maximum when AC and DC magnetic fields are parallel [23]. Nan *et al.* showed that the maximum value for the ME coefficient α of a laminated (2-2) PZT-$CoFe_2O_4$ in its transverse orientation (26 V/cm·Oe^{-1}) is about "10 times higher than that of its longitudinal orientation (3 V/cm·Oe^{-1})" when the laminated beam vibrates at its fundamental frequency, 300 Hz [21]. Yet the author did not mention the electric power density or the electro-mechanical bandwidth results of the composite magnetoelectric energy harvesting device. The electro-mechanical bandwidth is a metric to describe how wide the mechanical vibration is when the targeted electric power and voltage level is maintained. Fiebig *et al.* pointed out that a large ME effect (90 V/cm·Oe^{-1}) is observed by applying "a weak AC magnetic field and a strong DC bias field" and interests towards ME material revived after 1985 [22]. Therefore, in theory, the electric power reaches the maximum when we apply a saturation magnetic biased DC field in the transverse direction toward the ME VEHs, as the ME coefficient α reaches maximum value while the magnetostriction reaches maximum. Also, the literature suggests that the performance of the magnetoelectric composite beam can be

optimized when vibrating the composite beam at the first mechanical resonance frequency. Fabricating laminated 2-2 composite material is much easier than other types of composites [21]. Because of the promising results, we refined our composite piezoelectric model into a composite magnetoelectric (ME) model operating in the transverse mode (the magnetic fields are placed orthogonal to the electric polling direction) which couples the piezoelectric effect with the magnetostrictive effect further enhancing the electric power density. There are many applications of the magnetoelectric energy harvester. For example, composite magnetoelectric energy harvesters can operate near electric motors or the electric generators where a dynamic magnetic field can be found. Fiebig reported that composite magnetoelectric energy harvesters can be used to convert a microwave magnetic field into a microwave electric field [22]. The composite magnetoelectric device can also be used to make AC or DC magnetic field sensors. A large ME response of 260 $mV \cdot Oe^{-1}$ by a PZT/Terfenol-D tri-layer structure under a weak magnetic field (1 nT) was reported by Fiebig [22].

`

CHAPTER 2: OBJECTIVES OF RESEARCH

As mentioned in Chapter 1, to address the issue of replacement and recharging of batteries we designed, developed, and simulated a magnetoelectric energy harvester that can scavenge energy from multiple sources such as vibration and changes in the magnetic field. More specifically, the objectives of this research are:

- To model a generalized piezoelectric and ME material computationally. Being able to build a piezoelectric/ME model in COMSOL is the foundation of all other research objectives.
- To find an optimized design of a piezoelectric composite energy harvester beam through computational simulations. This will be achieved through parametric modeling of various harvester geometries followed by an analysis of the energy characteristics of the harvester. The second objective was achieved in our first, second, and third publications and the fourth manuscript (under preparation).
- To design, model, simulate, and optimize a magnetoelectric (ME) energy harvester that can harvest energy from two sources viz. changing magnetic field and the mechanical vibrations at the same time.
- To design, develop, simulate, and optimize a magnetoelectric energy harvesting system based on our knowledge from previous piezoelectric energy harvester results. This will be very useful research to enhance the actual electric power generated by the energy

harvester as well as the electric power density of the device thereby providing an enhanced onboard energy harvesting solution to small-scale electronic devices.

`

CHAPTER 3: PIEZOELECTRIC ENERGY HARVESTER

3.1.1 Overview

The objective of this research is designing an energy harvesting device to overcome the prominent issue in the research field namely that the electric power drops sharply as soon as the mechanical vibration frequency shifts away from the resonant frequency shown in Figure 6 [14]. The issue is widely reported throughout the literature [7] [18] [20]. The left subplot of Figure 6 shows an actual vibration energy harvester (VEH, MicroStrain) which is used in a wireless sensing application. The right subplot of Figure 6 shows a limited bandwidth. The full-width half-maximum bandwidth of the MicroStrain VEH is 15.5 Hz.

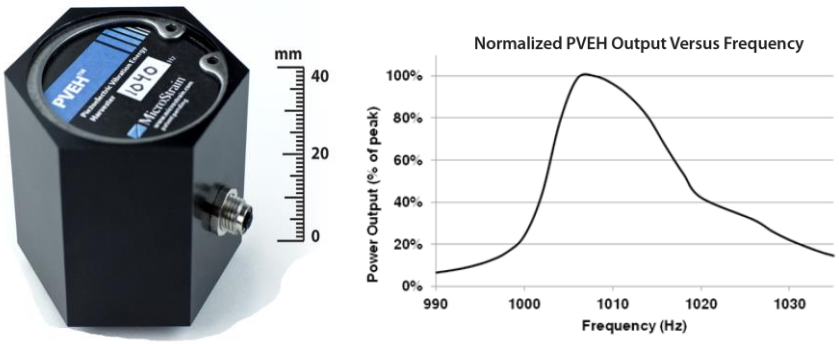

Figure 6. (Left) MicroStrain piezoelectric vibration energy harvester used in wireless sensing application. (Right) The electric power output of MicroStrain piezoelectric vibration energy harvester reaches 100% of peak power (30 mW, 3 VDC) when it vibrates at the resonance

frequency (1.04 kHz) with 1.5g acceleration [8].

The research group started modeling a simple rectangle piezoelectric bimorph cantilever. A unimorph beam is a single-layer structure as it is shown in Figure 7. A bimorph is defined as a structure comprised of two unimorphs of material, as shown in Figure 8.

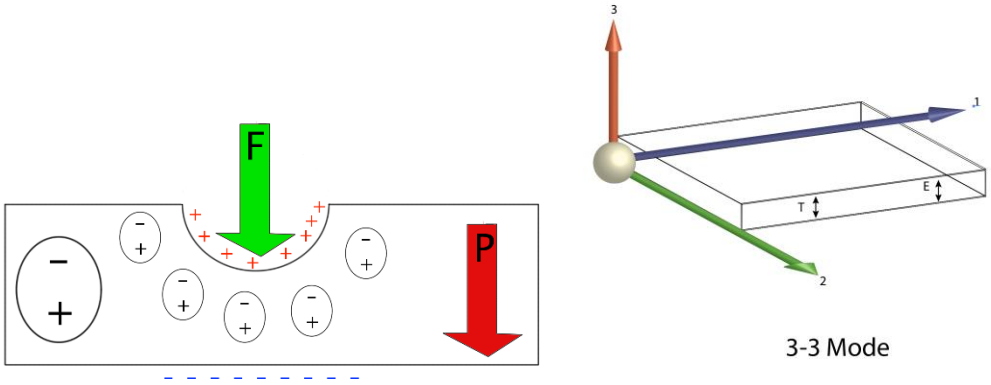

Figure 7. The left subplot shows a cross-section of a piezoelectric cantilever beam operates in 3-3 mode. The tight subplot shows the direction of stress T and the electric field E inside the 3-1 mode [14].

Because of the superior performance of the two-layer structure (bimorph) over unimorph [14], we started our research from a piezoelectric rectangular bimorph design. Our bimorph beam is made by two polycrystalline unimorphs stuck together with a mixture of conductive CircuitWorks CW2400 Conductive Epoxy Adhesive (parts A and B). Part A epoxy is for establishing the conductive interface between the piezoelectric layer and the thin brass layer. The part B hardener is for creating a strong bond between the PZT layer and the thin brass layer. The part A and part B Conductive Epoxy Adhesive is mixed at 1:1 ratio and quickly

placed in a temperature-controlled oven at 150 °F to 250 °F for five to ten minutes for fast curing. Without a firm mechanical bonding between the piezoelectric layer and the thin brass layer, the composite piezoelectric device can delaminate, therefore, the electro-mechanical impedance increases significantly [24]. Wandowski *et al.* showed that partially bonded composite piezoelectric transducers lead to reduced amplitudes of the structure resonance peaks due to impedance increase [24]. A cross-section of the bimorph is shown in Figure 8. The left side of the bimorph is fixed. The bottom surface of the bimorph is electrically grounded. When the composite beam is bent downward, as shown in Figure 8, the upper layer of the bimorph expands and the upper layer of the bimorph contracts. The voltage is measured between the top surface and the bottom surface of the bimorph. This configuration is known as the series configuration. An alternating voltage is generated by both upper and lower PZT-PZN layers due to the combined direct piezoelectric effect in the bimorph.

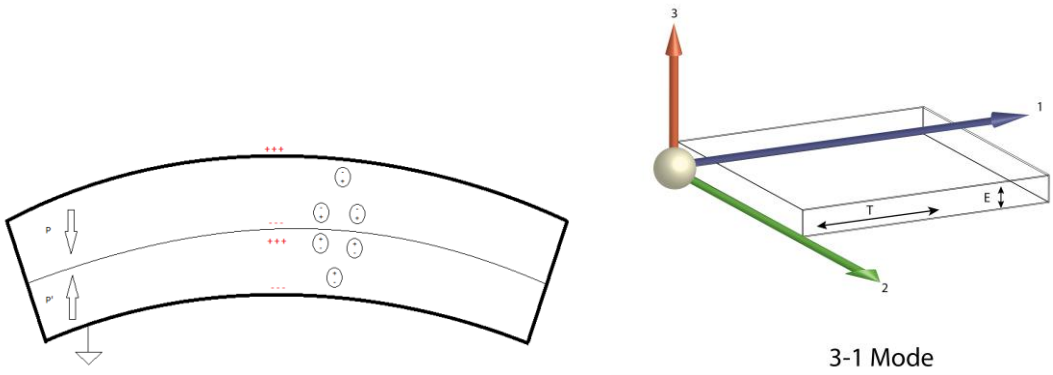

Figure 8. Left subplot shows a piezoelectric bimorph bending downward in the 3-1 mode [14], the upper layer has tensile stress and the lower layer has compressive stress. The right subplot shows the direction of the stress T along 1 direction and the electric field E are along 3

direction.

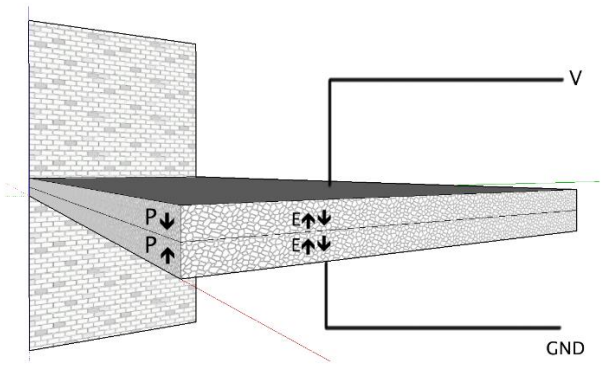

Figure 9. Bimorph connected in series [14].

In vibration energy harvester design, the cantilever is often thin and bended during mechanical vibration, the stress is along the length direction (1 direction), and the electric field E is along the thickness direction (3 direction); therefore, the mode is often known the 3-1 mode. In 3-1 mode, the direction of stress and the electric field are orthogonal, whereas the direction of stress and the electric field are in parallel in 3-3 mode

3.1.2 Piezoelectric material's compliance matrix

One of the contributions from our work is that we published a method of modeling any polycrystalline piezoelectric material by taking piezoelectric and mechanical material properties into our piezoelectric and piezomagnetic models. Electro-mechanical properties are expressed in the form of constitutive relations in the strain-charge form in equations (1) and

`

(2), which are shown below [14]:

$$D_i = \mathbf{d}_{ijk}\, T_{jk} + \boldsymbol{\varepsilon}_{ij} E_j \quad (1)$$

$$S_{ij} = \mathbf{s}_{ijkl} T_{kl} + d^T E_k \quad (2)$$

Our step-by-step conversion scheme from the piezoelectric material and the mechanical material properties to the compliance matrix and the coupling matrix was published [14], where D_i is the electric charge displacement vector, $\mathbf{d}_{ijk}$ is the piezoelectric coupling tensor, $\boldsymbol{\varepsilon}_{ij}$ is the dielectric tensor, S_{ij} is the strain vector, $\mathbf{s}_{ijkl}$ is the compliance tensor, which is a 4 th rank tensor, having 81 elements. T_{kl} is the stress vector, d^T is the piezoelectric coupling tensor under the stress, E_j is the electric field vector, and the subscripted index i, j, k, l indicates the direction of each element in the vectors and the order of tensors. Due to symmetry, the compliance matrix has 6 rows and 6 columns, which can be written in matrix form (3)

$$\begin{bmatrix} S_{11} & S_{12} & S_{13} & 0 & 0 & 0 \\ S_{11} & S_{11} & S_{13} & 0 & 0 & 0 \\ S_{13} & S_{13} & S_{33} & 0 & 0 & 0 \\ 0 & 0 & 0 & G^{-1} & 0 & 0 \\ 0 & 0 & 0 & 0 & G^{-1} & 0 \\ 0 & 0 & 0 & 0 & 0 & G^{-1} \end{bmatrix} \quad (3)$$

Notice that the compliance matrix must be a positive definite matrix, and all elements on the diagonal must be non-zero. The piezoelectric coupling tensor d, which can be written in the coupling matrix form below in the coupling matrix (4).

`

$$\begin{bmatrix} 0 & 0 & 0 & 0 & d_{15} & 0 \\ 0 & 0 & 0 & d_{24} & 0 & 0 \\ d_{31} & d_{31} & d_{33} & 0 & 0 & 0 \end{bmatrix} \quad (4)$$

We can fill the coupling tensor d with the material properties of PZTPZN-Scheme4 in the matrix (5).

$$\begin{bmatrix} 0 & 0 & 0 & 0 & 496 & 0 \\ 0 & 0 & 0 & 496 & 0 & 0 \\ 153 & 153 & 400 & 0 & 0 & 0 \end{bmatrix} \text{ pC/N} \quad (5)$$

The compliance matrix of the piezoelectric material was the first obstacle for anyone to model any piezoelectric material in COMSOL. G, the shear modulus, is the first thing that needs to be obtained by Youngs modulus E and Poisson ratio ν, either through a material property datasheet or through calculation via equation (6) below.

$$G = \frac{E}{2\,(1+\nu)} \quad (6)$$

All values to the compliance matrix were substituted for the PZT-PZN Scheme4 sample as the following format in the matrix (7).

`

$$\begin{bmatrix} 1.65 & -0.57 & -1.65 & 0 & 0 & 0 \\ -0.57 & 1.65 & -1.65 & 0 & 0 & 0 \\ -1.65 & -1.65 & 3.11 & 0 & 0 & 0 \\ 0 & 0 & 0 & 4.09 & 0 & 0 \\ 0 & 0 & 0 & 0 & 4.09 & 0 \\ 0 & 0 & 0 & 0 & 0 & 4.09 \end{bmatrix} 10^{-11}\ \mathrm{Pa}^{-1} \quad (7)$$

The relation between the mechanical-electrical coupling coefficient k, piezoelectric charge constant d, and dielectric constant and compliance is established by $k_{31}^2 = \frac{d_{31}^2}{\varepsilon_{33}^T S_{11}^E}$ [25] . Finding coupling coefficient k is the key to find more unknown elements in the compliance matrix. The piezoelectric charge constant d, dielectric constant ε, and compliance **s** can be found in Table 2 and Appendix A.

Table 2. Piezoelectric material properties value

	ρ (kg/m3)	d_{33}(pC/N)	ε_r	tan δ	s_{11}(Pa^{-1})
Sample#1	7850	290	757.735	0.0024	1.01×10^{-11}
Sample#2	7880	198	449.992	0.0057	1.15×10^{-11}

Based on Hooke's law, the relation between strain and stress is established by equation (8):

`

$$\varepsilon = \mathbf{s}\,\sigma \tag{8}$$

ε is the strain, **s** is the compliance of the material, which is inverse of stiffness, and σ is the stress. The relation between the negative ratio transverse strain and axial strain is expressed by the definition of Poisson's ratio in equation (9):

$$\nu = -\frac{\varepsilon_{12}}{\varepsilon_{11}} = -\frac{S_{12}\sigma_1}{S_{11}\sigma_1} = -\frac{S_{12}}{S_{11}} \tag{9}$$

The material is electrically poled along the z-axis ("3" direction). The piezoelectric ceramics material is transversely isotropic [7], therefore the transversely isotropic property was used to find more elements in the compliance matrix using the following equation (10) [12].

$$S_{11} = S_{22}, \quad S_{12} = S_{21}, \quad S_{13} = S_{31}, \quad S_{23} = S_{32}, \quad S_{11} = S_{22} \tag{10}$$

There is a more general form of calculation of S_{ij} as follows [12].

$$S_{ij} = \frac{d_{ij}^2}{k_{ij}^2 \varepsilon_{ij}^T} = \frac{d_{ij}^2}{k_{ij}^2 (d_{ij}^T / g_{ij}^T)} \tag{11}$$

By equation (11) and the transversely isotropic property, more compliance matrix elements can be found in equation (12) as follows

`

$$S_{13} = S_{31} = S_{32} = S_{23} = \frac{d_{31}^2}{k_{31}^2(d_{31}^T/g_{31}^T)} \quad (12)$$

$k_{33}{}^2$ is the conversion ratio of the mechanical work $W_M = \frac{F\Delta Z}{2}$ and electrical work $W_E = \frac{Q^2}{2C_p}$ of the cantilever beam [26]. The ratio be expressed in equation (13):

$$k_{33}{}^2 = \frac{W_E}{W_M} \quad (13)$$

Taking the square root on both sides and substituting W_E and W_M, and Q = C_p V, the following equation (14) is obtained:

$$k_{33} = \sqrt{\frac{W_E}{W_M}} = \sqrt{\frac{Q^2/(2C_p)}{F??Z/2}} = \frac{\sqrt{C_p}V}{\sqrt{F??Z}} \quad (14)$$

$??Z$ is the defection of the cantilever beam; F is the exciting force; Q is the electric charge accumulated on the surface of the beam; C_p is the capacitance of the cantilever beam between the upper surface and the lower surface; V is the voltage of the cantilever beam between the upper surface and lower surface of the beam. In the 3-1 mode, the beam can be simplified by

`

considering the compliance on the lower right elements in equation (15) from the compliance matrix.

$$S_{44} = S_{55} = S_{66} \quad (15)$$

So far, all piezoelectric elements of the compliance matrix are obtained for the anisotropic model simulations and all elements are tabulated in Appendix A.

3.1.2 The equivalent circuit and the vibrational bandwidth of VEHs

The equivalent electric circuit is shown in Figure 10. The piezoelectric/ME energy harvester can be modeled as a series LRC electric circuit with an alternating voltage source V in a circuit, L represents internal inductance, R represents internal resistance (damping), and C represents internal capacitance (stiffness). The letter Z in the equivalent electric circuit represents the external loading impedance.

`

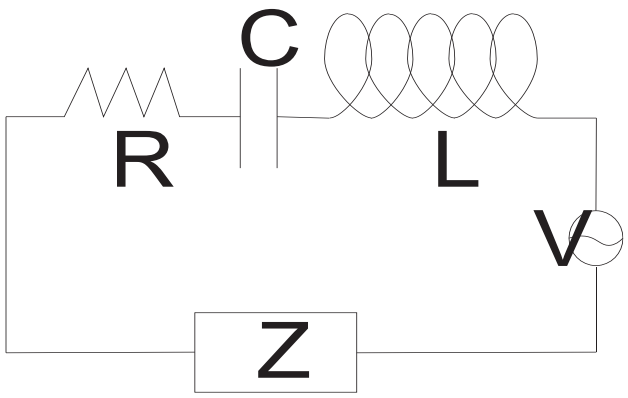

Figure 10. An equivalent LRC electric circuit of a piezoelectric bimorph energy harvester.

When the external impedance Z matches the internal impedance of LRC circuit , where X_c is the internal capacitive reactance the bimorph and X_L are the internal inductance of the bimorph, the electric power output reaches a maximum (widely known as the rule of impedance matching). In this case, when the external loading resistance Z matches the impedance of the internal impendence, the bimorph generates the maximum electric power; the calculation of a loading impedance is shown in equation (16).

$$Z = \sqrt{R^2 + (X_L - X_c)^2} \qquad (16)$$

Taking the square on both sides of equation (16) to obtain equation (17) , where f is the frequency of the oscillating electric signal in the equivalent electric circuit, which is presented in Figure 10.

`

$$Z^2 = r^2 + \left(2\pi f L - \frac{1}{2\pi f C}\right)^2 \quad (17)$$

In equation (17), the internal resistance r, the internal inductance L, and the internal capacitance C of a bimorph are fixed values; therefore, the frequency f of the oscillating signal in the equivalent electric circuit will be affected by the value of the external loading resistor. The internal resistance r, the internal inductance L, and the internal capacitance C need to be found before modeling the electric characteristics of a piezoelectric bimorph cantilever beam. The internal resistance r can be found by applying the Kirchhoff's Voltage Law (KVL) and the Ohm's Law in a closed electric equivalent circuit as shown in Figure 10, as it is expressed in equation (18).

$$\varepsilon = I\,r + I\,R + I\,Z_c + I\,Z_L \quad (18)$$

where ε is the electromotive force (EMF), I is the electric current, R the internal resistance, Z_c is the impedance of the capacitor, and Z_L is the impedance of the inductor in the closed electric equivalent circuit as shown in Figure 10. We can then take two measurements by using two different external loading resistors in the simulation and rewriting the Kirchhoff's Voltage Law (KVL) and the Ohm's Law in a pair of equations (19) and (20).

`

$$U_1 + I_1 (X_L - X_c) = - R I_1 + \varepsilon \quad (19)$$

$$U_2 + I_2 (X_L - X_c) = - R I_2 + \varepsilon \quad (20)$$

Where U_1 is the voltage across the external loading resistor Z_1, I_1 is the current going through the external resistor on the first measurement. U_2 is the voltage across a different external loading external resistor Z_2, I_2 is the current going through the external resistor R_2 in the second measurement. Since U_1, U_2, I_1, I_2, X_L, and X_c are known parameters, as they can be found in the simulations, we have two equations and two unknowns (R, ε); the internal resistor R can be easily found by solving the pair of equations (19) and (20). Thus, the pair of equations (19) and (20) can be simplified to equation (21), where Z_1 is the vector sum of the impedance of the inductor and the capacitor in the first measurement with one external loading resistor Z_1, and Z_2 is the vector sum of the impedance of the inductor and the capacitor in the second measurement with one external loading resistor Z.

$$R = \frac{-[(U_2 - U_1) + (I_2 |Z_2| - I_1 |Z_1|)]}{I_2 - I_1} \quad (21)$$

However, it would be impossible to find the internal resistor R of a given bimorph without knowing the values of the internal inductance L and the internal capacitance C of a bimorph in the closed electric equivalent circuit as shown in Figure 10. The inductance L and the

`

capacitance C in the closed electric equivalent circuit can be found in the COMSOL simulation. The reactance of the equivalent electric circuit can be found by equations (22) and (23).

$$|Z_1| = |X_{L1} - X_{c1}| = |2\pi f_1 L - \frac{1}{2\pi f_1 C}| \quad (22)$$

$$|Z_2| = |X_{L2} - X_{c2}| = |2\pi f_2 L - \frac{1}{2\pi f_2 C}| \quad (23)$$

The frequency f_1 and f_2 of the oscillating electric signal are due to two distinct resistive loadings Z_1 and Z_2 but $|Z_1| \neq |Z_2|$. Equations (22) and (23) are substituted to equation (21), the internal resistance r is expressed in equation (24):

$$R = \frac{-[(U_2 - U_1) + (I_2 |2\pi f_2 L - \frac{1}{2\pi f_2 C}| - I_1 |2\pi f_1 L - \frac{1}{2\pi f_1 C}|)]}{I_2 - I_1} \quad (24)$$

where the two distinctive oscillating frequencies f_1 and f_2 of the electric signal in two different resistive loadings can be found in simulations. The internal resistance R of the bimorph can be found by taking two different measurements as shown in equation (24). Equation (24) can be simplified to equation (25) once the inductance L and the capacitance C in the closed equivalent electric circuit are known through the simulation, as two oscillating frequencies f_1 and f_2 are the resonance frequencies of the equivalent electric circuit.

`

$$\mathrm{r} = \frac{-(U_2 - U_1)}{I_2 - I_1}, \mathrm{f} = f_r \quad (25)$$

The internal resistance r of the bimorph can be found by just taking two different voltage and current measurements ($U_1, U_2, I_1, I_2, U_1', U_2', I_1', I_2'$) with two different external resistive loads as shown in equation (24), given the value of the inductance L and the capacitance C, which is to be found in two separate simulations. The capacitance C is the ratio between the electric charge Q ($7.1028 \times 10^{-6}\ C$, $8.3341 \times 10^{-6}\ C$) on the upper surface of the bimorph and the voltage U (100 V for both designs) between the surfaces of the bimorph in equation (24) can be found by looking up the component of the capacitance matrix es.C_{11} in the "Derived Values" section in a stationary study, where C_{d1} is the capacitance of the first trapezoidal bimorph beam design when the shorter width W_1 is 18 mm, and the longer width W_2 is 40 mm. C_{d1} is calculated in equation (26). L_{d1} is the inductance of the first trapezoidal bimorph beam design when the shorter width W_1 is 18 mm, and the longer width W_2 is 40 mm. L_{d1} is calculated in equation (27). C_{d2} is the capacitance of the second trapezoidal bimorph beam design when the shorter W_1 is 18 mm and the longer width W_2 is 52 mm. C_{d2} is calculated in equation (28). L_{d2} is the inductance of the second trapezoidal bimorph beam design when the shorter width W_1 is 18 mm, and the longer width W_2 is 52 mm. L_{d2} is calculated in equation (29). The inductance L of the bimorph can be calculated by equation (30), where mef.Y_{11} is the admittance and mef.omega is the angular frequency of the electric signal in the AC equivalent electric circuit, both of which can be found in the simulation.

`

$$C_{d1} = \frac{Q}{U} = \frac{7.1028\times10^{-6}\,C}{100\,V} = 71028\ \text{pF} \quad (26)$$

$$L_{d1} = 776\ \text{H},\ f_{r1} = \frac{1}{2\pi\sqrt{LC}} = 21.4\ \text{Hz} \quad (27)$$

$$C_{d2} = \frac{Q}{U} = \frac{8.3341\times10^{-6}\,C}{100\,V} = 83341\ \text{pF} \quad (28)$$

$$L_{d2} = 643\ \text{H},\ f_{r2} = \frac{1}{2\pi\sqrt{LC}} = 21.7\ \text{Hz} \quad (29)$$

$$L = \text{imaginary}\left(\frac{1}{\text{mef}.Y_{11}.\text{iomega}}\right) \quad (30)$$

The internal resistance R_1 and R_2 are calculated by equations (31) and (32) under the resonance frequency f_{r1} and f_{r2} of the electric signal in the equivalent circuit by taking two different voltage and current measurements ($U_1, U_2, I_1, I_2, U_1', U_2', I_1', I_2'$) with two different external resistive loads Z_1 (0.01 M Ω) and Z_2 (0.02 M Ω), which are arbitrarily chosen.

$$R_1 = \frac{-(U_2-U_1)}{I_2-I_1} = \frac{-(22.95\,V-11.393\,V)}{0.0011475A\ -\ 0.0011393A} = 1.4\ \text{MΩ} \quad (31)$$

$$R_2 = \frac{-(U_2'-U_1')}{I_2'-I_1'} = \frac{-(31.537\,V-17.844V)}{0.0015768\,A\ -0.0017844\,A} = 65\ \text{kΩ} \quad (32)$$

`

Thus far, the internal resistance (R_1, R_2), the capacitance and the inductance of two bimorphs can be obtained through calculation. The values of the internal inductance L, internal capacitance C, and the internal resistance R of the bimorph in an equivalent circuit, together, determine the value of the electric quality factor Q_e by equation (33) [4].

$$Q_e = \frac{1}{R}\sqrt{\frac{L}{C}} \tag{33}$$

Alternatively, the mechanical quality factor Q_m of a structure can also be calculated by equation (34), which is adopted by COMSOL. f is the resonance frequency of the vibration. Due to mechanical damping, the complex value of the resonance frequency has an imaginary part (complex number). For instance, the complex resonance frequency of the two-piece trapezoidal bimorph (the first design, the length of the single plate is 60 mm, W_1 is 40 mm, and W_2 is 2 mm) 14.5 + 0.2i Hz in a COMSOL eigenfrequency study. The mechanical quality factor Q_m is 28.645 can be obtained by equation (34).

$$Q_m = \frac{abs\,(f)}{2\ imaginary\,(f)} \tag{34}$$

In such a way, we can plot the mechanical quality factor Q_m for all permutations of each bimorph geometry of two trapezoidal designs in Figure 11 and Figure 12. The mechanical quality factor

Q_m increases when the longer length W_2 increases for both trapezoidal designs. Yet, the shorter width W_1 does not have a significant effect on the mechanical quality factor Q_m.

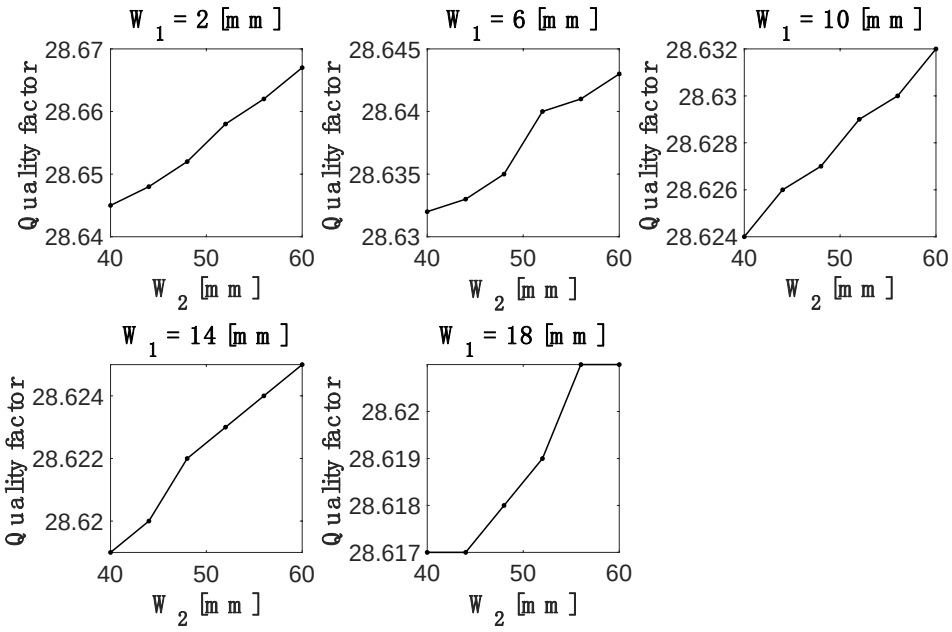

Figure 11. The mechanical quality factor Q_m of the first trapezoidal bimorph design. The The damping ratio is 0.017. The length of the beam L is 60 mm; the thickness of T_{piezo} is 0.3 mm;

the thickness of the brass layer T_s is 0.05 mm.

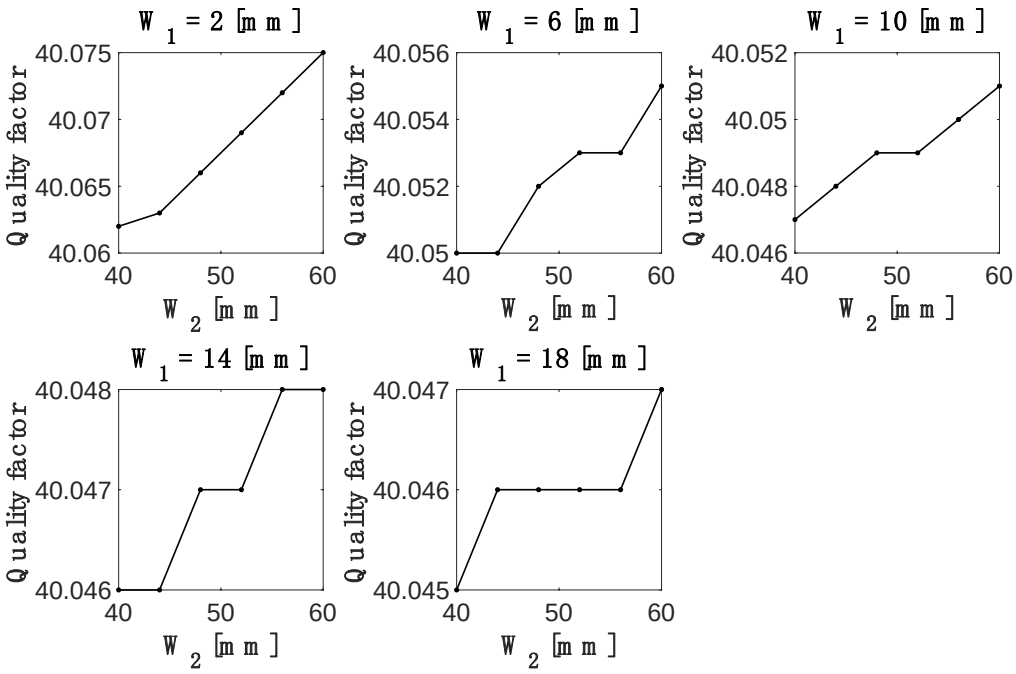

Figure 12. The mechanical quality factor Q_m of the second trapezoidal bimorph design. The damping ratio is 0.017. The length of the beam L is 60 mm; the thickness of T_{piezo} is 0.3 mm; the thickness of the brass layer T_s is 0.05 mm.

To investigate the mechanical quality factor Q_m, the complex nature of the eigenfrequency needs to be understood. The reason for the imaginary component w_i of the angular frequency is that it determines if the amplitude $e^{w_i t}$ of the oscillation of the VEH grows or shrinks in time, as equation (35) indicated. A(t) is a time-dependent damped oscillation function.$e^{-jw_r t}$ is a regular oscillation term, which can be further expanded by Euler's formula. The real part w_r of the

`

angular frequency determines the physical oscillation frequency. The positive real part $e^{w_i t}$ of angular frequency indicates the amplitude of the oscillation grows with time. The negative real part $e^{w_i t}$ of angular frequency indicates the amplitude of oscillation shrinks with time [27].

$$A(t) = e^{wt} = e^{w_i t}\, e^{-jw_r t} \quad , \; w = w_i + w_r \tag{35}$$

The damping ratio ζ is defined by COMOSL in equation (36).

$$\zeta = \frac{imaginary\,(f)}{abs\,(f)} \tag{36}$$

The damping ratio ζ (0.017) can be obtained by taking the real part and the imaginary part out of the complex eigenfrequency and plug them into equation (36). There is very little damping (ζ is 0.017) when the two-piece trapezoidal bimorph (the first design, length of the single plate is 60mm, W_1 is 40 mm and W_2 is 2 mm) vibrates under its first resonance frequency 14.5 Hz. A high damping ratio ζ harms the power output of a trapezoidal composite bimorph due to a high loss factor. The mechanical quality factor Q_m and the resonance frequency f_r of the two-piece trapezoidal beam both contribute to the mechanical resonance bandwidth. The resonance bandwidth Δf of an oscillator is defined by the full-width at half-maximum of its electric power at the resonance vibrational frequency. A VEH with a lower quality factor has a wider resonance bandwidth as the resonance bandwidth Δf is positively proportional to the resonance frequency

`

f_r and negatively proportional to the quality factor Q. The relation can be expressed in equation (37) below. f_r is the resonance frequency of the trapezoidal beam.

$$\Delta f = \frac{f_r}{Q}, \; Q = \frac{1}{R}\sqrt{\frac{L}{C}} \tag{37}$$

The resonance frequency f_r of a series electric circuit can be found when the capacitive and the inductive reactance is equal ($X_c = X_L$, $\frac{1}{2\pi fC} = 2\pi fL$). Therefore, the resonance oscillating frequency f_r is commonly expressed by equation (38), where L is the inductance, and C is the capacitance of a given bimorph.

$$f_r = \frac{1}{2\pi\sqrt{LC}} \tag{38}$$

Equation (33) and equation (38) are substituted to equation (37); therefore, the FWHM resonance bandwidth Δf can be expressed in equation (39), where R is the internal resistance of the bimorph, L is the internal inductance of the equivalent electric circuit. The resistivity of the composite materials (PZT-PZN, brass) and the internal inductance L of the bimorph both contributes to the length of the bandwidth of a bimorph.

$$\Delta f = \frac{f_r}{Q} = \frac{\frac{1}{2\pi\sqrt{LC}}}{\frac{1}{R}\sqrt{\frac{L}{C}}} = \frac{R}{2\pi L} \tag{39}$$

`

The change in the capacitance C changes the nominator f_r (resonance) as well as the denominator Q, the capacitance C cancels each other; therefore, the resonance width is independent of the capacitance. Q The bandwidth of the resonance frequency Δf can be calculated once the quality factor Q and the resonance frequency f_r are known. As we can see from equations (37) and (39), a higher equivalent internal resistance R of a series-connected bimorph and/or a lower equivalent internal inductance L in an series electrical circuit will contribute to a lower quality factor of a series LRC system, which ultimately leads to a wider the resonance bandwidth Δf of a system. The total internal resistance R and the total internal inductance L are expressed in equations (40) and (41). The upper PZT-PZN layer has resistance r_1, inductance L_1. The lower PZT-PZN layer has resistance r_2 ,inductance L_2. The resistance of the middle brass layer is r_3. Many researchers modeled the piezoelectric energy harvesters with similar equivalent LRC circuit [28] [25].

$$r = r_1 + r_2 + r_3 \tag{40}$$

$$L = L_1 + L_2 \tag{41}$$

The resonance frequency can be expressed by the analytical computation or the eigenfrequency analysis. The analytical resonance frequency is calculated by the young modulus E, the area of the moment of inertia I, as explained in our previous work [7]. The product EI is also referred to as the bending rigidity. The analytical formula of the resonance vibrational frequency can be

`

expressed by equation (42) for the first mode vibration [25]. As the tip mass m increases, the uniform load per unit length w increases and the first resonance decreases. Constant K_1 is a relating to the first resonance of the vibration. The acceleration of gravity g is 9.8 m/s^2. The tip mass is often used to fine-tune the resonance frequency of a beam as the tip mass increase the uniform load per unit length w in the denominator of equation (42)

$$f_1 = \frac{K_1}{2\pi}\sqrt{\frac{EIg}{wL^4}} \ , K_1 = 3.52 \tag{42}$$

The definition of the area moment of inertia along principle x-axis along the center of the cross-section of a rectangle beam by equation (43), where b is the width and h is the thickness of a rectangle beam.

$$\mathrm{I} = \int y^2 \, dA = \int_{-\frac{b}{2}}^{\frac{b}{2}} \int_{-\frac{h}{2}}^{\frac{h}{2}} y^2 dy dx = \frac{bh^3}{12} \tag{43}$$

Submitted equation (43) to equation (42), equation (44) is obtained.

$$f_1 = \frac{K_1}{2\pi}\sqrt{\frac{Ebh^3g}{12wL^4}} \ , K_1 = 3.52 \tag{44}$$

The uniform load per unit length w by equation (45), where m is the mass, ρ is the density of the beam, and L is the length of the beam.

`

$$w = \frac{m}{L} = \frac{\rho V}{L} = \frac{\rho\ bhL}{L} = \rho\ bh \qquad (45)$$

We can substitute equation (45) into equation (44) to obtain equation (46). We can see the first resonance f_1 is proportional to the thickness h and $\frac{1}{L^2}$. In order to design a low frequency VEH, besides adding a tip mass, we can also either make a bimorph thinner or/and make a bimorph longer. Increasing the length of the rectangle beam is more effective than making thickness low in reducing the eigenfrequency. We can also see that the width of the beam b does not appear in f_1, indicating the width has no effect on the eigenfrequency.

$$f_1 = \frac{K_1}{2\pi}\sqrt{\frac{\boldsymbol{Eh^2g}}{12\rho\boldsymbol{L^4}}} = \frac{K_1}{4\pi}\sqrt{\frac{\boldsymbol{Eg}}{3\rho}}\frac{h}{L^2}\ , K_1 = 3.52 \qquad (46)$$

Thus far, we can calculate the area moment of inertia I and the first resonance frequency of one-end-free and one end-fixed composite rectangle bimorph cantilever with a thin brass substrate.

3.1.3 Optimization

We started the optimization by running an eigenfrequency analysis in COMSOL. The eigenfrequency analysis is the main approach to find the lowest frequency mode of vibrations of

the structure. Once the eigenfrequency analysis is performed, we then found the first resonance frequency of the energy harvesting device. We pick the first resonance frequency because the research aim is to design a low mechanical vibration frequency energy harvesting device, as there are many low-frequency applications in our environment such as the vibration energy harvesting application of a walking person [29]. Once we find the first resonance frequency, we keep the same mechanical vibration in a separate simulation study and connect the energy harvesting device with an external electric circuit with a variable resistor. We then increase the resistance of this external resistor from 0 MΩ. The common patterns of the voltage and the electric power are consistent with the results in the literature [15] [30, 31]. One common pattern shows that the electric voltage increases to a local maximum, then the voltage becomes flat as the external resistance increases. Another common pattern is that the electric power increases to a local maximum, then the electric power drops after that point as the loading resistor increases.This common pattern is due to the impedance matching. Once the optimal resistance is found, we keep the same optimal resistance in the external electric circuit. We then treat the mechanical vibration of the piezoelectric beam as a variable in frequency studies. In our previous published work [3], we studied the mechanical vibration - electric power density bandwidth using the same method. We found an 18 Hz broadband FWHM mechanical vibration - electric power density bandwidth. We can see that 18 Hz FWHM electric power density bandwidth is much wider than the bandwidth of the MicroStrain's VEH device at 15.5 Hz in Chapter 3 Section 1.1.

`

3.2 MODELING OF SINGLE RECTANGLE PIEZOELECTRIC BEAM

3.2.1 Overview

The plan is changing the geometry of a rectangular piezoelectric bimorph with the discrete increases in terms of its length from 40 mm to 60 mm in steps of 4 mm, width from 2 mm to 18 mm in steps of 4 mm, and thickness from 0.2 mm to 0.5 mm in steps of 0.05 mm of the single rectangular composite piezoelectric VEH design. The method of determining the Full-Width Half Maximum (FWHM) bandwidth of the electrical power-mechanical vibration is a parametric sweeping on the mechanical vibrating frequency around the first resonance frequency +/- 5 to 20 Hz with a 1 Hz interval having the optimal resistance fixed for each corresponding discrete dimension [3].

3.2.2 Results and discussion

The results reflect changes in the length of the beam from 40 mm to 60 mm with increments of 4 mm, the width of the beam from 2 mm to 18 mm with an interval of 4 mm, thickness from 0.2 mm to 0.5 mm with an interval of 0.05 mm. The shift of open-circuit voltage can be seen in Figure 13. The open-circuit voltage is negatively proportional to the thickness of the bimorph on the upper right subplot; in other words, the maximum mechanical deformation of the beam decreases with increasing cross-section area. A thinner rectangular piezoelectric bimorph beam offers higher voltage and output electrical power than thicker rectangular piezoelectric bimorph [14].

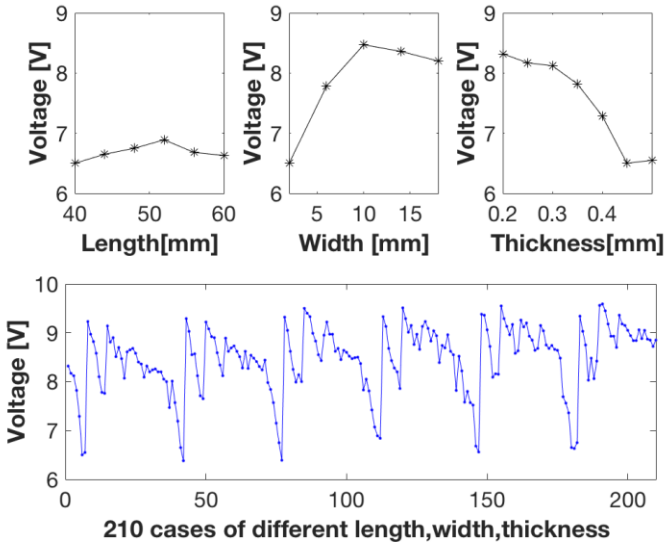

Figure 13. Sample1's open-circuit voltage response in terms of variation of beam's dimension (l,w,t) in 210 cases [14].

It can be seen in Figure 14 and Figure 15 that the longer bimorph has a lower resonance frequency (left); the thicker bimorph has a higher resonance frequency (right) as the natural frequency of the beam is also inversely proportional to the thickness of the beam.

`

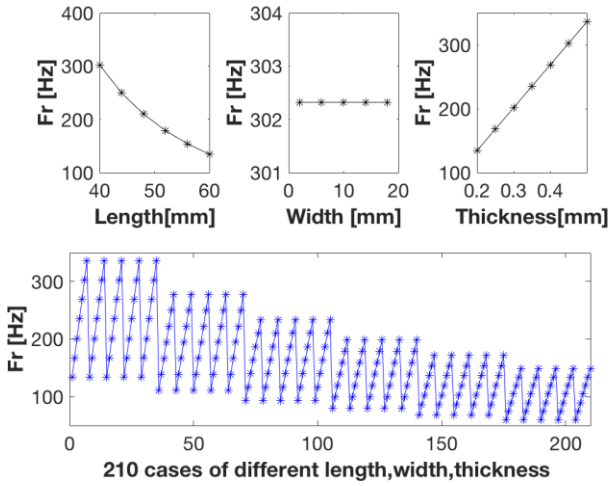

Figure 14. Sample one's resonance frequency response in terms of variation of the beam's dimension (l,w,t). In the following section, it is shown how the analytical resonant frequency changed when length, width, and thickness were changed individually. The analytical first resonance frequency f_1 is determined from Young's modulus E, the acceleration of gravity g, the density ρ the inverse quadratic term of length $\frac{1}{L^2}$, the thickness h.

$$f_1 = \frac{K_1}{2\pi}\sqrt{\frac{Eg}{12\rho}}\frac{h}{L^2}\ , K_1 = 3.52 \qquad (47)$$

The analytical first resonance frequency f_1 in equation (47) matches the simulation results shown in Figure 14 and Figure 15 [25]. It can be seen from the upper left subplot of Figure 14 and Figure 15 that the longer and thinner bimorph has a lower analytical resonance frequency due to the factor $\frac{h}{L^2}$ in equation (47). Similar effect appears on the unimorph. The thickness h of the beam has a linearly increasing effect on the resonance frequency of the cantilever. The

length L has a quadratic decrease in the resonance frequency of the cantilever. The width b (or w) has no effect on the resonance frequency of the rectangle cantilever as the analytical first resonance frequency f_1 shown in equation (47) as well as from the simulation results shown in Figure 14 and Figure 15.

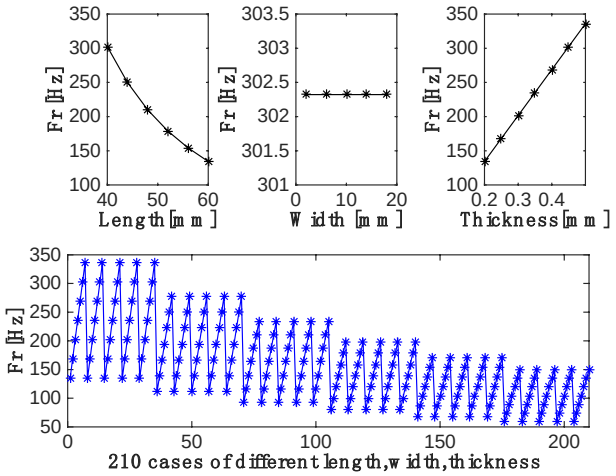

Figure 15. Sample two's analytical resonance frequency response in terms of variation of the beam's dimension (l,w,t).

It can be seen from the upper left subplot of Figure 16 that the longer bimorph had higher power output, the wider bimorph had lower power output, and the thicker bimorph had lower power output. When the length is 60 mm, the width is 2 mm, the thickness is 0.2 mm, the maximum power of the first sample obtained was 1.75×10^{-3} watts; the maximum power of the second sample obtained was 3.14×10^{-4} watts. Figure 16 shows how power changed when length, width, and thickness changed individually. The maximum power density of the first PZT-PZN sample is 7.28 mW/cm^3 and, that of the second PZT-PZN sample is 13.08 mW/cm^3.

`

The power density results agree with the published results of H. Kim et al.: the electric power density of piezoelectric micro-energy-harvesting devices range between 10 to 400 mW/cm^3 in the acceleration range of 2.3 to 78.4 m/s^2 and the frequency range of 0.08 to 1 kHz [14]. It is clear from the results that the electric power generated is directly proportional to the length of the beam whereas it is inversely proportional to the width and thickness of the beam. In other words, longer, thinner, and shorter width rectangle bimorph design generates enhanced power and operators in lower vibration frequency.

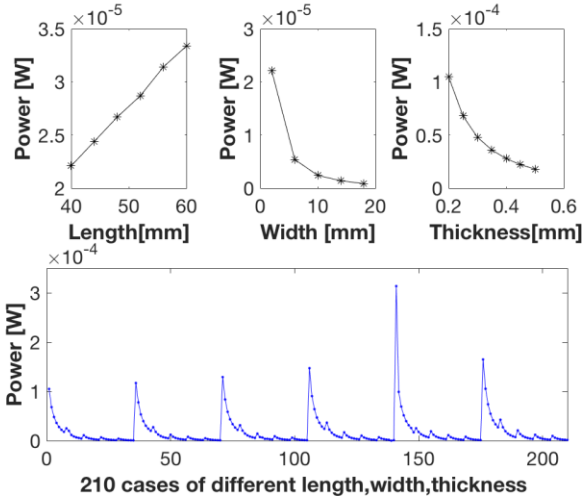

Figure 16. Sample1's power response in terms of variation of the beam's dimension (l,w,t).

The ultimate purpose of designing a high-performance energy harvester is to provide power to the electrical components, such as resistors. The optimum resistance was calculated based on maximum power generation. In a practical scenario, the device will be operated at the natural frequency of the beam at an optimized resistance for its geometry so that the device always generates maximum power.

3.2.3 Verification and validation

We have verified our results and validated our simulation model by comparing our simulation results with the experimental data published by other researchers [15]. The plots of RMS voltage and the average electric power vs load resistance of the PZT-PZN (Scheme4) comparison between our results (simulated data, line) and other researcher's results (measured data, circles) are shown in Figure 17.

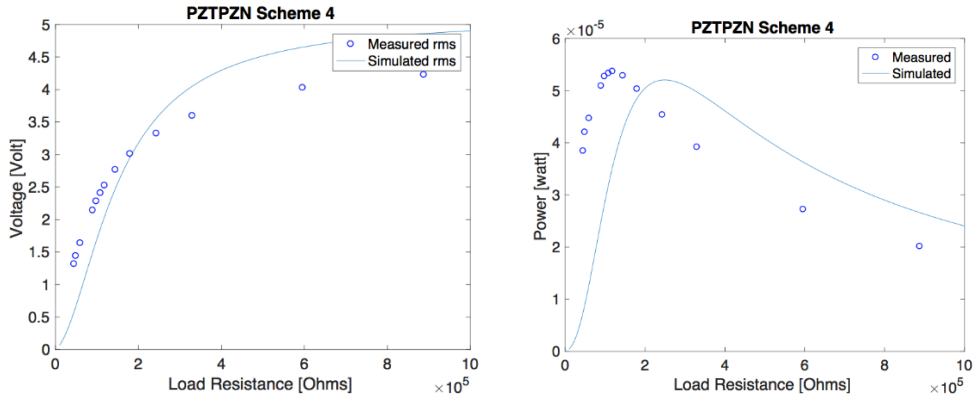

Figure 17. The RMS voltage and the average power vs load resistance of the PZT-PZN Scheme4 cantilever beam is measured and simulated at the resonance frequency, 183 Hz. The dimension of the composite beam is 25 mm × 5.5 mm × 0.4 mm. The thickness of the middle Brass layer is 0.05 mm [14].

`

The left subplot plot in Figure 18 shows that the voltage increases as the external resistance R increases then voltage saturates. The reason for this phenomenon is the electric potential E is distributed by the internal resistance r of the piezoelectric beam and the resistance of the external resistor R by equation (48). As the external resistor R approaches to a large value, $\frac{R}{r+R}$ is getting close to 1; therefore, the voltage of the external load is approaching the electric potential E.

$$U = E\frac{R}{r+R} \tag{48}$$

The voltage U measured across the loading resistor R saturates at the electric potential E from the energy harvester as the external resistance R increases. The electric power of the external resistor initially increases because the rate of voltage U^2 (dominator) increase is faster than that of the external resistance R in equation (49). As the resistance R of the external resistor increases, the electric power consumed by the external resistor decreases after the initial increase; in other words, the term $r/\sqrt{R}$ decreases to zero when R approaches infinity, the electric power output has the expression of E^2/R.

$$P = \frac{U^2}{R} = \frac{E^2}{(\sqrt{R}+\frac{r}{\sqrt{R}})^2} \tag{49}$$

`

This phenomenon can also be explained by the impedance matching. In an electric circuit, the maximum electric power transfer occurs when the impedance of the source matches the impedance of the load in equation (50).

$$Z_{source} = Z_{Load} \tag{50}$$

The impedance includes the electric resistance, the capacitive reactance X_c, and the inductive reactance X_L which are calculated in equation (51). The capacitive reactance X_c and the inductive reactance X_L are sensitive to the frequency of the alternating electric signal.

$$X_c = \frac{1}{2\pi f C} \ , \quad X_L = 2\pi f L \tag{51}$$

f is the frequency of the alternating electric signal; C is the capacitance and L is the inductance. In this research, we are only matching the internal resistance with the external resistance to maximize the electrical power transfer from the source to the load. The plots show that our voltage and electric power results are consistent with the experimental data reported by other researcher's published work [15] over the same PZT-PZN Scheme4 piezoelectric material and the same dimension of a single rectangular composite bimorph piezoelectric beam. As can be seen in Figure 17, the value of our simulated voltage and measured voltage is fitted well. The maximum average electric power is at the same level between the simulated average electric power and the measured average electric power. Therefore, our simulation model is validated by the experimentally measured data.

`

3.3 MODELING MULTI-BEAM PIEZOELECTRIC ENERGY HARVESTER

3.3.1 Overview

The multi-beam is a natural and popular approach to widen the piezoelectric VEHs' vibrational frequency bandwidth. The multi-beam's dimensions are listed in Table 3.

Table 3. Length, width, thickness, and the resonance frequency of the linear elastic composite five-beam system with a common composite base without a tip mass

		Thickness	
Length	Width	2Tp+Ts	Resonance frequency
44mm	10mm	0.55mm	126.86Hz
48mm	10mm	0.55mm	107.67Hz
52mm	10mm	0.55mm	91.79Hz
56mm	10mm	0.55mm	78.33Hz
60mm	10mm	0.55mm	68.303Hz

The average resonance frequency of the five-beam system in Table 3 is 94.57 Hz, and the broadband voltage response is observed. The distance between each pair of beams is kept at 10 mm. T_p is the thickness of one PZN-PZT layer; T_s is the thickness of the UNS C22000 Brass layer; $2T_p+T_s$ is the total thickness of the composite bimorph beam.

3.3.2 Summary

The strategy to find the maximum electric power output is: find the first resonance frequency (68.303 Hz) of the beam. Once the first resonance frequency of the beam is known, the external resistance was varied from 0.01 MΩ to 0.03 MΩ with a 0.001 MΩ resolution; optimal resistance is found at 0.025 MΩ.

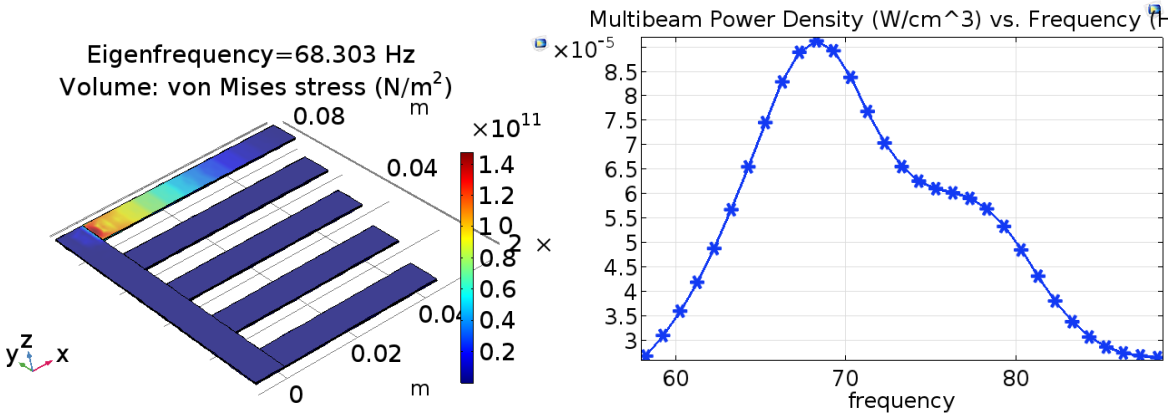

Figure 19. (Upper) Von Mises stress of a piezoelectric five-beam system connected by a common beam using the same PZT-PZN Scheme4 composite material and vibrating at the first resonance frequency at 68.3 Hz in 238078 elements in the extremely fine mesh of 1.3 cm^3 with 0g tip mass boundary condition on the edge of all free end of the five-beam system. The

dimension of the base is 8 mm × 90 mm × 0.55 mm [3].

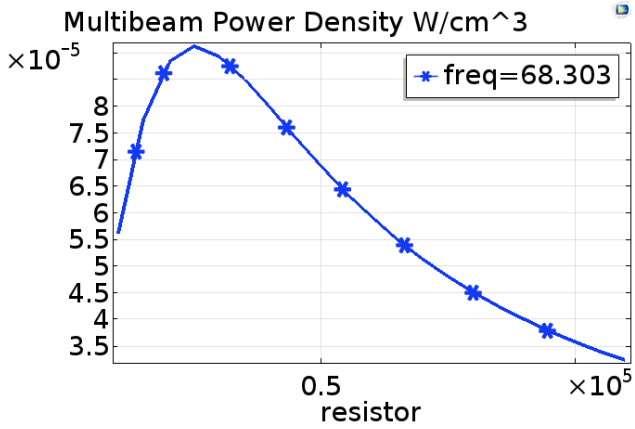

Figure 20. The piezoelectric multi-beam's electric power density in a range of the resistive load from 0.01 MΩ to 0.11 MΩ with a resolution of 0.005 MΩ under the first resonance frequency at 68.303 Hz; the peak electric power density is at 0.0913 mW/cm^3. The optimal resistance found at 0.025 MΩ.

With the optimal resistance found at 0.025 MΩ under the first resonance frequency at 68.303 Hz, the electric power density-frequency response was observed from 58.303 Hz to 78.303 Hz with a 1 Hz interval and can be seen in Figure 20 with the optimal 0.025 MΩ resistor loaded in an electric circuit. When the system is vibrating at 68.303 Hz, the maximum Von Mises stress is shown at the fixed end of the longest 60 mm beam in Figure 20. The volume of the five-beam system is 1.3 cm^3. The electric power density of the five-beam reaches a maximum of 0.0913 mW/cm^3 (0.119 mW) when vibrating at 68.303 Hz with the optimal resistor 0.025 MΩ connected in the series configuration. The full-width half-maximum bandwidth (FWHM) of the electric power density is found by scanning the vibration frequency around the first

resonance frequency of the five-beam system: the scan ranges from 58.303 Hz to 88.303 Hz with a 1 Hz interval. The system reaches the minimum half electric power density 0.0456 mW/cm^3 when vibrating 62.303 Hz and 80.303 Hz and reaches peak electric power density 0.0913 mW/cm^3 at the first resonance frequency at 68.303 Hz; therefore, the FWHM electric power density bandwidth of the five-beam system is 18 Hz (62.303 Hz - 80.303 Hz). Based on the results of the single and the multi-rectangular beam models, we further explored other nonlinear broadband energy harvesting device designs such as the one-piece trapezoidal beam designs as they are shown in Figure 21.

3.4 MODELING ONE-PIECE TRAPEZOIDAL PIEZOELECTRIC ENERGY HARVESTER

3.4.1 Overview

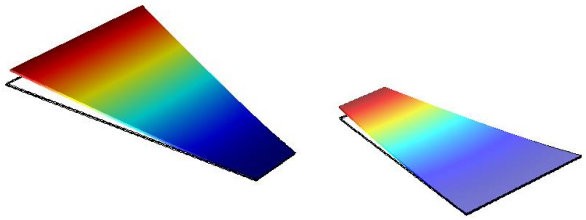

Figure 21. The displacement of two different trapezoidal piezoelectric bimorph beam designs shows that they vibrate at the first resonance frequency. The left subplot is the first design. The right subplot is the second design. The shorter width W_1 is 20 mm, the longer width W_2 is 60

mm. Both one-piece trapezoidal designs have 0g tip mass boundary conditions on the edge of the free end (warm color area). The other end of the beam is fixed on the blue colored area [3].

The investigation method to reveal the character of the mechanical vibration-electric power density bandwidth of the one-piece trapezoidal beam design is the same as mentioned. In this work, we treat the shorter width W_1 from 2 mm to 18 mm in steps of 4 mm and the longer width W_2 from 40 mm to 60 mm in steps of 4 mm as two independent variables and treat the fixed length at 60 mm and thickness at 0.55 mm as constant. Two views of the one-piece trapezoidal composite beam design are shown in Figure 22 and Figure 23 [3].

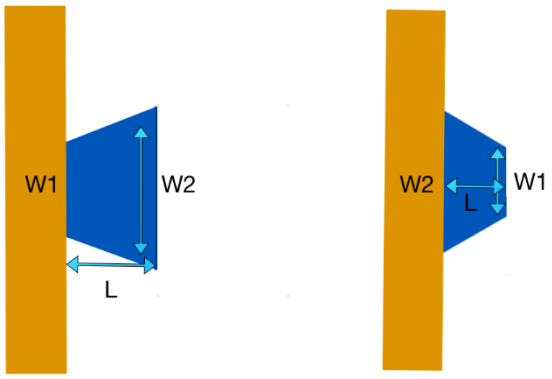

Figure 22. Top-down view of the one-piece bimorph piezoelectric trapezoidal beam. The left subplot is the first design, and the right subplot is the second design. W_1 is a shorter width. W_2 is the longer width [3].

Figure 23. Thickness view of the composite multi-beam and the one-piece trapezoidal beam's upper and lower PZT-PZN Scheme4 layers [3].

The Full-Width Half-Maximum (FWHM) bandwidth of the electrical power-mechanical vibration frequency study was investigated for the two one-piece trapezoidal beam designs by simulating 30 different discrete dimensions using variable short width W_1 from 2 mm to 18 mm in steps of 4 mm, the long width W_2 from 40 mm to 60 mm in steps of 4 mm, the fixed-length L at 60 mm, and the fixed thickness T at 0.55 mm.

3.4.2 Summary

The first resonance frequency increases as the shorter widths of the beam increases as the pattern is shown in Figure 24 and Figure 25: among 30 trapezoidal permutations of geometries for each trapezoidal piezoelectric composite bimorph beam design, the average resonance frequency of the first trapezoidal beam design is 33 Hz and the average resonance frequency of the second trapezoidal beam design is 58 Hz. This indicates that the first trapezoidal beam design is suitable for harvesting lower vibration frequency applications, whereas the second trapezoidal beam design is suitable for harvesting higher vibration frequency applications.

`

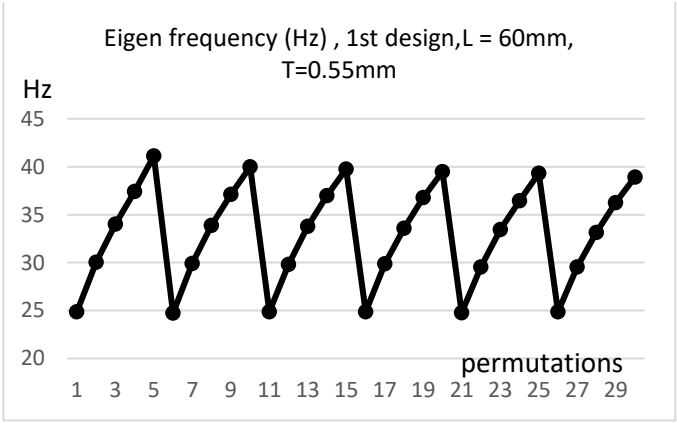

Figure 24. Resonance frequency vs. 30 permutations of the first trapezoidal piezoelectric composite bimorph beam design.

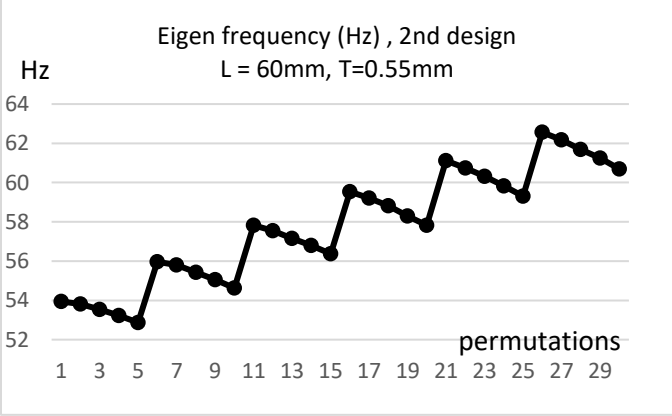

Figure 25. Resonance frequency vs. 30 permutations of the second trapezoidal piezoelectric composite bimorph beam design.

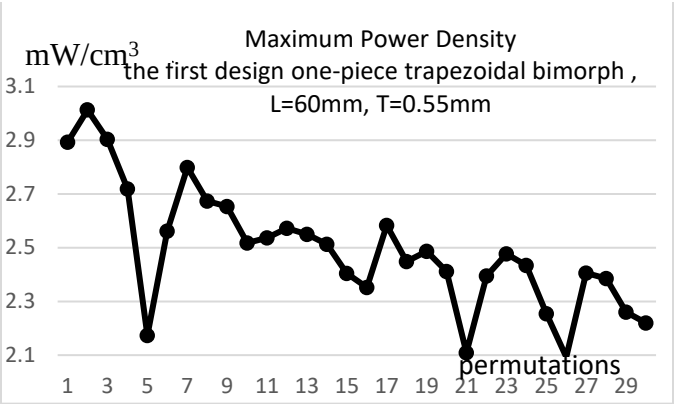

Figure 26. Maximum electrical power density vs. 30 various geometries of the first trapezoidal composite piezoelectric bimorph beam in a closed circuit with the corresponding optimal resistor load. 30 various geometries originated from changing W_1 from 2 mm to 18 mm in steps of 4 mm and changing W_2 from 40 mm to 60 mm in steps of 4 mm.

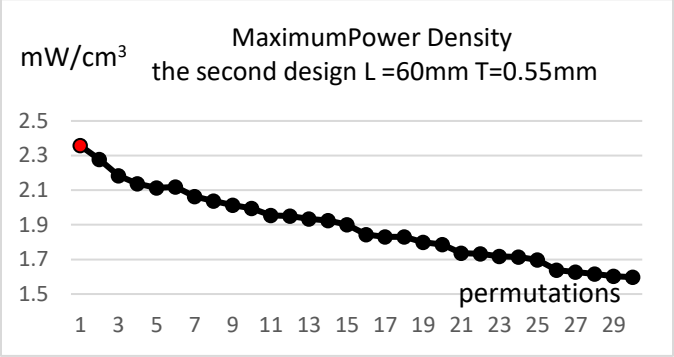

Figure 27. The maximum electrical power density of 30 various geometries of the second trapezoidal composite piezoelectric bimorph beam in a closed circuit with the corresponding optimal resistor load. 30 various geometries originated from changing W_1 from 2 mm to 18

mm in steps of 4 mm and changing W_2 from 40 mm to 60 mm in steps of 4 mm.

The maximum electric power density is defined by the unit electric power consumed by the corresponding optimal resistor connected in the closed circuit. Both trapezoidal designs share a similar pattern as shown in Figure 26 and Figure 27: the electric power in the y-axis decreases as W_1 and W_2 of the beam increases along the x-axis. The length of each trapezoidal beam is fixed at 60 mm, and the thickness of the beam is fixed at 0.55 mm. The maximum electrical power density reaches 3.01 mW/cm^3 (volume is 0.72 cm^3 and generated electric power is 2.167 mW) for the first trapezoidal composite beam design when W_1 reaches 8 mm and W_2 reaches 40 mm with the optimal resistor load 60 kΩ. The maximum electric real power density reaches 2.36 mW/cm^3 (volume is 0.66 cm^3 and generated electric power is 1.558 mW) for the second trapezoidal composite beam design when W_1 reaches 4 mm and W_2 reaches 40 mm with the optimal resistor load 60 kΩ as shown in Figure 26 and Figure 27. The reason for the largest maximum electric power density appears at the beginning of the geometry permutation plots of both one-piece trapezoidal composite piezoelectric bimorph beam design is that the maximum electric real power density is more sensitive to the volume of the beam than any other factors. The optimal resistance scan ranges from 10 kΩ to 500 kΩ with an interval of 25 kΩ for all 30 permutations of both trapezoidal piezoelectric bimorph beam designs. The maximum electric power density is compared between both trapezoidal piezoelectric bimorph beam designs due to the fairness of performance comparison, which is to take the size (volume) out of the consideration.

`

To better describe the bandwidth performance of the trapezoidal beam, the Full-Width Half-Maximum (FWHM) bandwidth of real electrical power is evaluated on both trapezoidal beam designs: the length L is fixed at 60 mm, the composite thickness T is fixed at 0.55 mm, and the Full-Width Half-Maximum (FWHM) bandwidth of electrical power is determined by scanning +/- 5Hz with 1 Hz interval around the first resonance frequency with the optimal resistance fixed in each corresponding widths (W_1, W_2) geometry permutation of the trapezoidal beam as shown in Figure 28 and Figure 29.

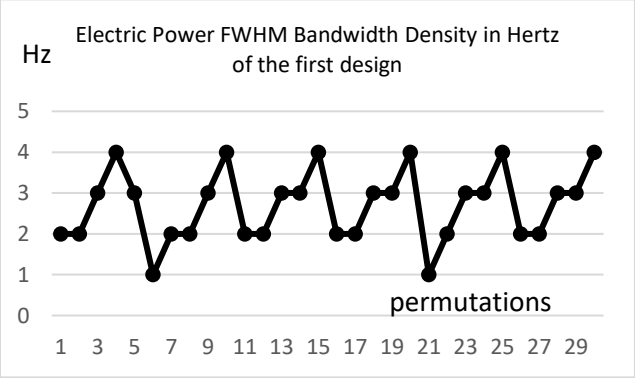

Figure 28. The FWHM bandwidth of the electrical power density of 30 various geometries of the first one-piece trapezoidal composite piezoelectric bimorph beam design in a closed circuit with the corresponding optimal resistor load fixed. 30 various geometries originated from changing W_1 from 2 mm to 18 mm in steps of 4 mm and changing W_2 from 40 mm to 60 mm in steps of 4 mm.

For the first trapezoidal design, the average vibration bandwidth of power density FWHM bandwidth of 30 geometry permutations is 2.7 Hz. The maximum vibration

bandwidth is 4 Hz (the minimum electric power density is 1.066 mW/cm^3; the maximum electric power density is 2.517 mW/cm^3; W_1 is 20 mm; W_2 is 44 mm; the volume is 0.96 cm^3; the electric power is 2.42 mW) and the minimum vibration bandwidth is 1 Hz (the minimum power density 0.966 mW/cm^3; the maximum power density is 1.898 mW/cm^3) as shown in Figure 28.

For the second trapezoidal design, the average vibration FWHM bandwidth of the electric power density of 30 geometry permutations is 5.3 Hz. The maximum vibration bandwidth is 6 Hz (the minimum power density is 0.799 mW/cm^3 and the maximum power density is 2.0415 mW/cm^3; W_1 is 12 mm; W_2 is 40 mm; the volume is 0.78 cm^3; the electric power is 1.59 mW) and the minimum vibration bandwidth is 4 Hz (the minimum power density 1.139 mW/cm^3; the maximum power density 2.356 mW/cm^3) as shown in Figure 29. The second beam design's electric power density FWHM bandwidth is less sensitive to the discrete geometry increments than the other designs, which contribute to the shape of Figure 29. The key comparison of the multi-beam design and the trapezoidal designs is tabulated in Table 4, in which the multi-beam design has the best electric power density FWHM vibration bandwidth of 18 Hz, whereas the first one-piece trapezoidal beam design has the better minimum power density of 1.066 mW/cm^3 as well as the better maximum electric power density of 2.517 mW/cm^3.

`

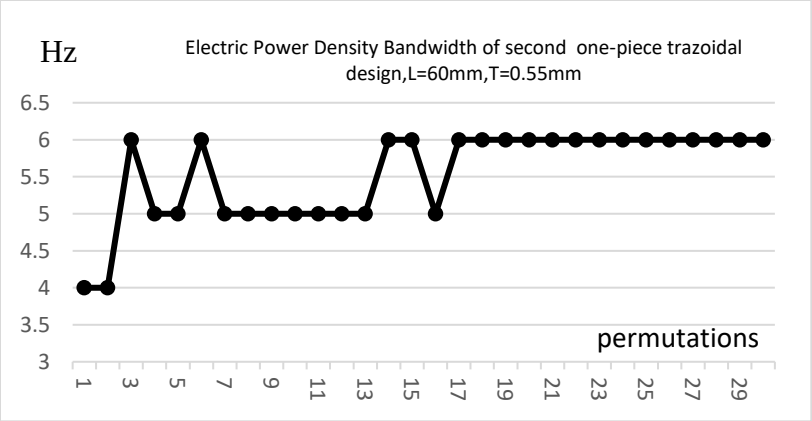

Figure 29. The electrical power density FWHM bandwidth vs. 30 various geometries of the second trapezoidal composite piezoelectric bimorph beam design in a closed circuit with the corresponding optimal resistor load fixed. 30 various geometries originated from changing W_1 from 2 mm to 18 mm in steps of 4 mm and changing W_2 from 40 mm to 60 mm in steps of 4 mm.

In conclusion, the multi-beam piezoelectric harvester generated 0.0913 mW/cm^3 electric power and offers wider bandwidth of 18 Hz than the trapezoidal beam designs (4 Hz to 6 Hz), yet the trapezoidal beam designs have a superior power density performance of 2.3 to 2.5 mW/cm^3. The simulation results tabulated in Table 4 show that the multi-beam approach and the one-piece trapezoidal piezoelectric beam approach are two of the promising approaches in designing high power density piezoelectric energy harvesters.

`

Table 4. FWHM bandwidth, the minimum, and maximum of the electric power density of the multi-beam and the one-piece trapezoidal beam

Design	Max. FWHM Bandwidth	*Min. Power Density*	*Max. Power Density*
multi-beam (5)	18 Hz	0.0456 mW/cm^3	0.0913 mW/cm^3
1st trapezoidal(1-peice)	4 Hz	1.066 mW/cm^3	2.517 mW/cm^3
2nd trapezoidal(1-peice)	6 Hz	0.799 mW/cm^3	2.356 mW/cm^3

Results of both one-piece trapezoidal VEHs' power density in Table 4 are higher than that of a rectangular-shaped composite beam (0.2676 mW/cm^3 predicted and 0.1713 mW/cm^3 measured and reported by Bedekar *et al.*) [15]. Yet the maximum power results (2.517 mW/cm^3) is slightly lower than that of Benasciutti *et al*. reported trapezoidal-shaped beam (3.9 mW/cm^3).

3.4.3 Validation through comparison

Not only have we verified and validated the voltage and the electric power data of the single rectangular composite bimorph piezoelectric beam by comparing our simulation results with the experimental results reported by other researchers [3] [15], but also verified and validated the

`

electric power density data of the one-piece trapezoidal composite bimorph piezoelectric beam design by comparing our results with the results reported by other researchers [15] [18] [19]. For instance, Rouhollah and Mohsen studied the "trapezoidal V-shaped" beam and proposed an analytical formula for the first resonance frequency for the rectangular beam and tapped beam: the authors showed that the analytical resonance frequency of the tapped beam is twice as much as that of the rectangular beam [18]. Yet Rouhollah and Mohsen did not discuss performance metrics such as the electrical energy performance, the operational bandwidth of the V-shaped beam, or the trapezoidal beam. Benasciutti *et al.* studied the trapezoidal and the reversed trapezoidal bimorph cantilever beams. The authors showed that the electric power density of the reversed trapezoidal beam is consistently higher than that of the trapezoidal, which agrees with our result of the maximum power density for our first trapezoidal beam design and the second trapezoidal beam design in this work [19]. Benasciutti *et al.* reported that the electric power density of the one-piece trapezoidal composite piezoelectric bimorph beam is about 5 mW/cm^3 and the electric power density of the one-piece reversed trapezoidal composite piezoelectric bimorph beam is about 10 mW/cm^3 [19]. Yet the piezoelectric material used in the two research projects is different: Benasciutti *et al.* did not include the electro-mechanical bandwidth result and used PSI-5A4E PZT material for their one-piece trapezoidal composite beam models. In theory, we could have predicted the bandwidth of Benasciutt's one-piece trapezoidal VEHs by using our existing modeling method. However, Poisson ratio of PSI-5A4E is missing in the literature, as a result we are not able to model the polycrystal PSI-5A4E PZT currently. While PZT-PZN-Scheme4 material is used in this work, we showed FWHM bandwidth of the electrical power-mechanical vibration of the one-piece trapezoidal composite beam design result as well as the maximum electrical power density results of our one-piece trapezoidal composite beam

designs of 7.26 mW/cm^3 and 10.37 mW/cm^3 [3]. The maximum electrical power density results of our one-piece trapezoidal composite beam designs are at the same level when we compared our electrical power density results with those from another researcher [19]. The small numerical difference between our power density results and those of other researchers is because two different piezoelectric materials were modeled: Benasciutti *et al.* used PSI-5A4E PZT material, whereas we used the PZTPZN-Scheme4 material. The electric power density and the FWHM bandwidth comparison data are tabulated in Table 5.

Table 5. The comparison of the electric power density and the FWHM bandwidth between our one-piece trapezoidal design and Benasciutti's one-piece trapezoidal beam design

Authors	Piezoelectri Material	Electric Power Density	Bandwidth
Benasciutti, et al	PSI-5A4E-PZT (A)	5 mW/cm^3	Not reported
Benasciutti, et al	PSI-5A4E-PZT (B)	10 mW/cm3	Not reported
Chen & Bedekar	PZT-PZN (A)	10.4 mW/cm3	2.9 Hz
Chen & Bedekar	PZT-PZN (B)	7.3 mW/cm3	2.5 Hz

3.5 MODELING TWO-PIECE TRAPEZOIDAL PIEZOELECTRIC ENERGY HARVESTER

3.5.1 Design of the two-piece trapezoidal piezoelectric energy harvester

We not only studied the bandwidth of mechanical vibration of the one-piece piezoelectric trapezoidal composite energy harvesting device designs [3] but also the two-piece piezoelectric trapezoidal composite beam designs. The non-linear two-piece trapezoidal shape is shown in two views in Figure 30 and Figure 31.

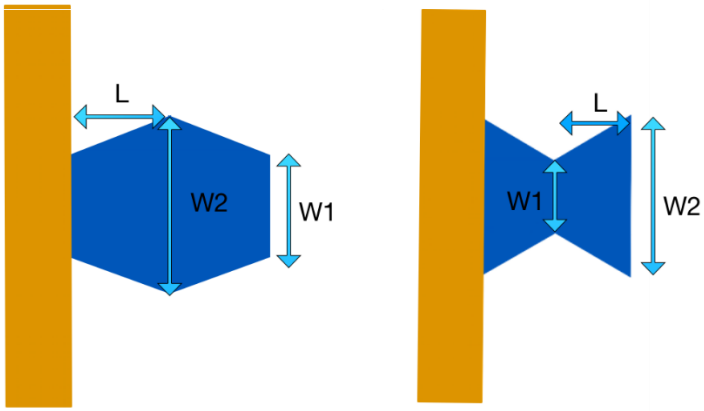

Figure 30. Top-down view of the two-piece piezoelectric trapezoidal beam. The left subplot is the first two-piece trapezoidal beam design, and the right subplot is the second two-piece trapezoidal beam design. W_1 is the shorter width. W_2 is the longer width. L is the length of one single plate. The longer width W_2 fixed at 40 mm, 44 mm, 48 mm, 52 mm, 56 mm, and 60 mm. The shorter width W_1 varies from 4 mm to 20 mm with a 4 mm interval [3].

The FWHM bandwidth of the mechanical vibration frequency is extracted from COMSOL's frequency study for two different two-piece trapezoidal beam designs by simulating 30 discretized geometries in the short width W_1 from 2 mm to 20 mm with 4 mm interval, the long width W_2 from 40 mm to 60 mm with 4 mm internal, a fixed-length L at 60 mm, and the thickness T at 0.55 mm. Figure 31 shows a detailed 2-D dimension of the two-piece trapezoidal design.

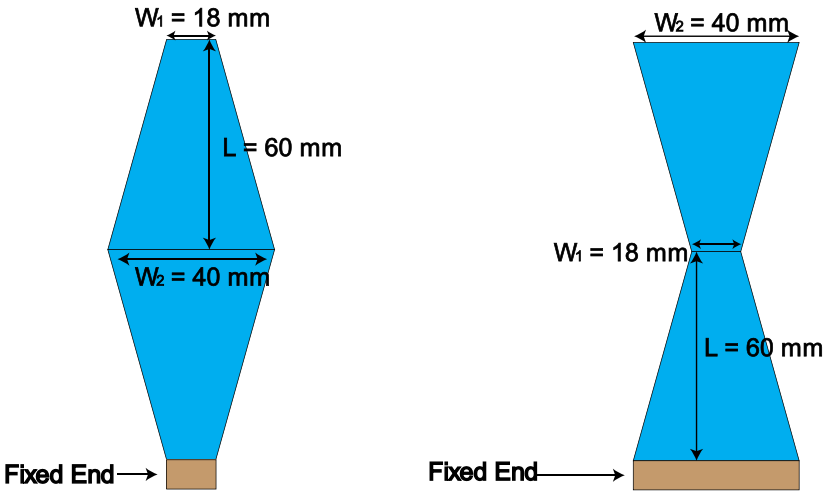

Figure 31. The top-down view of the two-piece piezoelectric trapezoidal beam designs. The left subplot is the first two-piece trapezoidal beam design and the right subplot is the second two-piece trapezoidal beam design. W_1 is the shorter width, W_2 is the longer width, and L is the length of one single plate [4].

`

3.5.2 Results and discussion

The first design of the two-piece piezoelectric trapezoidal beam is shown in the left subplot of Figure 31. The volume of the two-piece trapezoidal beam ranges from 1.638 cm^3 to 3.042 cm^3 as the widths of the beam grow [4]. The electric power density of the beam reaches a maximum of 19.595 mW/cm^3 or 38.044 mW in the electric power when the shorter width W_1 is 2 mm and the longer width W_2 is 56 mm [14]. The beam vibrates at the first resonance frequency at 13.7 Hz with the optimal resistor 0.14 MΩ connected in series. The maximum FWHM mechanical vibration bandwidth of the real electric power density is found through iterating 30 discretized geometries for the first resonance frequency. For example, a beam with 40 mm W_1 and 18 mm W_2 has 20.0 Hz first resonance frequency in the eigenfrequency analysis. We kept the same first resonance frequency at 20.0 Hz and found an optimal resistor 0.08 MΩ by a parametric study on the resistor. We kept the optimal resistor 0.08 MΩ and set up a parametric vibration frequency study, in which the frequency ranges from 0.9 f_r (18.0 Hz) to 1.1 f_r (22.0 Hz) with 0.1 Hz interval [4]. The beam's vibration generates the minimum electric power density 3.6327 mW/cm^3 or 15.17 mW in the electric power when vibrating between 19.5 Hz and 22.0 Hz [4]; it reaches a peak electric power 15.17 mW at the frequency close to the first resonance frequency at 20.767 Hz; therefore, the electric power density FWHM bandwidth of the two-piece trapezoidal beam is 2.5Hz. The voltage-frequency plot and the electric power-frequency plot are shown in Figure 32 [4].

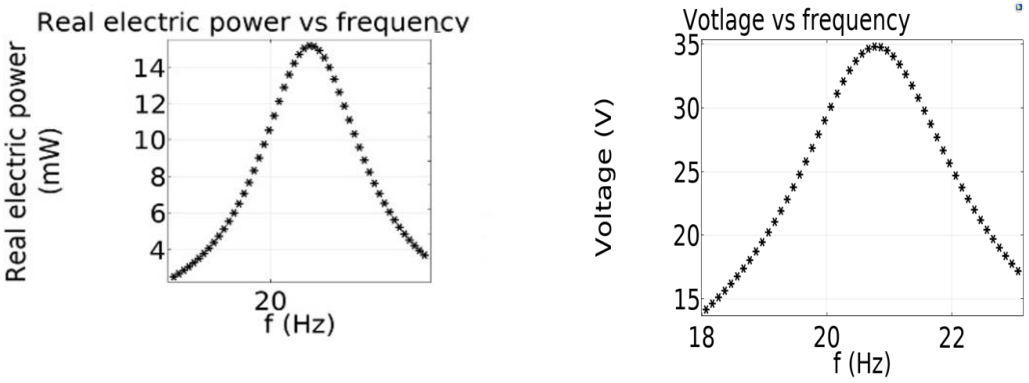

Figure 32. The electric power output vs. the mechanical vibration frequency of the **first** trapezoidal bimorph two-piece design on the left plot. Voltage vs vibration frequency of the **first** trapezoidal bimorph two-piece design on the right plot. W_1 is 40 mm, W_2 is 18 mm. The full-width half-maximum is 2.5 Hz. The quality factor is 28. The structural loss factor is 0.025. The damping ratio is 0.017. The optimal resistance is 0.08 MΩ. The length of the beam L is 60 mm; the thickness of T_{piezo} is 0.3 mm; the thickness of the brass layer T_s is 0.05 mm.

The second design of the two-piece trapezoidal beam is shown in the right subplot of Figure 33. The volume of the two-piece trapezoidal beam ranges from 1.638 cm^3 to 3.042 cm^3 as the widths of the beam grow [4]. The electric power density of the beam has a maximum of 43.52 mW/cm^3 (97.136 mW), when the shorter width of the bimorph W_1 is 2 mm, the longer width of the bimorph W_2 is 60 mm [4]. For example, a beam with 52 mm W_1 and 18mm W_2 has the first resonance frequency of 15.1 Hz in the eigenfrequency analysis. We kept the same first resonance frequency 15.1 Hz and found an optimal resistor 0.07 MΩ by a parametric frequency study on the resistor. We kept the optimal resistor 0.07 MΩ and set up a parametric vibration frequency study, in which the mechanical vibration frequency ranges from 0.9 f_r

(13.6 Hz) to 1.1 f_r (16.6 Hz) with 0.1 Hz interval [4]. The voltage-frequency plot and the electric power-frequency plots are shown in Figure 33 [4].

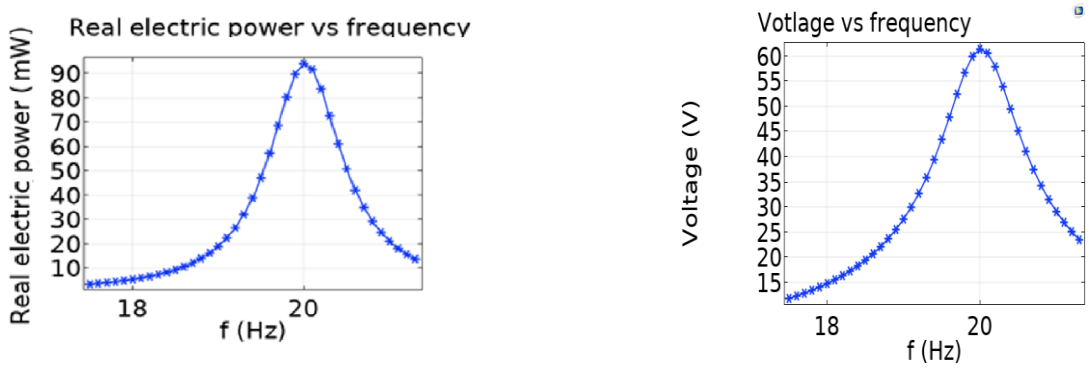

Figure 33. Electric power output vs. vibration frequency of the **second** trapezoidal bimorph two-piece design on the left plot. Voltage vs vibration frequency of the **second** trapezoidal bimorph two-piece design on the right plot. W_1 is 40mm, W_2 is 18 mm. The full-width half-maximum is 2.5 Hz. The quality factor is 28. The structure loss factor is 0.025. The damping ratio is 0.017. The optimal resistance is 0.08 MΩ. The length of the beam L is 60 mm; the thickness of T_{piezo} is 0.3 mm; the thickness of the brass layer T_s is 0.05 mm [4].

The two-piece trapezoidal beam designs have shown the potential to increase the energy harvester's electric power output and the frequency bandwidth, although the FWHM bandwidth of the one-piece trapezoidal composite beams shows its results to the designing of a broadband energy harvesters [3]. The displacement of 2 two-piece trapezoidal beam designs which are shown in Figure 34 [4].

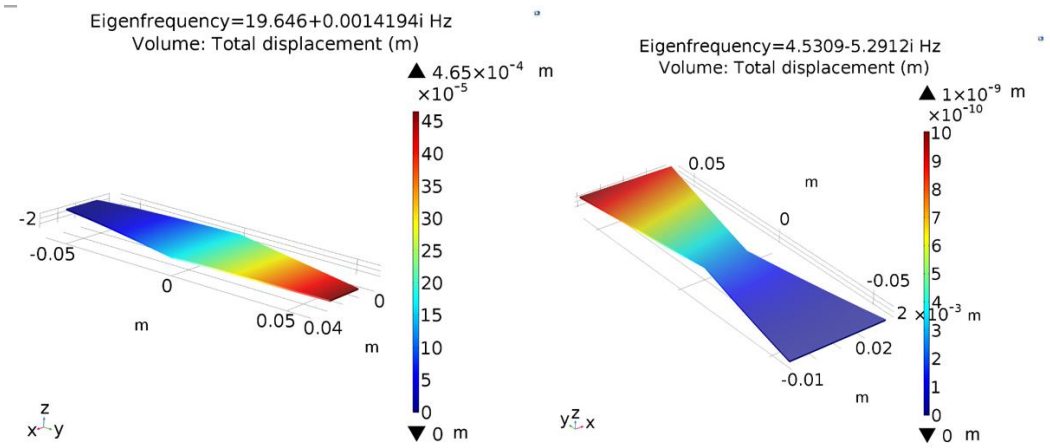

Figure 34. The displacement of two different two-piece trapezoidal piezoelectric bimorph beam which vibrates at its first resonance frequency. The left subplot is the stationary displacement with no deformation of the **first** design. The right subplot is the stationary displacement with the deformation of **the second** design. The shorter width W_1 is 18 mm, and the longer width W_2 is 40 mm for both two bimorph designs. The length of the beam L is 60 mm; the thickness of T_{piezo} is 0.3 mm; the thickness of the brass layer T_s is 0.05 mm [4].

The first design of the two-piece piezoelectric trapezoidal beam's average resonance frequency of thirty discretized geometry is 17.6 Hz. For the second design, the average resonance frequency of thirty discretized geometries of the two-piece trapezoidal beams is 17.9 Hz. T_p is the thickness of one PZT-PZN layer [4]. T_s is the thickness of the UNS C22000 Brass layer. $2T_p+T_s$ are the total thickness of the composite piezoelectric bimorph as shown in Figure 35 [4].

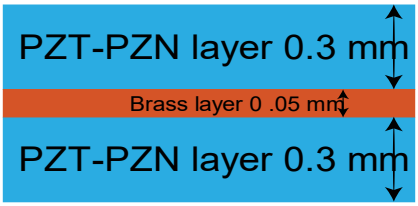

Figure 35. The thickness view of the composite two-piece trapezoidal beam's upper and lower PZT-PZN Scheme4 layer for both two bimorph designs. The length of the beam L is 60 mm; the thickness of T_{piezo} is 0.3 mm; the thickness of the brass layer T_s is 0.05 mm [4].

The maximum FWHM bandwidth is 2.5 Hz, the minimum power density is 3.63 mW/cm^3, the maximum electric power density is 7.27 mW/cm^3 when the shorter width W_1 is 40 mm and the longer width W_2 is 18 mm. The structural volume of the bimorph is 2.262 cm^3. The output of electric power is 7.27 mW. For the second two-piece trapezoidal design, the maximum FWHM bandwidth is 1.1 Hz, the minimum power density 18.66 mW/cm^3, and the maximum electric power density 37.32 mW/cm^3 when the shorter width W_1 is 18 mm and the longer width W_2 is 52 mm. The structural volume is 2.73 cm^3 and the electric power is 94.04 mW. The electric power density increases FWHM bandwidth when the shorter width W_1 of the bimorph increases as they are shown in Figure 36 and Figure 37. We have not seen any existing paper on a two-piece trapezoidal composite harvesting device published in the literature to date. Therefore, we have published our results to the *Journal of Advances in Materials Science and Engineering (AMSE)* in January 2020. The Full-Width Half-Maximum bandwidth of the

electro-mechanical frequency response of 30 different two-piece trapezoidal beams is shown in Figure 36 and Figure 37.

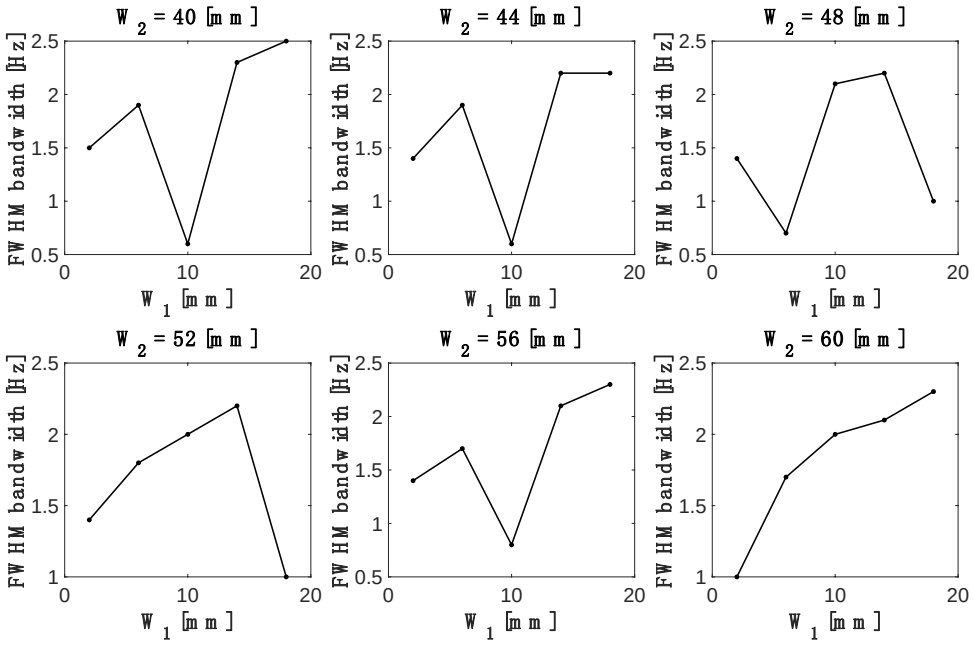

Figure 36. The electrical power density FWHM bandwidth vs. 30 various geometries of the one-piece trapezoidal composite piezoelectric bimorph of the first design in a closed electric circuit with the corresponding optimal resistor load. The longer width W_2 fixed at 40 mm, 44 mm, 48 mm, 52 mm, 56 mm, and 60 mm. The shorter width W_1 varies from 4 mm to 18 mm with a 4 mm interval.

Figure 36 shows the electric-mechanical FWHM bandwidth of the one-piece trapezoidal beam increased from as the short width W_1 increased from 4 mm to 20 mm with a 4 mm interval. It indicates that an increase in the shorter width W_1 is an effective strategy to increase the electro-mechanical bandwidth for the first two-piece trapezoidal designs.

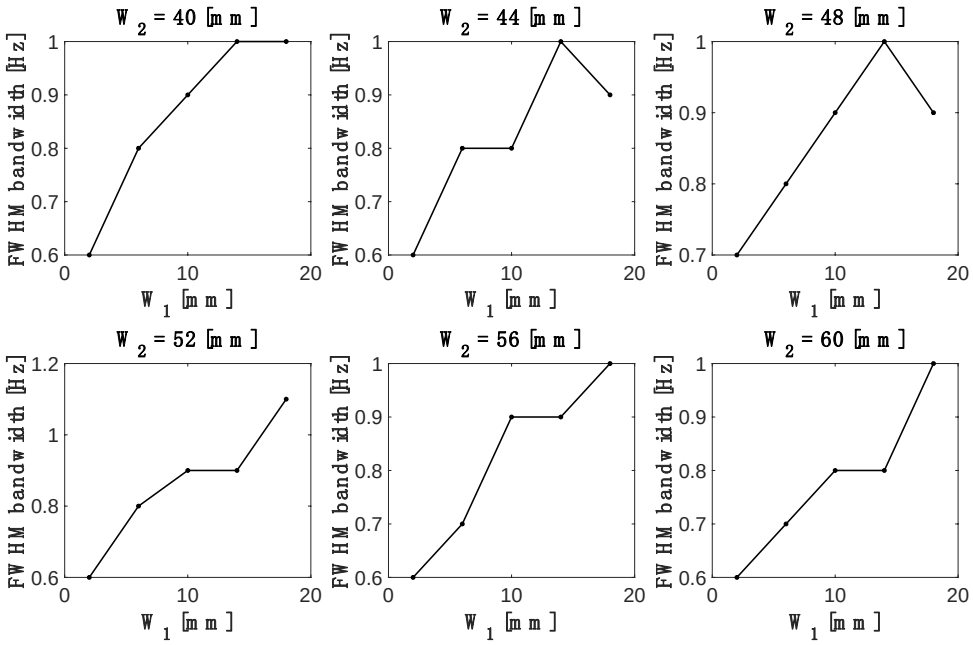

Figure 37. The electrical power density FWHM bandwidth vs. 30 various geometries of the second (bowtie shaped) design two-piece trapezoidal composite piezoelectric bimorph design in a closed electric circuit with the corresponding optimal resistor load. The longer width W_2 fixed at 40 mm, 44 mm, 48 mm, 52 mm, 56 mm, and 60 mm. The shorter width W_1 varies from 4 mm to 18 mm with a 4 mm interval.

Figure 37 shows the FWHM electrical power density bandwidth of the two-piece trapezoidal beam increased as the short width W_1 increased from 4 mm to 18 mm. It indicates that an increase in W_1 is also an effective strategy to increase the mechanical vibration bandwidth for the second two-piece trapezoidal design.

`

3.5.3 Validation through comparison

In this manuscript, we explained two different tactics to increase the mechanical vibration bandwidth in the multi-beam approach and the trapezoidal shape approach. The trapezoidal designs have higher electric power density performance due to its non-linear shape. The mechanical vibration frequency bandwidth of a piezoelectric energy harvester is related to many factors: the shape, dimension, and the material property of the device. We have published our third manuscript on the two-piece trapezoidal composite piezoelectric beam to *the Journal of Advances in Materials Science and Engineering* in January 2020. The results show the increased mechanical vibration frequency bandwidth of two different two-piece trapezoidal composite piezoelectric beam designs. Table 6 shows the tabulated results of the Full-Width Half-Maximum electric power density bandwidth of three different composite piezoelectric energy harvesting bimorph designs: the multi-beam, the one-piece trapezoidal, and the two-piece trapezoidal beam design. Liu *et al.* claimed the bandwidth of their multi-beam design is 8 Hz from 226 Hz to 234 Hz [10]. Our electric power density bandwidth of the multi-beam design is 18 Hz which is 125 % wider than that of Liu's bandwidth results as seen from Table 6. Wu *et al.* reported that the bandwidth of their multi-beam design is 12 Hz from 13 Hz to 25 Hz [9]. Our electric power density bandwidth of the multi-beam design is 18 Hz, which is 50 % wider than Wu's bandwidth results as we can see from Table 6. For the nonlinear piezoelectric VEH models, we provided the FWHM bandwidth and the minimum power density data for the one-piece trapezoidal models where these data are missing in the literature [18] [19]. No two-piece trapezoidal simulation model has been studied or published to date. Therefore, we have published our results of the two-piece trapezoidal VEH models to the *Journal of Advances in Materials Science and Engineering* in February 2020 [31].

`

Table 6 FWHM bandwidth, the minimum, maximum electric power density of various energy harvester beam [3]

	Max. FWHM Bandwidth	*Range*	*Min. Power Density*	*Max. Power Density*
Our multi-beam design [3]	18Hz	62.3 - 80.3 Hz	0.0456 mW/cm^3	0.0913 mW/cm^3
Liu *et al.*'s multi-beam design [10]	8 Hz	226 - 234 Hz	N/A	N/A
Wu *et al.'s* multi-beam design [7]	12Hz	13 - 25 Hz	N/A	N/A
Our 1st trapezoidal design (1-piece) [3]	2.9Hz		5.18 mW/cm^3	10.37 mW/cm^3
1st trapezoidal design (1-piece) proposed by Benasciutti *et al.* [19]	N/A		N/A	5 mW/cm^3
Our 2nd trapezoidal design (1-piece) [3]	5.6Hz		2.11 mW/cm^3	4.22 mW/cm^3
2nd trapezoidal design (1-piece) proposed by Benasciutti *et al.* [19]	N/A		N/A	10 mW/cm^3
Our 1st trapezoidal design (2-piece)	2.5Hz	19.5 – 22 Hz	3.63 mW/cm^3	7.26 mW/cm^3
Our 2nd trapezoidal design (2-piece)	1.1Hz	19.5– 20.6 Hz	8.4 mW/cm^3	16.81mW/cm^3

The results from Table 6 also show that the one-piece trapezoidal beam design has the widest 5.6 Hz mechanical vibration-electric power density bandwidth response among the three different designs, yet the electric power density of the two-piece trapezoidal beam design shows its superiority to other broadband energy harvester designs. The maximum power density is 16.81 mW/cm^3 of the second design of the two-piece trapezoidal bimorph.

`

CHAPTER 4: MAGNETOELECTRIC ENERGY HARVESTER

4.1 INTRODUCTION

The magnetostriction effect was discovered by James Joule in 1842 when he found that the nickel sample's shape changes when a magnetic field was applied. Virtually all materials have magnetostriction properties, as materials are made of atoms, the spins and rotations of atoms' unpaired electrons are sources of the magnetic dipole moments in the domains of the magnetic materials [32]. When magnetoelectric material changes shape in a magnetic field, it converts the magnetic energy to the elastic energy in the magnetostrictive material [33]. It is a convention to define the magnetostrictive material as the absolute value of the saturation magnetostriction constant λ_s greater than 50 ppm (parts per million) [32]. The saturation magnetostriction λ_s is the ratio $\Delta\lambda/\lambda$ between the change of the length $\Delta\lambda$ and the original length of material λ. Fe, Co, and Ni are the earliest discovered magnetostrictive materials. There are two unpaired electrons in the 3-d orbital for Ni atom. We studied the performance of the metallic nickel Ni through our simulation models. The pure metallic nickel was the earliest magnetostriction material discovered in the 1920s, which has the negative saturation magnetostriction constant λ_s of -50 ppm [32]. During the 1930s and 1940s, the researchers studied the magnetostrictive properties of iron, cobalt and their alloys: the saturation magnetostriction constant λ_s of 70%Co-30%Fe polycrystal alloy is 130 ppm under the magnetic field of 1.12×10^5 A/m [32]. Metglas was developed in the 1970s, which is an amorphous metal alloy, has an extremely high relative

magnetic permeability around 10,000 in the low frequency at 1 kHz, due to the magnetic flux concentration effect [33], but it has very little saturation magnetostriction about 1 ppm. In the 1980s, Clark *et al.* at the Naval Ordnance Laboratory (NOL), discovered an alloy named Terfenol-D ($Tb_{0.3}\,Dy_{0.7}\,Fe_2$) which is made of two rare-earth atoms: Terbium, Dysprosium and iron in its chemical composition. Terfenol-D can produce a super magnetostrictive effect due to its extremely large saturation magnetostriction constant λ_s from 1200 to 2000 ppm in room-temperature under a large magnetic field of 1.6×10^6 A/m [32]. In this study, we focus on using the negative magnetostrictive material: nickel, as it was one of the earliest developed magnetostrictive materials. Nickel is a soft ferromagnetic material, which indicates it has a low coercivity H_c and therefore a smaller area of a magnetic hysteresis loop [32].

The piezoelectric effect is traditionally known as one of the methods to harvest the vibration energy, as the vibration generates the mechanical strain and stress in the piezoelectric material. In the field of the energy harvesters' design, there are two main challenges: (i) low output electric power density, and (ii) narrow vibrational frequency response [34]. The traditional linear piezoelectric vibrational energy harvester (VEH) suffers from a problem: the VEH only operates at its resonance frequency when the vibration frequency shifts from its resonance, the voltage and the electric power output drops significantly. To overcome these issues, researchers have been investigating new VEH designs from two sources: the stray vibration and the ambient magnetic field. The stray vibration is ubiquitous from moving objects: such as automobiles, machinery, human, and animals. The ambient magnetic field comes from a wide range of places: the geomagnetic field of the earth: 0.25 to 0.65 Oe; the area near computer monitor the magnetic field reaches 0.2 to 135 Oe with 1 foot away; the places near a desktop light the magnetic field

reaches 32.8 Oe with 1 foot away; The stray vibration and the ambient magnetic field would be otherwise wasted energy sources where the free energy is waiting to be collected. The coupled piezoelectric and magnetostrictive effects provided us a venue to save the ubiquitous energy from waste. Such a coupled effect is known as the magnetoelectric (ME) effect, as the mechanical stress not only comes from the vibration but also comes from the ambient magnetic field, which is transferred from the magnetostrictive material such as Ni to the piezoelectric material. The magnetoelectric materials are used in the electric current sensors, energy harvesters, magnetoelectric random access memory (MeRAM), and ME antennas [35]. With such a wide range of applications of ME materials, we focus on enhancing the output electric power and the vibrational bandwidth of the energy harvesters through the non-linear ME trapezoidal design. Recently, researchers studied the dual-mode energy harvesters and reported that they have found improved results of harvesting energy from the mechanical vibration and the magnetic field [36] [37]. By operating the energy harvester in an environment with an ambient vibration and the stray magnetic fields, an ideal energy harvester should not only convert the mechanical energy from the vibration but also the magnetic field via the coupled piezoelectric and magnetostrictive effects through bonding in a laminated ME composite structure [38]. To gauge the performance of the ME vibration energy harvester, the magnetoelectric voltage coefficient α is widely reported in the literature [32] [39], from which we know that the magnetoelectric voltage coefficient α is much higher when the magnetoelectric energy harvester vibrates at the first resonance frequency. Besides, Ramos *et al.* found that the magnetoelectric voltage coefficient α of a multi-layer composite structure does not increase as the number of layers above five layers [40]. Park *et al.* reported that there is an optimal number of the magnetostrictive layers (thickness) when a VEH operates in a low bias magnetic field H_{dc}, while

`

VEH exhibits a large coefficient α [41]. Bichurin *et al*. proposed a pair of the analytical formula for the transverse and the thickness magnetoelectric voltage coefficients α_{31} and α_{33}, and they found that the transverse magnetoelectric voltage coefficient α_{31} is twice as much as the thickness voltage coefficient α_{33} of CFO-PZT and NFO-PZT laminated composite beam when the volume ratio of the piezoelectric and the magnetostrictive material is 1:1. Since the 3-3 mode is widely used in ME sensor applications and the 3-1 mode is often used in the vibrational applications, we would like to have the magnetoelectric voltage coefficient α_{31} as large as possible when the device operates in the 3-1 mode. Applying a static DC external magnetic field along the thickness direction of the bimorph would require a larger DC external magnetic field to reach the saturation magnetization of the magnetostrictive layer, therefore we apply the magnetic field in the transverse direction of a beam. The transverse magnetoelectric voltage coefficient is defined as $\alpha_{31} = \frac{\partial E_3}{\partial H_1}$, where ∂E is the change of the electric field in z direction as the result of the change of the magnetic field ∂H along x-direction [35]. Ramos *et al*. also pointed out that the simulation result of α_{31}-H_{dc} is much higher than the experimental data due to the strain relaxation between the piezoelectric layer and the magnetostrictive layer [40]. There were a few recent types of research that focus on improving the broadband vibrational frequency bandwidth. Lin *et al.*'s 3D ME energy harvester reported having an open voltage bandwidth of 2.1 Hz [42]. Yang *et al.* proposed a series-connected two rectangular composite cantilever beam has 5.6 Hz bandwidth with a maximum electric output power 0.25 mW at the acceleration of 1g (g is 9.8 m/s^2) [12]. S. D. Patil reported a sandwiched Metglas/BTO/Metglas cantilever beam reached a higher α_{31} of 81 mV/cm·Oe with an optimal thickness ratio t_{Meglas}/t_{BTO} of 1.0 [43]. Yongpin Wan *et al.* reported larger magnetic permeability, permittivity, and stiffer Young's modulus of the magnetostrictive

material individually contribute to higher coefficients α_{31} and α_{33} of a circular magnetoelectric energy harvester made Terfenol-D and PZT as they are shown in Figure 38 [44].

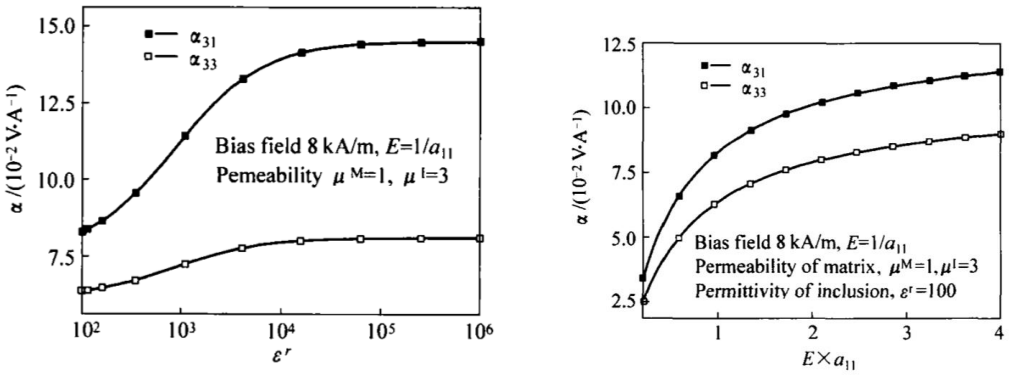

Figure 38. The left subplot shows the ME voltage coefficients α increase when the relative permittivity ε_r is increased; the right subplot shows the ME voltage coefficients increase when Young's modulus E is increased.

4.2 MODELING THE SINGLE RECTANGLE NI-BASED MAGNETOELECTRIC (ME) ENERGY HARVESTER

In addition to our previous work on modeling piezoelectric materials [14] and designing various broadband composite piezoelectric energy harvester devices [3], our current work has been modeling, simulating a ME composite magnetoelectric energy harvester device through COMSOL Multiphysics finite element simulation. A single rectangle Ni-based ME model is shown in Figure 39.

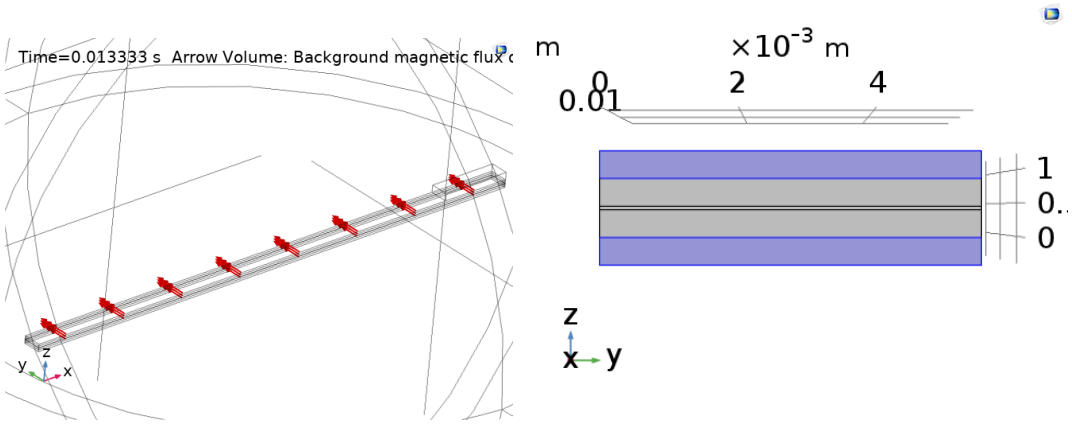

Figure 39. A composite magnetoelectric (ME) energy harvesting device based on Ni-PZT-PZN-Brass-PZT-PZN-Ni magnetoelectric composite material. The left plot (i) shows that a strong uniform dc saturation magnetic field is applied to the energy harvester in the transverse direction. The right plot (ii) shows the cross-section of the same five-layer structure: the purple layers are the magnetostrictive Ni layers and the grey layers (in between purple layers) are the piezoelectric layers. The thin layer (0.025mm) in the middle of two grey PZT-PZN Scheme4 layers is the brass layer.

The reason for a magnetoelectric energy harvester scavenging the magnetic energy in the environment is that the magnetic field causes stress in the magnetoelectric material (Ni, purple) that gets turned into an electric voltage by a bonded piezoelectric layer (gray) as shown in the right subplot in Figure 39. The red arrows show the transverse direction of the magnetic field penetrates through the composite magnetoelectric beam model. The negative magnetoelectric material (Ni, purple) layers shrink along the direction of the magnetic field as the stress is transferred from the magnetostrictive layers to the piezoelectric layers. The Ni layer contracts because of the Ni atom's two unpaired electrons in the 3d orbital. The electron configuration of

`

the Ni atom is [Ar] $3d^8 4s^2$ which is shown below. The arrow indicates the spinning direction of each electron's orbital:

[Ar]	3d ↑↓	3d ↑↓	3d ↑↓	3d ↑	3d ↑	4s ↑↓

Ni plate is made of fine Ni polycrystal material. Each Ni crystal domain is a single metallic crystal. The Ni atom forms Ni^{2+} cation in the crystal structure. Each Ni^{2+} cation loses two free electrons from its valent shell. The free electron enables the electric current flow; therefore, the Ni metal's electric conductivity is considerable. Despite the two free electrons on the 4s orbital have no contribution to the net Ni atom's magnetic moment as they spin in the opposite direction, they generate opposite electrical current, therefore the magnetic moments of the two free electrons in 4s orbital were canceled. Yet, the spins of two unpaired electrons in the 3d orbital exhibit the magnetic dipole moments. The area where the direction of Ni atom's magnetic moment aligns in the same direction forms a single magnetic domain in the Ni crystal. When the external magnetic field applied on the polycrystal Ni plate, the magnetic field applies a magnetic torque onto the Ni's atom's magnetic moment, therefore the Ni atoms magnetic moment will move and rotate toward the direction of the external magnetic field. The magnetic domain is defined as there is only one magnetization direction for every single magnetic domain. The bulk of the polycrystalline metallic Ni is made of many single magnetic domains shown in Figure 40

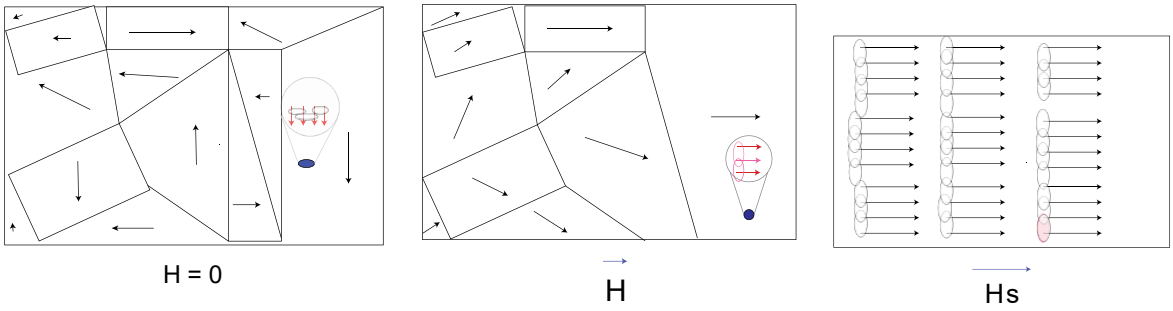

Figure 40. The magnetic domain in the Ni's polycrystalline material with no external magnetic field on the left subplot; with a weak external magnetic field H on the middle subplot; with the saturated external magnetic field H_s on the right subplot. The red arrow is a Ni atom's magnetic moment. The ellipses are the exchange interaction between Ni cations' unpaired electrons on the 3d orbital. H_s is the saturation magnetic field.

The reason the atomic magnetization direction tends to align with the adjacent atom(s) in the ferromagnetic material is minimizing exchange energy E_{ex} between the electrons of the adjacent atoms expressed in equation (52):

$$E_{ex}(\theta) = -2A\sigma^2 \cos\theta \qquad (52)$$

σ is the angular momentum of the electron's spin in 3d orbital; A is the exchange constant and $A > 0$ for ferromagnetic atoms; θ is the angle of the spins of two adjacent Ni atom on 3d orbital. We can see that when $\theta = 0$ (or $\cos\theta = 1$), the exchange energy E_{ex} reaches a minimum at $-2A\sigma^2$. Therefore, the magnetization direction of the Ni atom tends to align with those of the adjacent Ni atoms in a single magnetic domain, as they are shown by the red arrow in Figure 40. Such interaction between atoms as also known as the exchange interaction shown

by ellipses in Figure 40. As the external magnetic field increased from 0 to the saturated magnetic field H_s, the magnetic domain walls disappear and the whole bulk Ni material gradually becomes a single magnetic domain, the magnetostrictive material generates maximum strain in the saturated external magnetic field. The stress is being transferred into the piezoelectric material from the magnetostrictive maternal such as Ni, which generates more electricity. Such a coupled effect is referred to as the magnetoelectric effect. The magnetoelectric effect is commonly expressed as the coupling equation (53) [22] and Figure 41 [33] in the literature:

$$\text{ME effect} = \frac{magnetic}{mechanical} \times \frac{mechanical}{electric} \tag{53}$$

(magnetostriction) (piezoelectricity)

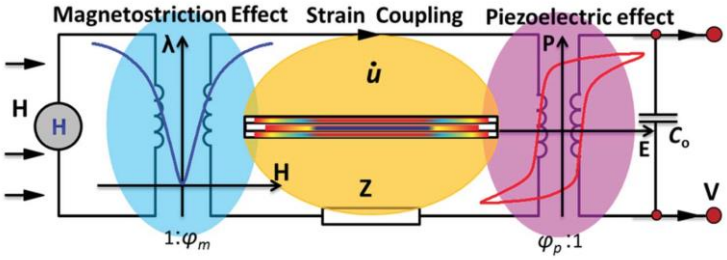

Figure 41. A generalized equivalent circuit modeling the coupling of the piezoelectric effect and the magnetostrictive effect [33]. H is the magnetic field. φ_m is the magneto-elastic coupling factor. φ_p is the piezoelectric coupling factor. Z is the impedance. C_o is the clamped capacitance of the piezoelectric bimorph. E is the electric field. λ is the magetostriction. $\dot{u}$ is

the mechanical current. P is the electric polarization. V is the output voltage.

Equation (53) entails that the ME effect is a combined effect of the piezoelectric and the magnetostrictive effects by the mechanical interaction. The mechanical properties, the electrical properties, and the magnetic properties are expressed in the form of two constitutive equations (54), (55) and (56) in the stress-charge-magnetic field relation in the literature [21].

$$\vec{\sigma} = \mathbf{c}\,\vec{S} + \mathbf{e}^{\mathbf{T}}\vec{\mathrm{E}} + \mathbf{q}^{\mathbf{T}}\vec{\mathrm{H}} \quad (54)$$

$$\vec{\mathrm{D}} = \mathbf{e}\,\vec{S} + \boldsymbol{\varepsilon}\vec{\mathrm{E}} + \boldsymbol{\alpha}\vec{\mathrm{H}} \quad (55)$$

$$\vec{\mathrm{B}} = \mathbf{q}\,\vec{S} + \boldsymbol{\alpha}^{\mathbf{T}}\vec{\mathrm{E}} + \boldsymbol{\mu}\vec{\mathrm{H}} \quad (56)$$

$\vec{\sigma}$ is the stress vector (6×1); **c** is the stiffness tensor (6×6) of 4th order; $\vec{S}$ is the strain vector (6×1); $\mathbf{e}^{T}$ is the third order piezoelectric coupling tensor (3×6) transposed; $\vec{\mathrm{E}}$ is the electric field (3×1); $\mathbf{q}^{T}$ is the third order piezo-magnetic tensor (3×6) transposed; $\vec{\mathrm{H}}$ is the magnetic field vector (3×1); $\vec{\mathrm{D}}$ is the electric charge displacement vector (3×1); **ε** is the second-order dielectric tensor (3×3); **α** is the second-order magnetoelectric (ME) tensor (3×3); **μ** is the second-order permeability tensor (3×3). These constitutive equations (54) and (55) are similar to the constitutive equations (1) and (2) except for an additional magnetic field terms H in each constitutive in equations (54) and (55) and (56). The stiffness matrix **c** can be calculated by a step-by-step conversion scheme from the piezoelectric material and the mechanical material properties to the

`

stiffness matrix and the coupling matrix [14]. The piezo-magnetic tensor **q** of nickel is shown in the matrix form below [45].

$$\begin{bmatrix} -4140 & 570 & 0 & 0 & 0 & 0 \\ 0 & 0 & 0 & 0 & 0 & 0 \\ 0 & 0 & 0 & 0 & 0 & 0 \end{bmatrix} 10^{-12} \text{ A/m} \tag{57}$$

The composite magnetoelectric energy harvesting device is a five-layer bimorph structure as shown in Figure 39. The upper purple layer and the lower purple layer are kept the same thickness of 0.3 mm. The grey layers are made of the metallic Ni, which is a magnetostrictive material. The upper gray layer and lower gray layer are made of the PZT-PZN Scheme4 material, which was mentioned in our previous papers: 0.2676 mW/cm^3 predicted and 0.1713 mW/cm^3 measured as reported by Bedekar *et al.* about its superior power density compared with other PZT materials [3] [14] [15]. The thin layer brass in the middle is 0.025 mm thick. The composite magnetoelectric energy harvesting device will be exposed to two kinds of magnetic fields in the transverse direction from two sources: a strong bias dc saturation magnetic field from an electric magnetic coil and an alternating weak ac magnetic field B_{ac} at the amplitude of +/- 1 Oe that oscillates at 1 kHz shown in Figure 42, which is generated horizontally by a pair of Helmholtz coils. The dc bias magnetic field is needed to generate the maximum magnetostrictive effect on the device, which changes its shape in the direction of the strong dc magnetic field. The weak ac uniform sinusoidal magnetic field oscillates at 1 kHz for the measurement purpose shown in the subplot of Figure 42. The proportioned magnetic field in the time domain is shown in the right subplot of Figure 42.

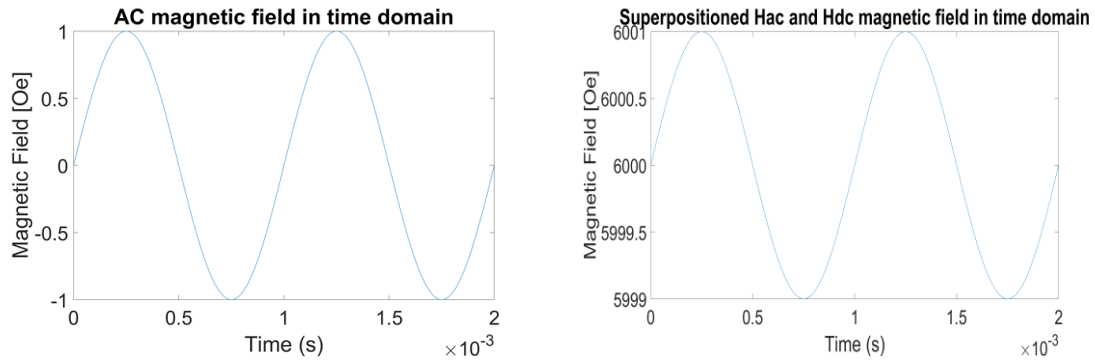

Figure 42. An alternating ac magnetic field oscillates of the amplitude of 1 Oe at 1 kHz in a total of two periods on the left subplot; the superpositioned magnetic field comes from the alternating ac magnetic field and the dc bias magnetic field of the magnitude of 6000 Oe or 0.6 Tesla in two mechanical vibration cycles is plotted on the right subplot.

4.2.1 Method

The first step is to find the mechanical resonance frequencies of the ME VEH through frequency analysis. This is performed through COMSOL Multiphysics simulation as the eigenfrequency study converges in a just a few minutes, as Figure 43 shows the first mode shape deformation of a rectangular magnetoelectric (ME) VEH, with 60 mm in length, 2 mm in width, 0.825 mm in thickness, and a 0.4 gram of a steel tip mass. The dimension of the bimorph was chosen based on the pattern on our results of the single rectangle piezoelectric beam's electric power in Chapter 3 Section 3.2.2: the large electric output power appears the longest and the least in width and thickness. The tip mass has the same width of 2 mm as the rectangular beam, 7.7 mm in length, and 0.2 mm in thickness. The tip mass is made of the high-strength alloy steel, which is one of the built-in metallic materials in COMSOL. The

material property of the steel is listed in Appendix A. We chose Ni to be our choice for the magnetostrictive layers in Figure 44. The first eigenfrequency 143.6 Hz of a rectangular magnetoelectric beam with a metal tip mass shown in Figure 43. With the tip mass, the first eigenfrequency is 143.6 Hz shown in Figure 44. We added one tip mass to our model because adding tip mass reduces the eigenfrequency of the ME VEH from 169.36 Hz to 143.6 Hz by 25.76 Hz, 15.2 % reduction.

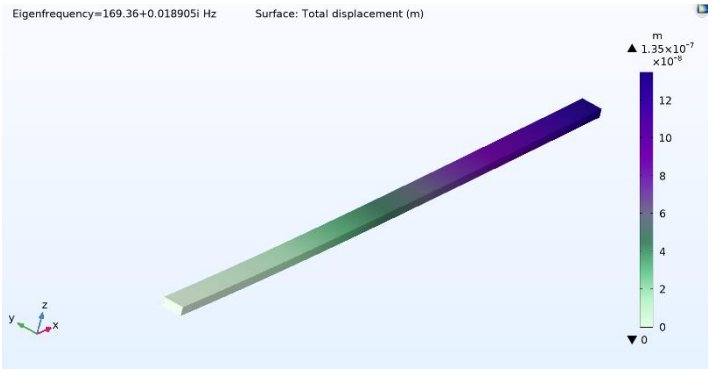

Figure 43. The first eigenfrequency 169.36 Hz of a rectangular magnetoelectric beam without a tip mass on its free-end; the structural quality factor of the beam is 4479.3.

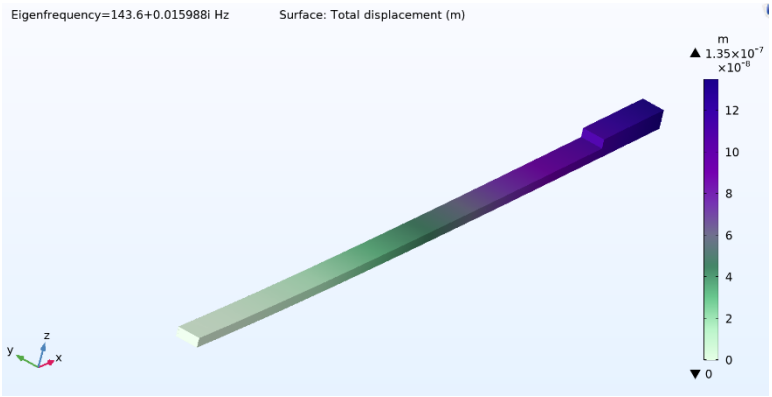

Figure 44. The first eigenfrequency 143.6 Hz of a rectangular magnetoelectric beam with a

metal tip mass; the structural quality factor of the beam is 4490.7.

To investigate the behavior and the performance of the magnetoelectric beam, initially, we ran the time-dependent study from 0 s to $2/f_r$ s with a 1/1200 s interval as the COMSOL Multiphysics software does not allow us to run a frequency study with two oscillating sources (vibration and ac magnetic field) directly. Therefore, running the time-dependent study overcomes this problem. However, the time-dependent studies are known to have convergence issues in COMSOL. As the simulation time is a finite resource, therefore, the ending time is set to $2/f_r$ s for the time-dependent simulation, f_r is the resonance frequency. If the time-dependent simulation encountered non-convergence issue, we followed the instructions from COMSOL support's advice and COMSOL's official article about fine-tuning solver settings [46]. By setting up the time-dependent study in such a way based on the article "Improving convergence in nonlinear time-depended model", we finally obtained the time-dependent data. We set the vibration amplitude of the free end of the beam to 2 mm along the z-axis in the function of time expressed by $A(t) = -2\cos(2\pi f t)$, and f is the first resonance at 143.6 Hz shown in Figure 45.

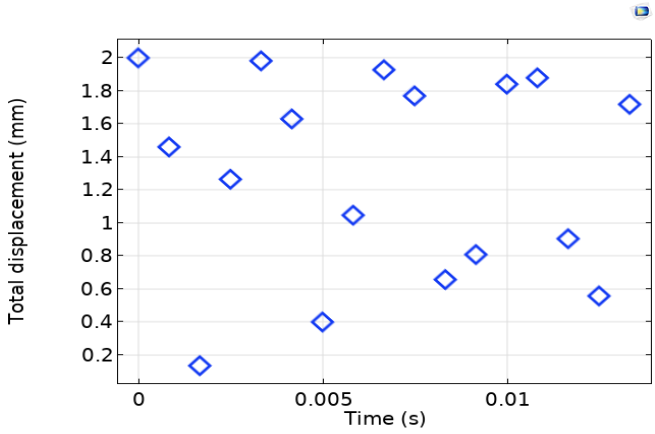

Figure 45. The displacement boundary condition on the free end of the same ME beam with the same steel tip mass.

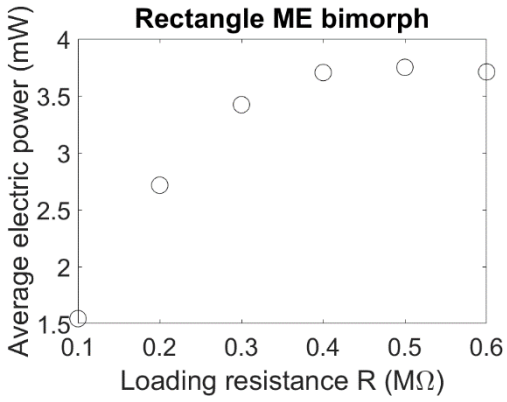

Figure 46. Impedance matching of the same ME rectangular beam with a 0.4g tip mass. The optimal impedance is 0.5 MΩ.

After the first step of eigen frequency, the second step is the impedance matching: when the external impedance matches the internal impedance, the system's electric output reaches the maximum. As we can see from Figure 46, the optimal external resistance was 0.5 MΩ through

`

scanning the multiple resistance from 0.1 MΩ to 0.6 MΩ with steps of 0.1 MΩ. We then call the matching resistance “optional resistance” because the system’s electric output power reaches the maximum at that matched impedance at 0.5 MΩ. The loading impedance is connected in between two surfaces as shown in Figure 47.

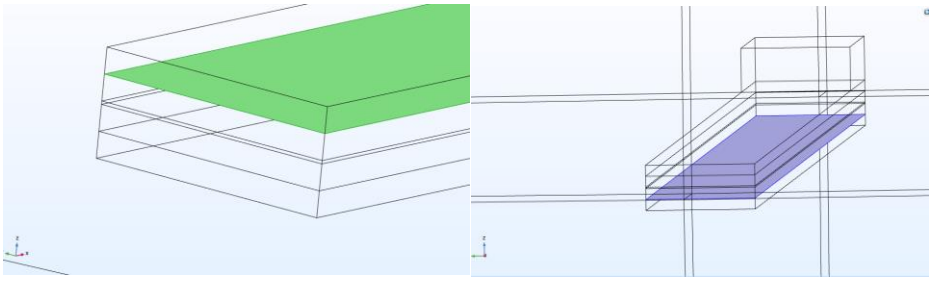

Figure 47. The green surface shown on the left subplot represents one of the electrodes connecting to the electrical ground; the purple surface shown on the right subplot represents the other electrode connecting to a loading resistor in an electric circuit.

Once the position of the electrode is determined, we then went to the next step to optimize the electric power output by the electric impedance matching. We ran the time-dependent study from 0 s to $2/f_r$ s with 1/1200 s interval. The value f_r is the fundamental mechanical vibration frequency at 143.6 Hz. We kept the same mechanical vibration frequency at 143.6 Hz, and we ran the time-dependent simulation for two models in one mechanical vibration cycle from 0 s to 2/143.6 s for the voltage comparisons. The optimal resistor is 0.5 MΩ for the simulation model with the design of the traditional electrode. In Figure 48, it can be seen that the peak-to-peak voltage of the traditional ME bimorph is 139.24 V. The average rms voltage is 47.2 V.

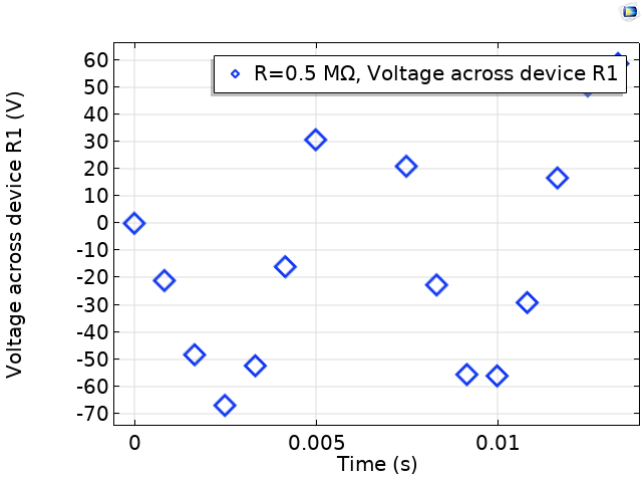

Figure 48. The voltage generated by the rectangular ME bimorph connected with the optimal resistor of 0.5 MΩ .

In Figure 49, the peak electric power of the traditional ME bimorph is 9.25 mW in two mechanical cycle from 0 s to 2/143.6 s. The average electric power of the traditional ME bimorph is 3.69 mW in two mechanical cycle from 0 s to 2/143.6 s.

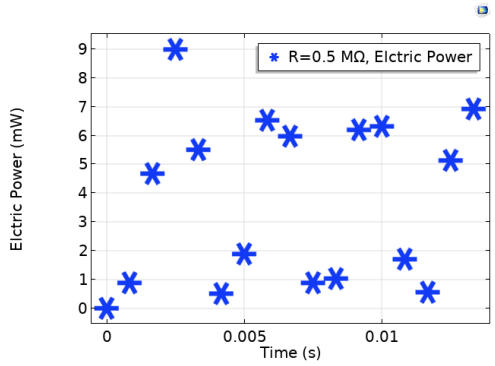

Figure 49. The electric power dissipated on the optimal external resistor of 0.5 MΩ of the traditional single rectangle bimorph design in two mechanical vibration cycles s at 143.6 Hz.

In Figure 50, it can be seen that the peak electric power density of the traditional ME bimorph is 192 mW/cm^3. The average electric power density of the traditional ME bimorph is 77.07 mW/cm^3.

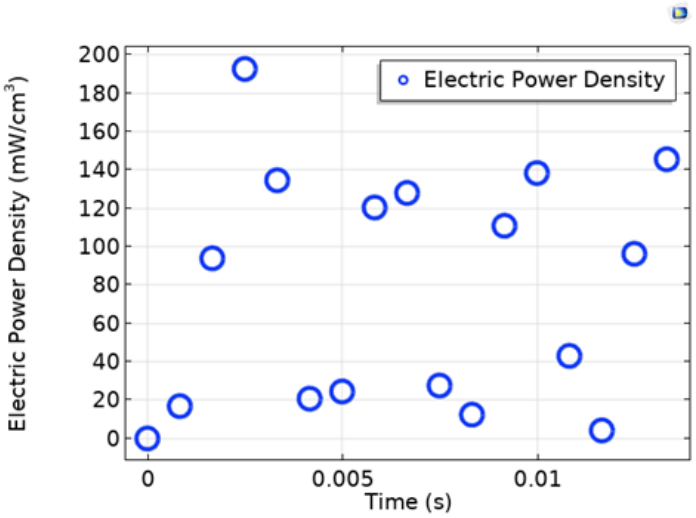

Figure 50. The electric power density dissipated on the external resistor at 0.5 MΩ of the traditional single rectangle bimorph design in two mechanical vibration cycles at 143.6 Hz.

In Figure 51, the peak magnetoelectric coefficient of the traditional ME bimorph is 1862.2 V/cm·Oe. The average rms magnetoelectric coefficient of the traditional ME bimorph is 1179.9 V/cm·Oe.

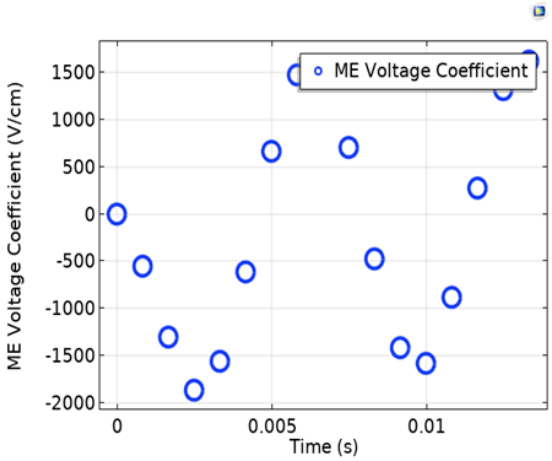

Figure 51. The magnetoelectric voltage coefficient between the rectangular ME bimorph.

4.2.2 Summary

We listed the first resonance frequency of the mechanical vibration, the optimal resistance, the maximum electric power, and the maximum electric power density in Table 7.

Table 7 Single rectangle Ni-based ME bimorphs in the first mechanical vibration cycle

ME bimorph	*1st eigenfrequency Hz*	*Optimal Resistance*	*Max. Electric Power*	*Max. Electric Power Density*
Single rectangle	143.6	0.5 MΩ	9.25 mW	192 mW/cm^3

`

The ratio of the first resonance frequency and the quality factor is the electric power bandwidth of the energy harvester. As we can see in Table 8, the ratio of the fundamental frequency and the quality factor f_r/Q is at 0.0319 (Hz), therefore the theoretical electric power bandwidth is narrow. The maximum electric power and the electric power density is low. For these reasons, we are motivated to design a more advanced ME beam with improved electric power, electric power density, and electric power bandwidth.

Table 8 Single rectangle Ni-based ME bimorphs in two mechanical vibration cycles

ME bimorph	f_r/Q ratio	Average voltage (V)	Max. Displacement of the free end of (mm)	Quality factor	Average α (V/cm·Oe)
Single rectangle	0.0319	43.3	2	4490.7	1179.9

`

4.3 MODELING OF THE ONE-PIECE TRAPEZOIDAL MAGNETOELECTRIC ENERGY HARVESTER

4.3.1 Motivation

Because the quality factor Q of the single rectangle Ni-based ME bimorph is very high at 4490.7. The ratio of the fundamental frequency f_r and the quality factor Q is as low as 0.0319. The quality factor Q can be defined as the ratio between the stored energy E_{stored} and the lost energy in a cycle E_{lost}, Q = $2\pi \frac{E_{stored}}{E_{lost}}$ [47]. A high quality factor Q system indicates the system has a low mechanical loss. Therefore, the electric power output bandwidth will be very narrow, as the mechanical vibration bandwidth is expressed $\Delta \mathrm{f} = \frac{f_r}{Q}$. For these reasons, we are motivated to design a one-piece trapezoidal Ni-based ME energy harvester since the authors cannot find any similar simulation research in the literature about the trapezoidal ME energy harvesters to date.

4.3.2 Method

The investigation method to reveal the character of the electric power density bandwidth of the one-piece trapezoidal beam design is similar to the method in Chapter 4 Section 3. In this work, we designed a one-piece trapezoidal ME bimorph with one shorter width W_1 at 8 mm and the longer width W_2 at 40 mm, the length L at 60 mm, and the thickness at 1.05 mm. Two

views of the one-piece ME composite bimorph design are shown in Figure 52, Figure 53, and Figure 54.

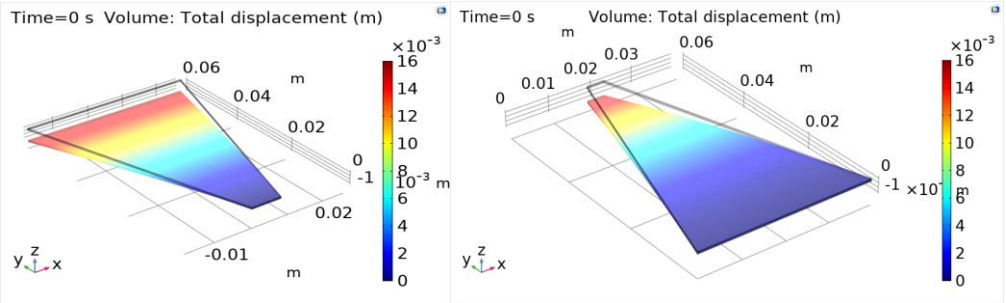

Figure 52. The initial condition of the displacement when time t starts from 0 s. The left subplot is the first design: W_1 is 8 mm and W_2 is 40 mm. The right subplot is the second design: the shorter width W_1 is 4 mm, the longer width W_2 is at 40 mm.

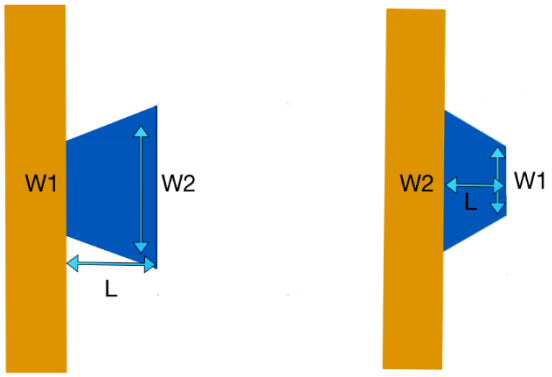

Figure 53. The top-down view of the one-piece trapezoidal ME bimorph. The left subplot is the first design, and the right subplot is the second design. W_1 is a shorter width and W_2 is the

longer width.

For the first design of the one-piece ME beam, the dimensions of W_1 and W_2 were set at 8 mm and 40 mm respectively as it showed the largest electric power density output at 3.01 mW/cm^3 without the magnetostrictive Ni layer with an optimal resistance at 0.06 MΩ. For the second design of the one-piece ME beam, the dimensions of W_1 and W_2 were set at 4 mm and 40 mm respectively as it showed the peak electric power density output at 2.36 mW/cm^3 without the magnetostrictive Ni layer with an optimal resistance at 0.06 MΩ. We kept the same optimal resistance of 0.06 MΩ because the dimension of the piezoelectric layers did not change in the ME design, therefore the optimal resistance remained the same; the only addition to the original one-piece trapezoidal model was the magnetostrictive layer(s) as the thickness view shown in Figure 54.

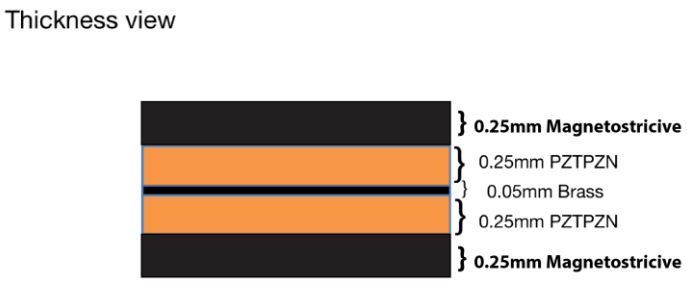

Figure 54. The thickness view of the composite trapezoidal ME bimorph's upper and lower magnetostrictive and PZT-PZN Scheme4 layers. A general nonconductive adhesive material

can be used to bound the Magnetostrictive Ni layer and the PZTPZN layer.

4.3.3 Results and Discussion

We ran the time-dependent studies from 0 s to $2/f_{r1}$ with the interval of 1/1200 s for the mechanical displacement at 2 mm at the free end of the bimorph. We plotted the voltage, the electric power output, the electric power density and ME voltage constant of two different one-piece trapezoidal ME bimorph designs. We assigned f_{r1} to be the first eigenfrequency of the structure. We plotted the displacement of the free end of two different one-piece trapezoidal ME bimorph designs in the initial two mechanical vibration cycle shown in Figure 55. We could have run more cycles in the time domain, as the signal is harmonically repeated; we can only run two vibration cycle. We can see that the amplitude of free end of each bimorph is capped at 2 mm.

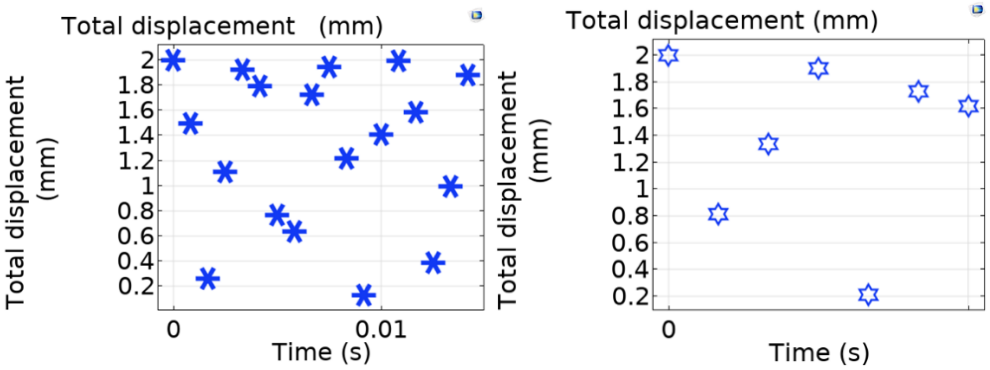

Figure 55. The left subplot is the mechanical displacement of the free end of the first bimorph design vibrating at its fundamental frequency of 137.52 Hz, and the right subplot is the mechanical displacement of the free end of the second bimorph design vibrating at 380.06 Hz.

`

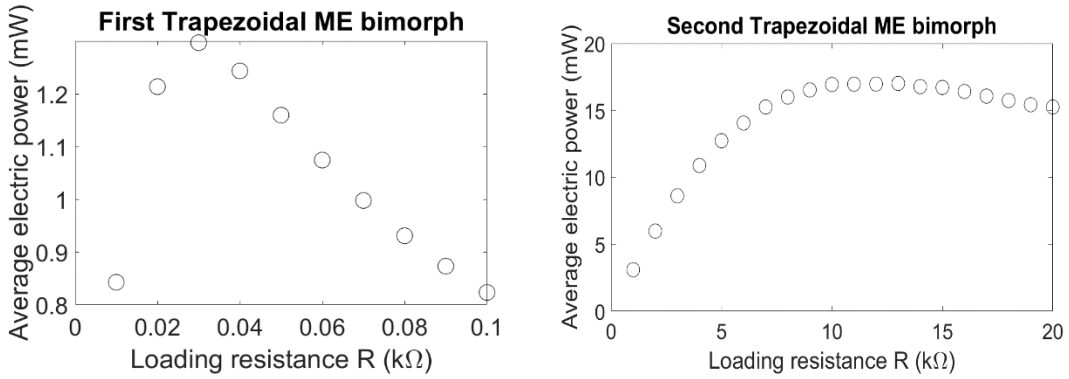

Figure 56. Impedance matching of the two trapezoidal ME bimorphs

The left subplot of Figure 56 the shows the optimal impedance of the first trapezial bimorph is 0.03 MΩ (30 kΩ) through scanning multiple external resistance from 0.01 MΩ to 0.1 MΩ with steps of 0.01 MΩ. The right subplot of Figure 56 the shows the optimal impedance of the second trapezial bimorph is 13 kΩ through scanning multiple external resistance from 1 kΩ to 20 kΩ with steps of 1 kΩ.

In Figure 57, we can see the peak-to-peak voltage V_{pp} of the first trapezoidal ME bimorph design is 18.11 V. The peak-to-peak voltage V_{pp} of the second trapezoidal ME bimorph design is 43.44 V. The average voltage V_{RMS} of the first one-piece trapezoidal ME bimorph in the initial two mechanical vibration cycles is 6.23 V. The average voltage V_{RMS} of the second one-piece trapezoidal ME bimorph in the initial two mechanical vibration cycles is 14.69 V. The average rms voltage of the second one-piece trapezoidal ME bimorph design is 2.35 times higher than that of the first one-piece trapezoidal ME bimorph design.

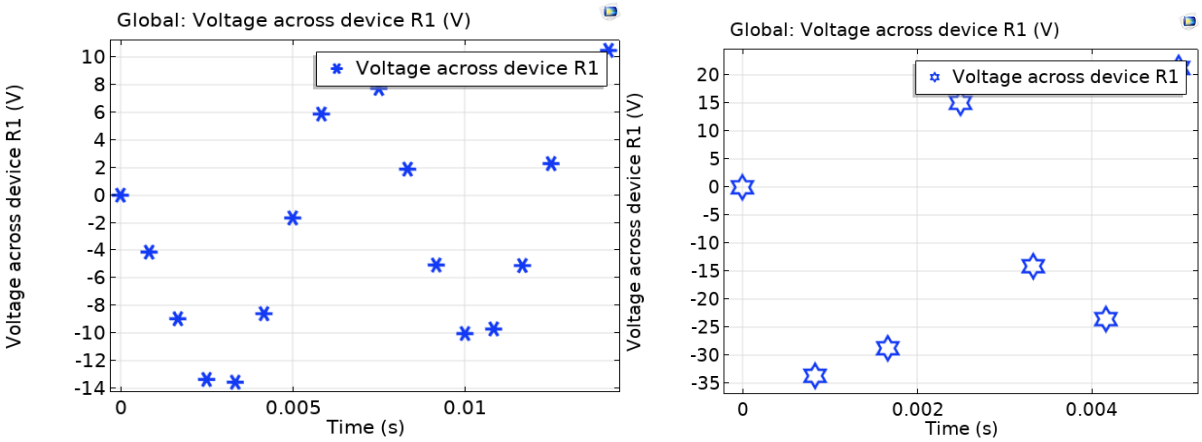

Figure 57. The voltage of two different design of the one-piece trapezoidal ME bimorphs in the first one mechanical vibration cycle; the left subplot is the voltage across the external resistance of the first bimorph design vibrating at its fundamental frequency 137.52 Hz with the optimal resistance at 0.03 MΩ (or 30 kΩ); the right subplot is the voltage across the external resistance of the second bimorph design vibrating its fundamental frequency 380.06 Hz with the optimal resistance at 0.013 MΩ (or 13 kΩ)

In Figure 58, we can see the peak electric power output of the first one-piece trapezoidal ME bimorph design is 3.09 mW. The peak electric power of the second one-piece trapezoidal ME bimorph design is 37.13 mW. The average electric power of the first one-piece trapezoidal ME bimorph in the initial two mechanical vibration cycles is 1.3 mW. The average electric power of the second one-piece trapezoidal ME bimorph in the initial two mechanical vibration cycles is 16.89 mW. The average electric power of the second one-piece trapezoidal ME bimorph design is 15.6 times higher than that of the first one-piece trapezoidal ME bimorph design.

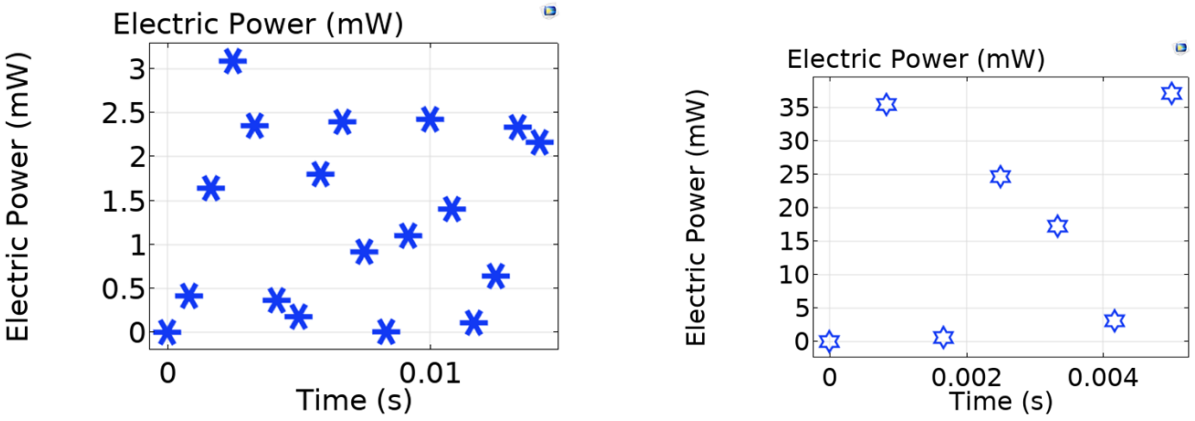

Figure 58. The electric power output of two one-piece trapezoidal ME bimorphs in the first one mechanical vibration cycle; the left subplot is the first bimorph design vibrating at its fundamental frequency 137.52 Hz with the optimal resistance at 0.03 MΩ (30kΩ); the right subplot is the second bimorph design vibrating at its fundamental frequency 380.06 Hz with the optimal resistance at 0.013 MΩ (or 13 kΩ).

In Figure 59, we can see the peak electric power density of the first one-piece trapezoidal ME bimorph design is 4.29 mW/cm^3. The peak electric power density of the second one-piece trapezoidal ME bimorph design is 56.26 mW/cm^3. The average electric power density of the first one-piece trapezoidal ME bimorph in the initial two mechanical vibration cycles is 1.8 mW/cm^3. The average electric power density of the second one-piece trapezoidal ME bimorph in the initial two mechanical vibration cycles is 25.59 mW/cm^3. The peak and average electric power density of the second one-piece trapezoidal ME bimorph design is around 14 times higher than that of the first one-piece trapezoidal ME bimorph design.

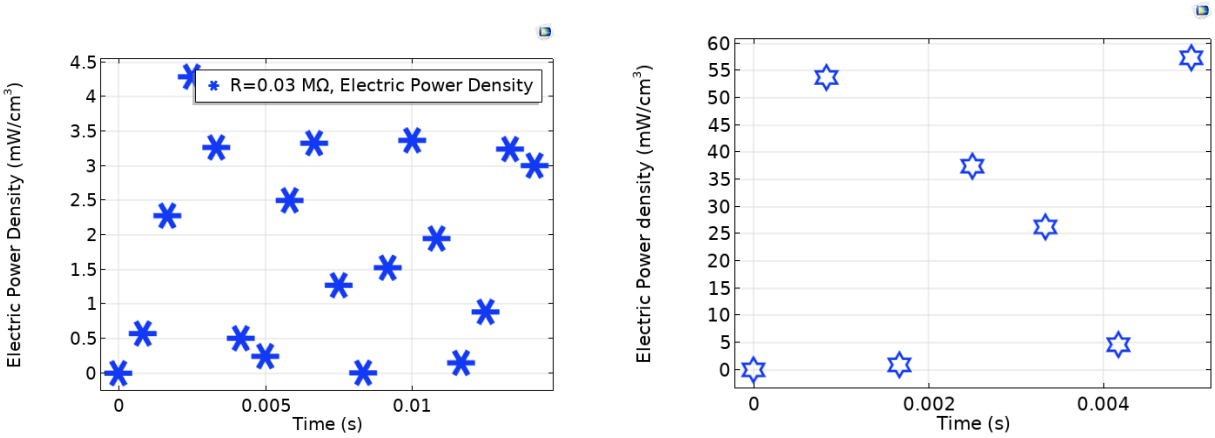

Figure 59. The electric power density (output) of two one-piece trapezoidal ME bimorphs; the left subplot is the first bimorph design vibrating at its fundamental frequency 137.52 Hz with the optimal resistance at 0.03 MΩ (30 kΩ); the right subplot is the second bimorph design vibrating at its fundamental frequency 380.06 Hz with the optimal resistance at 0.013 MΩ (or 13 kΩ).

In Figure 60, we can see the peak ME voltage coefficient α of the first one-piece trapezoidal ME bimorph design is 192 V/cm Oe. The peak ME voltage coefficient α of the second one-piece trapezoidal ME bimorph design is 429 V/cm Oe. The average ME voltage coefficient α of the first one-piece trapezoidal ME bimorph in the initial two mechanical vibration cycles is 124 V/cm Oe. The average ME voltage coefficient α of the second one-piece trapezoidal ME bimorph in the initial two mechanical vibration cycles is 294 V/cm Oe. The average ME voltage coefficient α of the first one-piece trapezoidal ME bimorph is 2.37 time higher than that of the second one.

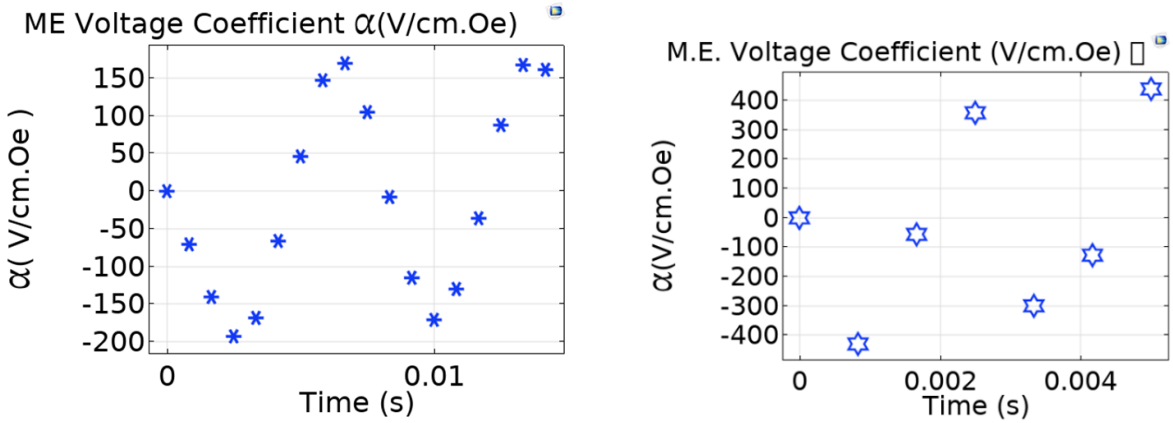

Figure 60. The ME voltage coefficient α in the first mechanical vibration cycle; The left subplot is the α of the first one-piece trapezoidal ME bimorph design in the time domain; the right subplot is the α of the second one-piece ME bimorph design in the time domain.

4.3.4 Summary

Once we found the first resonance vibration frequency of two different one-piece trapezoidal Ni-based ME bimorph design through the eigenfrequency analysis in COMSOL, we then listed the first resonance vibration frequencies, the structure quality factors, and the maximum electric power density in Table 9. As we can see, the eigenfrequency of the second ME one-piece trapezoidal bimorph design is 2.76 times higher than that of the first. The second ME one-piece trapezoidal bimorph has 12.9 times in average electric power and 14.2 times higher electric power density in average than that of the first. f_r/Q ratio of the first trapezoidal one-piece ME bimorph is 5.5 times higher than that of the rectangle ME bimorph. f_r/Q ratio of the second trapezoidal one-piece ME bimorph is 15.3 times higher than that of the rectangle ME bimorph. f_r/Q ratio of the second trapezoidal one-piece ME bimorph is 2.8 times higher than

that of the first trapezoidal one-piece ME bimorph. Yet the peak electric power density of the rectangle ME bimorph is the highest among three different ME bimorphs. Comparing two trapezoidal bimorphs, the second design not only has higher f_r/Q ratio (2.8x) but also higher electric power density (13x).

Table 9 Comparison of three different Ni-based ME bimorphs

`	*1st eigenfrequency (Hz)*	*Q (qualify factor)*	*f_r/Q Ratio*	*Max. Electric Power Density*
Rectangle bimorph	143.60	4490.7	0.0319	192 mW/cm^3
Our 1st trapezoidal ME bimorph	137.52	784.16	0.1754	4.29 mW/cm^3
Our 2nd trapezoidal ME bimorph	380.06	777.53	0.4888	56.26 mW/cm^3

The ratio of the first resonance frequency and the quality factor is proportional to the power bandwidth of the energy harvester. As we can see in Table 10, the ratio of the resonance frequency and the quality factor f_r/Q of the second one-piece trapezoidal ME bimorph design is 2.8 times higher than the first. Therefore, the theoretical bandwidth of the second one-piece trapezoidal ME bimorph has a 2.8 time higher than that of the first one. The theoretical bandwidth of the first one-piece trapezoidal ME bimorph has a 5.5 time higher than that of the rectangle ME bimorph. The theoretical bandwidth of the second one-piece trapezoidal ME

bimorph has a 15.3 time higher than that of the rectangle ME bimorph. Overall, the second one-piece trapezoidal ME bimorph has better electric power (2.8x), and electric power density (13.1x).

Table 10 Comparison of three different ME one-piece trapezoidal bimorphs

One-piece ME bimorph	*f_r/Q Ratio*	*RMS Voltage(V)*	*Displacement (mm)*	*Average α (V/cm·Oe)*	*Optimal resistance (MΩ)*
Rectangle bimorph	0.0319	47.2	2	1179	0.5
1st trapezoid	0.175	6.23	2	124	0.03
2nd trapezoid	0.488	14.69	2	294	0.013

4.4 VALIDATION THROUGH COMPARISON

In the field of developing new ME energy harvesters, there are a few experimental [12] [48] and theoretical works [12] [49] [48] in the literature. However, there is very few simulations work about ME VEH in the literature due to the inherent difficulty and complexity in modeling the ME effect. In this work, we provide the simulation results of the single rectangle ME VEH and the one-piece ME VEH through comparing our results with other researchers' results. We

have been realizing there are many kinds of novel ME energy harvesters in the literature, but most of them fall into two general categories: torque mode and force mode as they are shown in Figure 61.

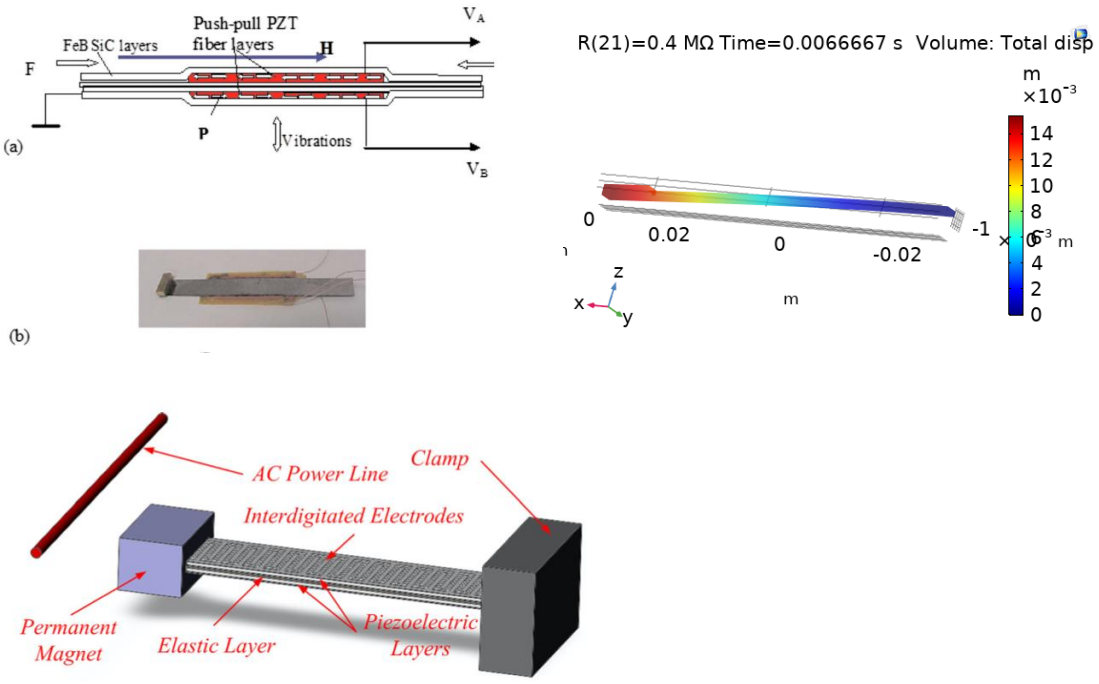

Figure 61. The lower left subplot shows a three-layer bimorph operating in a torque mode [48]; the right subplot shows our five-layer rectangle composite bimorph operating in a force mode; the upper left and middle left subplot shows a three-layer bimorph operating in a force mode.

The torque mode magnetoelectric energy harvester usually has a low resonance and a permanent magnetic proof mass attached to the free end of the structure, which is shown in the left subplot of Figure 61. The permanent magnets on the free end have two purposes: one is lowering the resonance of the structure; the other is generating magnetic force align with the

external AC magnetic field H_{ac} which typically comes from electronics or electrical power. Han *et al.* reported they obtained 2.136 mW electric power and 3.65 mW/cm^3 electric power density by placing an AC power line at 1 cm distance away from the beam at the alternating frequency of 50 Hz, 10 Ampere electrical current [48]. Compared with the electric power of our revised single rectangle bimorph on the right subplot of Figure 61, with a 1 Oe alternating magnetic field H_{ac} and a 0.6 T constant H_{dc}, the average electric power is 3.74 mW and the average electric power density is 77.34 mW/cm^3. The resonance frequency is tuned to 50 Hz in Han's model. The resonance frequency of our single rectangular ME model is 143.6 Hz. The difference between the two models is tabulated in Table 11. In Figure 62 we showed the voltage data comparison between our revised ME rectangle bimorph with experiment data of Dong *et al.* [50].

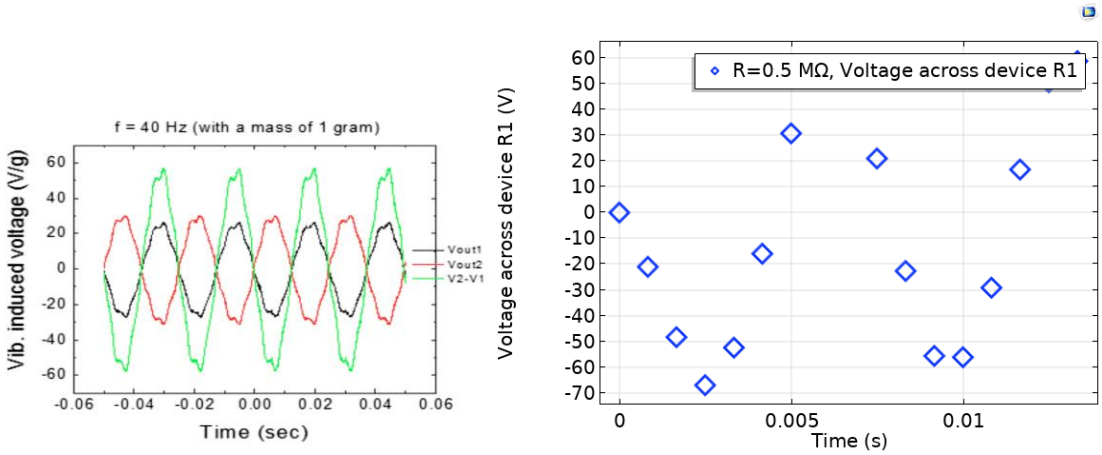

Figure 62. voltage result in the time domain from Dong *et al.* [50].

`

Table 11. Performance comparison between a torque mode ME bimorph and a force mode bimorph

Performance	Han *et al.* (torque mode)	Our rectangular model (force mode)	Dong *et al.* (force mode)
Electric power (mW)	2.136	3.74 (avg.)	0.42
Electric power density (mW/cm^3)	3.65	77.34 (avg.)	2.1
Piezoelectric volume (mm^3)	585.2	48	N/A
Optimal resistance	0.9 GΩ	0.5 MΩ	50 kΩ
Resonance frequency (Hz)	50	143.6	40
Displacement of the free end (mm)	11.66	2	N/A
Peak Magnetoelectric voltage coefficient (V/cm·Oe)	N/A	1657	N/A
Piezoelectric material	PZT-5A	PZTPZN-Scheme4	PZT fiber
Magnetostrictive material	NdFeB N38	Ni	NdFeB
Mass of tip (g)	30.5	0.4	1
Number of composite layers	3	5	5
Peak Voltage	N/A	67.05	63

`

Although there are not as many publications about the trapezoidal ME harvesters as the rectangle ME harvesters in the literature, we still managed to find one in the literature from Annapureddy et al. shown in Figure 63 [51]. In Annapureddy et. al. experimental work, three different one-piece trapezoidal bimorphs with the ratio b/a: the shorter edge "b" on the free end and the longer edge "a" on the fixed end of beam at 0.68, 0.45 and 0.22 shown in the left subplot of Figure 63 were designed. The authors found that the one-piece trapezoidal bimorph with the lowest b/a ratio of 0.22 has the highest voltage at 10.9 V as shown in Figure 64 [51]. The authors claimed that the electric power density increased 6.8 times with the optimal resistor at 0.4 MΩ compared to a conventional rectangular ME energy harvester due to the non-uniform strain distribution as shown in the right subplot in Figure 63. The in-plane strain increased 37%, 49%, and 62% for the single one-piece trapezoidal ME bimorph with the b/a ratio of 0.68, 0.45 and 0.22 compared to the conventional rectangle ME bimorph at the b/a ratio at 1.0 [51]. They also reported that the strain on the free end is 26% higher than the fixed end [51]. Annapureddy *et al.* reported the voltage output increases linearly with the external alternating magnetic field H_{ac} [51]. Therefore, they predicted the electric power increases quadratically with respect to H_{ac} increase based on the expression of the electric power $P = U^2/R$ [51]. These one-piece trapezoidal bimorphs have the same first resonance frequency at 40 Hz and operate in an alternating magnetic field H_{ac} of 200 μT (2 Oe) without the bias DC magnetic field H_{dc} [51]. We compared our one-piece trapezoidal ME bimorphs results with theirs in Table 12.

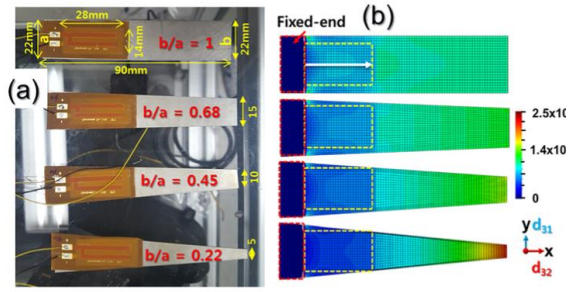

Figure 63. The 2D dimension of another one-piece trapezoidal ME energy harvester by Annapureddy *et al.* [51].

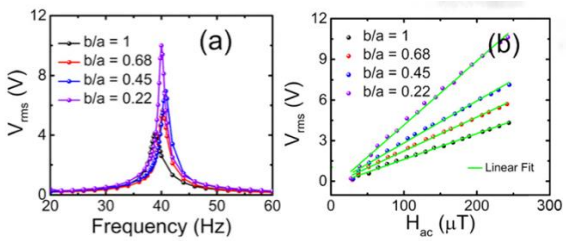

Figure 64. (a) Average voltage around the bimorph's resonance at 40 Hz; (b) Average voltage increases linearly when the alternating magnetic field increases;

Table 12. Comparison between three different one-piece trapezoidal ME bimorphs

Performance	Annapureddy *et al.*	Our one-piece ME trapezoidal (first design)	Our one-piece ME trapezoidal (second design)
Peak electric power density (mW/cm^3)	0.108	4.29	56.26
Piezoelectric volume (cm^3)	0.00392	0.72	0.66
Optimal resistance (MΩ)	0.4	0.03	0.013
Resonance frequency (Hz)	40	137.52	380.06
Displacement of the free end (mm)	N/A	2	2
Average rms Magnetoelectric voltage coefficient (V/cm·Oe)	N/A	124	294
Piezoelectric material	PMN-PZT-Mn (Single crystal sheets)	PZTPZN-Scheme4 (Polycrystal)	PZTPZN-Scheme4 (Polycrystal)
Magnetostrictive material	Ni (magnetized)	Ni	Ni
Mass of tip (g)	4.5 (Nd magnet)	0	0
Number of composite layers	4	5	5
RMS average voltage (V)	10.9	6.23	14.69
Amplitude of H_{ac} (Oe)	2	1	1

`

CHAPTER 5: MILESTONES

The candidate passed the qualifying exam on October 15, 2014 and presented his proposal defense in September 2017. He attended the COMSOL Boston conference and presented our work on the topic of "Modeling, Simulation and Optimization of Piezoelectric Bimorph Transducer for Vibration Energy Harvesting" in 2016, 2017, and 2018 with three presentation posters. The candidate also made an external user presentation in 2016 with the topic of "Modeling, Simulation, and Optimization of Piezoelectric Bimorph For Broadband Energy Harvesting". The trips were funded by the Computational Science Program and the Department of Engineering Technology at MTSU. Three accepted manuscripts are published in the *Journal of Material Science Research* (Google-based Impact Factor 2017: 5.94), and the *Journal of Advances in Materials Science and Engineering* in Jan. 2019 (Impact Factor: 1.399), the authors, title, and journal's information are listed below:

N. Chen and V. Bedekar, "Modeling, Simulation and Optimization of Piezoelectric Bimorph Transducer for Broadband Vibration Energy Harvesting," *Journal of Material Science Research*, vol.6, no. 4, Oct. 2017

N. Chen and V. Bedekar, "Modeling, Simulation, and Optimization of Piezoelectric Bimorph Transducer for Broadband Vibration Energy Harvesting in multi-beam and trapezoidal approach", *Journal of Material Science Research*, accepted on Sep. 10, 2017.

`

N. Chen and V. Bedekar, “Design, modeling, simulation, and optimization of broadband two-piece trapezoidal piezoelectric devices for sensing and energy harvesting", *Journal of Advances in Materials Science and Engineering* in Jan. 2020

The candidate worked with the academic advisor Dr. Vishwas Bedekar (PI) on an external grant (NSF SCC) titled “Self-sustainable smart and connected communities” in Spring 2019. We are planning to submit one last manuscript to *IEEE UFFC* (or another peer-viewed journal) on our magnetoelectric energy harvesters in 2020.

`

CHAPTER 6: CONCLUSION AND FUTURE WORK

The research objectives mentioned in Chapter 2 were accomplished by showing the step by step model building process for piezoelectric electric bimorphs. We showed the electric power, electric power density and bandwidth of our piezoelectric multibeam and the one-piece and two-piece trapezoidal designs. The power bandwidth of our multibeam is wider than these of the trapezoidal bimorph designs. The power density of the trapezoidal bimorphs are higher than that of the multibeam design.

The remaining of the objectives proposed in Chapter 2 were also accomplished by building ME energy harvesting models in the background magnetic field. The voltage, the electric power and the electric power density are boosted comparing to the trapezoidal bimorphs due to the increased stress by the magnetoelectric effect between the piezoelectric layer and magnetostrictive layer. We compared our simulation results of the revised rectangle ME bimorph with the experimental results of Dong *et al.* and Han *et al*. in Chapter 4 Section 4. We also compared our simulation results of the one-piece ME bimorphs with the experimental results of Annapureddy *et al*. in Chapter 4 Section 4. We also compared our simulation results of the revised rectangle ME bimorph with our one-piece trapezoidal ME bimorphs shown in Table 13.

`

Table 13. Comparison between our ME bimorphs

Performance	Our rectangle ME	Our one-piece ME trapezoidal (first design)	Our one-piece ME trapezoidal (second design)
Avg. electric power (mW)	3.74	1.30	16.89
Avg. electric power density (mW/cm^3)	77.34	1.80	25.59
Piezoelectric volume (cm^3)	0.048	0.72	0.66
Optimal resistance (MΩ)	0.5	0.03	0.013
Resonance frequency (Hz)	143.6	137.52	380.06
Displacement of the free end (mm)	2	2	2
Avg. Magnetoelectric voltage coefficient (V/cm·Oe)	1179	124	294
Mass of tip (g)	0.4	0	0
Number of composite layers	5	5	5
Peak-to-peak Voltage (V_{pp})	139.24	14.69	43.44
The amplitude of H_{ac} (Oe)	1	1	1
Bias H_{dc} magnetic field (T)	0.6	0.6	0.6

`

Despite the time-dependent studies widely known for the non-convergence, our time-dependent COMSOL simulation model converges when the ending time is small, from a few mechanical vibration cycles to 0.1 s or 0.2 s. When the time-dependent simulation's duration of the ME models reached 1 second, the ME models did not converge. The reason for the non-convergence issue on the extended time-dependent ME models is to be investigated in the future. Nevertheless, COMSOL Multiphysics does not guarantee the convergence of all models after all. As long as the non-convergence issue for longer duration can be fixed in the future, can we easily convert the time-dependent data to the frequency bandwidth data using the method mentioned in Chapter 4 Section 4.3. Only then the electric power bandwidth and the electric power density bandwidth of our ME models can be obtained. In the future, we may include the electric power and the electric power density of the ME multibeam and ME two-piece trapezoidal bimorphs. Also, we may use other magnetostrictive materials such as Terfenol-D to build a higher performance ME energy harvester. Compared to Ni (λ_s = -50 ppm) based ME bimorph, Terfenol-D based ME energy harvester has a higher voltage and a better electric power density due to its supersaturation magnetostriction λ_s up to 1200 ~ 2000 ppm under Terfenol-D's saturated magnetic field at 1 T. The larger saturation magnetostriction λ_s leads to the larger strain. The higher stress transferred to the piezoelectric layer; therefore, we expect a larger voltage and higher electric power as well as a larger electric power density. For this reason, we can focus on Terfenol-D as our next magnetostrictive material when developing advanced trapezoidal ME cantilever beams.

`

APPENDICES

`

APPENDIX A: MATERIAL PROPERTIES

We used COMSOL Multiphysics 5.5 for all our simulation models. We used the following material properties for the metallic nickel, PZT-PZN-Scheme4, UNS C22000 brass, the high-strength alloy steel, and the air.

The linear material property of the metallic nickel

	Value	*Name*
E	200	Young's modulus (G pa)
ν	0.31	Poisson's ratio
σ	1.5625	Electric conductivity (10^{-7} S)
S	5×10^{-12}	Compliance (Pa^{-1})
ε_r	1	Dielectric constant (relative permittivity)
μ_r	600	Relative permeability
ρ	8800	Density (kg/m^3)
q_{11}	- 4140	Piezomagnetic coupling (m/A)
q_{12}	570	Piezomagnetic coupling (m/A)

`

The material property of the PZTPZN-Scheme4

	Value	*Name*
σ	667	Electric conductivity (10^{-7} S)
ε_r	1588	Dielectric constant (relative permittivity)
μ_r	1	Relative permeability
ρ	7850	Density (kg/m^3)
S_{11}	1.15	Compliance (10^{-11}Pa^{-1})
S_{12}	-3.91	Compliance (10^{-11}Pa^{-1})
S_{13}	-1.52	Compliance (10^{-11}Pa^{-1})
S_{33}	7.07	Compliance (10^{-11}Pa^{-1})
S_{44}	3.08	Compliance (10^{-11}Pa^{-1})
S_{66}	3.08	Compliance (10^{-11}Pa^{-1})
d_{31}	153.7	Piezoelectric charge constant (pC/N)
d_{33}	400	Piezoelectric charge constant (pC/N)

`

The material property of UNS C22000 Brass

	Value	*Name*
ν	0.34	Poisson’s ratio
ε_r	4500	Dielectric constant (relative permittivity)
μ_r	1	Relative permeability

The material property of the high-strength alloy steel

	Value	*Name*
E	200	Young's modulus (G pa)
ν	0.3	Poisson’s ratio
σ	4.03	Electric conductivity (10^6 S/m)
ε_r	1	Dielectric constant (relative permittivity)
μ_r	1	Relative permeability
ρ	7850	Density (kg/m^3)

`

The material property of the air

	Value	*Name*
σ	1	Electric conductivity (S/m)
ε_r	1	Dielectric constant (relative permittivity)
μ_r	1	Relative permeability

Elements of compliance matrix of sample one

$S_{11}, S_{22}(Pa^{-1})$	1.15×10^{-11}
$S_{13}, S_{31,}S_{32}, S_{23}(Pa^{-1})$	-1.152×10^{-11}
$S_{12}, S_{21}(Pa^{-1})$	-3.91×10^{-12}
$S_{33}(Pa^{-1})$	7.07×10^{-11}
$S_{44}, S_{55}(Pa^{-1})$	3.082×10^{-11}
$S_{66}(Pa^{-1})$	3.082×10^{-11}

`

Elements of compliance matrix of sample two

$S_{11}, S_{22}(Pa^{-1})$	1.01×10^{-11}
$S_{13}, S_{31,}S_{32}, S_{23}(Pa^{-1})$	-1.01×10^{-11}
$S_{12}, S_{21}(Pa^{-1})$	-3.54×10^{-12}
$S_{33}(Pa^{-1})$	1.58×10^{-11}
$S_{44}, S_{55}(Pa^{-1})$	2.73×10^{-11}
$S_{66}(Pa^{-1})$	2.73×10^{-11}

REFERENCES

[1] H. Li, C. Tian and Z. D. Deng, "Energy harvesting from low frequency applications using piezoelectric materials," *Applied Physics Reviews,* vol. 1, no. 4, 2014.

[2] S. Zhou and X. Gao, Magnetostrictive Material, Beijing: Metallurgical Industry Press, 2017.

[3] N. Chen and V. Bedekar, "Modeling, Simulation and Optimization of Piezoelectric Bimorph Transducer For Broadband Vibration Energy Harvesting in multi-beam and trapezoidal approach," *Journal of Materials Science Research,* vol. 7, no. 2, October 2018.

[4] V. B. Nan Chen, "Design, Modeling, and Simulation of Two-Piece Trapezoidal Piezoelectric Devices for Sensing and Energy Harvesting," *Journal Of Advances in Materials Science and Engineering,* vol. 2020, 2020 Feb..

[5] J. L. GONZALEZ, A. RUBIO and F. MOLL, "Human Powered Piezoelectric Batteries to Supply Power to Wearable Electronic Devices," *Int. J. Soc. Mater. Eng. Resour.,* vol. 10, no. 1, March 2002,http://doi.org/10.5188/ijsmer.10.34.

[6] M. Broussely, P. Biensan, F. Bonhomme, P. Blanchard, S. Herreyre, K. Nechev and R. Staniewicz, "Main aging mechanisms in Li ion batteries," *Journal of Power Sources,* Vols. 146,https://doi.org/10.1016/j.jpowsour.2005.03.172, no. 1-2, May 2005.

[7] Y. Hu and Y. Xu, "A wideband vibration energy harvester based on a folded asymmetric gapped cantilever," *Appl. Phys. Lett,* vol. 104, no. 5, 2014,https://doi.org/10.1063/1.4863923 .

[8] M. Inc, "Vibration Energy Harveste Date Sheet," www.microstrain.com, Williston,VT, 2011.

[9] M. Wu, Y. Ou, H. Mao, Z. Li, R. Liu, A. Ming and W. Ou, "Multi-resonant wideband energy harvester based on a folded asymmetric M-shaped," *AIP Advances,* vol. 5, no. 7, 2015, https://doi.org/10.1063/1.4927466 .

[10] J. Liu, H. Fang, Z. Xu, X. Mao and X.C. Shen, "A MEMS-based piezoelectric power generator array for vibration energy harvesting," *Microelectronics,* vol. 39, no. 5, May 2008,https://doi.org/10.1016/j.mejo.2007.12.017.

[11] J. Yang, Y. Wen, P. Li, X. Dai and M. Li, "A Broadband Vibration Energy Harvester Using Magnetoelectric Transducer," in *IEEE SENSORS 2010 Conference*, 2010.

[12] J. YANG and e. al., "Magnetoelectric Energy Harvesting from Vibrations of Multiple Frequencies," *Journal of Intelligent Material Systems and Structures,* vol. 22, no. 14, 2011.

[13] F. Cerini, M. Baù, M. Ferrari and V. Ferrari, "Impact-Enhanced Multi-beam Piezoelectric Converter for Energy Harvesting in Autonomous Sensors," *Sensors and Microsystems,* vol. 268, no. 72, 2014,https://doi.org/10.1016/j.proeng.2012.09.173.

[14] N. Chen and V. Bedekar, "Modeling, Simulation and Optimization of Piezoelectric Bimorph Transducer For Broadband Vibration Energy Harvesting," *Journal of Material Science Research,* vol. 6, no. 4, Oct. 2017, https://doi.org/10.5539/jmsr.v6n4p5.

[15] V. Bedekar, J. Oliver and S. Priya, "Design and fabrication of bimorph transducer for optimal vibration energy harvesting," *IEEE Trans. Ultrason., Ferroelect., Freq. Contr. , Permission to use Figure 2(d) , Figure 3(d),* vol. 57, no. 7, June 2010,DOI: 10.1109/TUFFC.2010.1582.

[16] G. Zhang, S. Gao, H. Liu and S. Niu, "A low frequency piezoelectric energy harvester with trapezoidal cantilever beam: theory and experiment," *Microsyst Technol,* vol. 23, no. 8, 2017,DOI 10.1007/s00542-016-3224-5.

[17] R. Usharani, G. Uma and M. Umapathy, "Design of high output broadband piezoelectric energy harvester with double tapered cavity beam," *Int. J. of Precis. Eng. and Manuf.-Green Tech,* vol. 3, no. 4, 2016,DOI: 10.1007/s12206-017-0603-5.

[18] R. Hosseini and M. Hamedi, "An investigation into resonant frequency of trapezoidal V-shaped cantilever piezoelectric energy harvester," *Microsyst. Technol.,* vol. 22, no. 5, May 2016,https://doi.org/10.1007/s00542-015-2583-7.

[19] D. Benasciutti, L. Moro, S. Zelenika and E. Brusa, "Vibration energy scavenging via piezoelectric bimorphs of optimized shapes," *Microsyst Technol,* vol. 16, no. 5, 2010,DOI 10.1007/s00542-009-1000-5.

[20] J. Twiefel, M. Neubauer and J. Wallaschek, "Bandwidth Improvement for Vibration Energy Harvesting devices," in *AMA Conferences 2013*, Hanover, 2013,DOI 10.5162/sensor2013/C2.1.

[21] C.-W. Nan, M. I. Bichurin, S. Dong, D. Viehland and G. Srinivasan, "Multiferroic magnetoelectric composites: Historical perspective, status, and future directions," *Journal of Applied Physics*, vol. 103, no. 3, 2008,http://dx.doi.org/10.1063/1.2836410.

[22] M. Fiebig, "Revival of the magnetoelectric effect," *JOURNAL OF PHYSICS D: APPLIED PHYSICS*, vol. 38, no. 8, 2005, stacks.iop.org/JPhysD/38/R123.

[23] J. Ryu, S. Priya, K. Uchino and H.-E. Kim, "Magnetoelectric Effect in Composites of Magnetostrictive and Piezoelectric Materials," *Journal of Electroceramics*, vol. 8, no. 2, August 2002,https://doi.org/10.1023/A:102059972.

[24] T. Wandowski, J. Moll, P. Malinowski, S. Opoka1 and W. Ostachowicz, "Assessment of piezoelectric sensor adhesive bonding," *Journal of Physics: Conference Series*, vol. 628, 2015,doi:10.1088/1742-6596/628/1/012114.

[25] W. C. B. R. G. Young, Roark's Formulas for Stress and Strain, 7nd Edition, McGraw-Hill, Chapter 16 , pp 767 - 768, 2002.

[26] Varadarajan and Bhanusri, "Varadrajan and Bhanusri, Design and Simulation of Unimorph Piezoelectric Energy Harvesting System," in *COMSOL Conference* , Bangalore, 2013.

[27] Y. D. Chong, "MH2801: Complex Methods for the Science," 2016. [Online]. Available: www1.spmd.ntu.edu.sg/~ydchong/teching/04_complex_oscillations.pdf.

[28] J.-b. Yuan, T. Xie and W.-s. Chen, "Energy harvesting with piezoelectric cantilever," in *IEEE International Ultrasonics Symposium Proceedings*, eijing, China, 2008,10.1109/ULTSYM.2008.0339.

[29] P. Mitcheson and e. al., "Energy Harvesting From Human and Machine Motion for Wireless Electronic Devices," *Proceedings of IEEE*, vol. 94, no. 9, Sep. 2008.

[30] S. Priya and D. J. Inman, Energy Harvesting Technologies, Boston, MA: Spring Science & Business Media, 2008.

[31] N. Chen and V. Bedekar, "Design, Modeling, and Simulation of Two-Piece Trapezoidal Piezoelectric Devices for Sensing and Energy Harvesting," *Journal of Advances in Materials Science and Engineering*, vol. 2020, 2020.

[32] S. Zhou and X. Gao, Magnetostrictive Materials, Beijing: Metallurgical Industry Press, 2017.

[33] V. Annapureddy and e. al., "Magnetic energy harvesting with magnetoelectrics: an emerging technology for self-powered autonomous systems," *Sustainable Energy & Fuels*, vol. 1, no. 10, 2017.

[34] Z. Chu and e. al., "Dual-stimulus magnetoelectric energy harvesting," *Materials for Energy Harvesting (MRS) Bulletin*, vol. 43, no. 3, DOI: 10.1557/mrs.2018.31, 2018.

[35] Y. Cheng and e. al., "Recent development and status of magnetoelectric materials and devices," *Physics Letters A*, vol. 328, no. 41, 2018.

[36] V. B. Bichurin, I. Solovjev and S. Priya, "Multimodal Energy Harvesting System," in *Proc. of SPIE*, 2011.

[37] X. Bai, Y. Wen, J. Yang, P. Li, Jing Qiu and Y. Zhu, "A magnetoelectric energy harvester with the magnetic coupling to enhance the output performance," *JOURNAL OF APPLIED PHYSICS*, vol. 111, no. 7, p. https://doi.org/10.1063/1.3677877, 2012.

[38] Y. Wang, J. Li and D. Viehland, "Magnetoelectrics for magnetic sensor applications: status, challenges and perspectives," *Materials Today*, vol. 17, no. 6,https://doi.org/10.1016/j.mattod.2014.05.004, pp. 269-275, 2014.

[39] M. Bichurin, V. Petrov and G. Srinivasan, "Theory of low-frequency magnetoelectric effects in ferromagnetic-ferroelectric layered composites," *Journal of Applied Physics*, vol. 92, no. 12, p. DOI: 10.1063/1.1522834, 2002.

[40] P. Ramos, H. Amorín, J. Ricote, A. Castro and M. Algueró, "Insights into the Performance of Magnetoelectric Ceramic Layered Composites," *Journal of composites science (MDPI)*, vol. 1, no. 14, p. DOI: 10.3390/jcs1020014, 2017.

[41] C.-S. Park, C.-W. Ahn, J. Ryu, W.-H. Yoon, D.-S. Park, H.-E. Kim and S. Priya, "Design and characterization of broadband magnetoelectric sensor," *Journal of Applied Physics*, vol. 105, no. 9, p. https://doi.org/10.1063/1.3117484, 2009.

[42] Z. Lin, J. Chen, X. Li, J. Li, J. Liu, Q. Awais and J. Yang, "Broadband and three-dimensional vibration energy harvesting by a non-linear magnetoelectric generator," *Appl. Phys. Lett.*, vol. 109, no. 25, p. https://doi.org/10.1063/1.4972188, 2016.

[43] S. D. Patil, K. Y. Rajpure and A. M. Shaikh, "Magnetoelectric Coupling in Metglas/BaTiO3/Metglas Lead-Free Magnetoelectric Composites," *Journal of Materials Science and Chemical Engineering*, vol. 4, no. 8, p. http://dx.doi.org/10.4236/msce.2016.48001, 2016.

[44] W. Yong-ping, Z. Zheng and Q. Jin-hao, "Magnetoelectric voltage coefficients of magnetoelectric composite," *Transactions of Nonferrous Metals Society of China*, vol. 16, no. https://doi.org/10.1016/S1003-6326(06)60134-9, 2006.

[45] V. Bedekar, M. Bichurin, I. Solovjev and S. Priya, "Multimodal Energy Harvesting System," in *SPIE Defense, Security, and Sensing,United States* , Orlando,FL, 2011,doi: 10.1117/12.884747.

[46] COMSOL, "Improving convergence in nonliear time dependent models".

[47] G. Simon, "What is the quality factor and how does it relate to loss?," Onscale, 4th March 2020. [Online]. Available: https://onscale.com/blog/what-is-the-quality-factor-and-how-does-it-relate-to-loss/.

[48] J. Han, J. Hu, Z. Wang, S. X. Wang and J. He, "Enhanced performance of magnetoelectric energy harvester based on compound magnetic coupling effect," *JOURNAL OF APPLIED PHYSICS*, vol. 117, no. 14, 2015.

[49] S. Dong, J. Li and D. Viehland, "Theory Analysis on Magnetoelectric Voltage Coefficients of the Terfoneol-D/PZT Composite Transducer," Virginia Tech, Blacksburg, 2003.

[50] S. Dong, J. Zhai, J. F. Li, D. Viehland and S. Priya, "Multimodal system for harvesting magnetic and mechanical energy," *APPLIED PHYSICS LETTERS,* vol. 93, no. 10, 2008.

[51] A. e. al., "Enhanced magnetic energy harvesting properties of magneto-mechano-electric generator by tailored geometry," *APPLIED PHYSICS LETTERS,* vol. 109, no. 9, p. https://doi.org/10.1063/1.4962047, 2016.

[52] S. H. Mohamad, M. F. Thalas, A. Noordin, M. S. Yahya, M. H. C. Hassan and Z. Ibrahim, "A POTENTIAL STUDY OF PIEZOELECTRIC ENERGY HARVESTING IN CAR VIBRATION," *ARPN Journal of Engineering and Applied Sciences,* vol. 10, no. 19, 2015.

[53] H. Salmani, G. H. Rahimi and S. A. Hosseini H., "An Exact Analytical Solution to Exponentially Tapered Piezoelectric Energy Harvester," *Shock and Vibration,* vol. 2015, no. 1, July 2015,http://dx.doi.org/10.1155/2015/426876.